

Aus der Klinik für Neurologie  
(Prof. Dr. med. M. Bähr)  
der Medizinischen Fakultät der Universität Göttingen

**Axonal transport of autophagosomes in  
models of neurodegeneration in vitro  
and in vivo**

INAUGURAL-DISSERTATION

zur Erlangung des Doktorgrades  
der Medizinischen Fakultät der  
Georg-August-Universität zu Göttingen

vorgelegt von

**Xiaoyue Luo**

aus

Hunan, China

Göttingen 2023

Dekan: Prof. Dr. med. W. Brück

### **Betreuungsausschuss**

Betreuer: PD Dr. med. J. C. Koch

Ko-Betreuer: PD Dr. med. C. van Oterendorp

### **Prüfungskommission**

Referent/in: PD Dr. med. J. C. Koch

Ko-Referent/in: .....

Drittreferent/in: .....

Datum der mündlichen Prüfung: .....

Hiermit erkläre ich, die Dissertation mit dem Titel „Axonal transport of autophagosomes in models of neurodegeneration in vitro and in vivo“ eigenständig angefertigt und keine anderen als die von mir angegebenen Quellen und Hilfsmittel verwendet zu haben.

Göttingen, den 04.05.2023

.....

(Xiaoyue Luo)

# Table of Contents

<b>List of Figures .....</b>	<b>III</b>
<b>List of Tables .....</b>	<b>IV</b>
<b>Abbreviations .....</b>	<b>V</b>
<b>1 Introduction .....</b>	<b>1</b>
1.1 Neurodegeneration in the central nervous system .....	1
1.2 Traumatic axonal injury .....	2
1.2.1 Acute axonal degeneration .....	2
1.2.2 Wallerian degeneration.....	4
1.3 Glaucoma-induced neurodegeneration .....	4
1.4 Aging .....	7
1.5 Autophagy .....	9
1.6 Aims of this thesis.....	13
<b>2 Materials and Methods .....</b>	<b>14</b>
2.1 Materials.....	14
2.1.1 Animals .....	14
2.1.2 Chemicals .....	14
2.1.3 Buffers, solutions, and their recipes .....	16
2.1.4 Viral vectors .....	16
2.1.5 Antibodies .....	17
2.1.6 Equipment .....	18
2.1.7 Software .....	19
2.2 Methods .....	20
2.2.1 cDNA Cloning and production of adeno-associated viral vectors.....	20
2.2.2 Neuronal cell culture in microfluidic chambers .....	20
2.2.2.1 Preparation of microfluidic chambers .....	20
2.2.2.2 Coating with poly-L-ornithine and laminin.....	21
2.2.2.3 Primary cortical neuron culture and cell seeding.....	21
2.2.2.4 Test of virus toxicity and transduction efficacy.....	22
2.2.2.5 Co-culture of cortical neurons and astrocytes .....	22
2.2.2.6 Viral transduction and medium changes .....	23
2.2.2.7 Axotomy.....	24
2.2.2.8 Treatment with pepstatin A, BODIPY™ FL Conjugate .....	24
2.2.2.9 Recycling of microfluidic chamber.....	24
2.2.3 Live-cell microscopy and quantification.....	24
2.2.3.1 Real-time imaging of LC3 transport in degenerating axons in vitro.....	25
2.2.3.2 Quantification of live-imaging in microfluidic chambers in vitro .....	25
2.2.3.3 Imaging and quantification of BODIPY-pepstatin A and LC3 co-localization in vitro.....	25
2.2.4 Animal experiments .....	26
2.2.4.1 Intravitreal injections of viral vectors .....	26
2.2.4.2 Surgical exposure of the optic nerve .....	27
2.2.4.3 Crush lesion of the optic nerve.....	27
2.2.4.4 Establishment of the subacute glaucoma animal model.....	28
2.2.4.5 Two-photon live imaging of axonal LC3 transport on the optic nerve .....	28
2.2.4.6 Quantification of in vivo live imaging .....	29

2.2.5	Immunohistochemistry .....	29
2.2.5.1	Animal euthanasia and tissue processing .....	29
2.2.5.2	Immunohistochemical staining and quantification.....	30
2.2.6	Sodium dodecyl sulfate-polyacrylamide gel electrophoresis (SDS-PAGE) .....	31
2.2.7	Immunoblotting and quantification .....	31
2.2.8	Statistical analyses.....	32
<b>3</b>	<b>Results .....</b>	<b>34</b>
3.1	Experimental set-up for an in vitro model of acute axonal degeneration.....	34
3.2	Evaluation of axonal transport of autophagosomes after axotomy in vitro.....	35
3.3	Establishment of in vivo models of axonal degeneration in the optic nerve .....	37
3.3.1	Autophagosome trafficking in young animals at basal levels .....	38
3.3.2	Evaluation of autophagosome transport in aging .....	38
3.3.3	Transport of autophagosomes in the crush lesion model .....	39
3.3.3.1	Assessment of autophagosome trafficking in the crush lesion model.....	39
3.3.3.2	Colocalization of LC3 and active Cath D after axotomy in vitro.....	42
3.3.3.3	Colocalization of LC3 and active Cath D after axotomy in vivo .....	46
3.3.3.4	Activation of autophagy after optic nerve crush injury in rats .....	48
3.3.3.5	Crush lesion alters autophagic flux and the motor protein distribution in the rat optic nerve .....	49
3.3.4	Analysis of autophagosome transport in a subacute glaucoma model .....	51
3.3.4.1	Establishment of a subacute glaucoma model based on limbal vascular plexus cauterization .....	51
3.3.4.2	Evaluation of autophagosome transport in the glaucoma model.....	52
<b>4</b>	<b>Discussion .....</b>	<b>55</b>
4.1	Dynamic changes in axonal trafficking of autophagosomes after axotomy in vitro ....	55
4.2	In vivo autophagosome trafficking in axonal degeneration models.....	56
4.3	Fusion of autophagosomes and lysosomes following axonal injury .....	58
4.4	Autophagy is induced following acute axonal injury in vivo.....	59
4.5	Degradative capacity in the autophagy pathway is impaired after axonal lesion.....	59
4.6	Crush lesion selectively disrupts the retrograde axonal transport in the optic nerve ...	60
4.7	Conclusion.....	61
<b>5</b>	<b>Summary .....</b>	<b>62</b>
<b>6</b>	<b>Bibliography .....</b>	<b>64</b>

## List of Figures

Figure 1: Schematic diagram of the molecular and morphological processes involved in acute axonal degeneration (AAD) .....	3
Figure 2: Overview of pathological features involved in glaucoma .....	6
Figure 3: Schematic diagram of the autophagic process in mammals .....	12
Figure 4: Vector diagram of AAV6-mScarlet-LC3 .....	20
Figure 5: Acute axonal degeneration model in vitro .....	34
Figure 6: Live imaging of autophagosomes in rat primary cortical neurons after axotomy in vitro on DIV 10 .....	35
Figure 7: Live imaging of autophagosomes in vivo .....	37
Figure 8: In vivo autophagosome transport of the optic nerve in young adult rats (3 months) and aged rats (18 months) .....	40
Figure 9: In vivo autophagosome transport in the optic nerve of rats after crush lesion .....	42
Figure 10: Decreased colocalization of LC3 and active Cath D after axotomy in vitro .....	45
Figure 11: Colocalization of LC3 and cathepsin D in the rat optic nerve 6 hours after crush lesion .....	47
Figure 12: Crushed-induced autophagy in rat optic nerve .....	48
Figure 13: Changes of autophagic pathways in the rat optic nerve 6 hours after crush lesion .....	49
Figure 14: Motor protein levels in the rat optic nerve 6 hours after crush lesion .....	51
Figure 15: In vivo autophagosome transport in the optic nerve of rats after cautery .....	53

---

## List of Tables

Table 1: Chemicals .....	14
Table 2: Buffers and solutions recipes.....	16
Table 3: Viral vectors .....	16
Table 4: Primary antibodies .....	17
Table 5: Secondary antibodies .....	17
Table 6: Equipment.....	18
Table 7: Software .....	19
Table 8: Antibodies and dilutions involved in Western blotting .....	32
Table 9: IOP measurements in OHT and control eyes in 5 rats.....	51

## Abbreviations

3-MA	3-methyladenine
AAD	acute axonal degeneration
AAV	adeno-associated virus
AD	Alzheimer's disease
AH	aqueous humor
ANOVA	analysis of variance
ATG	autophagy-related protein
ATP	adenosine triphosphate
BCA	bicinchoninic acid
BDNF	brain-derived neurotrophic factor
bGH-pA	bovine growth hormone- polyadenylation
BODIPY	boron-dipyrromethene
BSA	bovine serum albumin
CB	chicken beta-actin
CNTF	ciliary neurotrophic factor
CMA	chaperone-mediated autophagy
CMF	calcium magnesium-free
CMV	cytomegalovirus
CNS	central nervous system
CRMP2	collapsin response mediator protein-2
CTB	cholera toxin subunit-B
DEX	dexamethasone
DIV	day in vitro
DMEM	dulbecco's modified eagle medium
DMSO	dimethyl sulfoxide
DRGs	dorsal root ganglia neurons
DTT	dithiothreitol
E18	embryonic day 18
ECL	enhanced chemiluminescence
FCS	fetal calf serum
FIP200	focal adhesion kinase family-interacting protein of 200 kDa
GAPDH	glyceraldehyde 3-phosphate dehydrogenase
GC	glucocorticoid
HBSS	Hank's balanced salt solution
HcT	tetanus neurotoxin
IOP	intraocular pressure
LC3	microtubule-associated protein 1 light chain 3
LGN	lateral geniculate nucleus
NAD	nicotinamide adenine dinucleotide



---

NMN	nicotinamide mononucleotide
NMNAT2	NMN adenylyltransferase 2
NT4/5	neurotrophic factor 4/5
OHT	ocular hypertension
ONC	optic nerve crush
ONH	optic nerve head
PBS	phosphate buffered saline
PD	Parkinson's disease
PE	phosphatidylethanolamine
PFA	paraformaldehyde
PI3K	phosphatidylinositol 3-kinase
PI3P	phosphatidylinositol 3-phosphate
PLO	poly-L-ornithine
PSN	penicillin/streptomycin/neomycin
RGCs	retinal ganglion cells
ROIs	regions of interest
SARM1	sterile alpha and TIR motif-containing 1
SC	superior colliculus
SCI	spinal cord injury
SDS	sodium dodecyl sulfate
SDS-PAGE	SDS-polyacrylamide gel electrophoresis
SNAREs	soluble N-ethylmaleimide-sensitive factor attachment protein receptors
SQSTM1	sequestosome 1
TBI	traumatic brain injury
TBS	Tris-buffered saline
TBS-T	TBS with 0.1% Tween-20
TM	trabecular meshwork
ULK1	uncoordinated 51-like kinase 1
VPS34	vacuolar protein sorting 34
WD	wallerian degeneration
WPRE	woodchuck hepatitis virus post-transcriptional regulatory element

# 1 Introduction

## 1.1 Neurodegeneration in the central nervous system

Among many traumatic and neurodegenerative diseases of the central nervous system (CNS), neuronal cell death is one of the main pathological hallmarks and the leading cause of progressive clinical dysfunction (Akamatsu and Hanafy 2020; Chi et al. 2018). To prevent or delay excessive neuronal loss during the process of these detrimental diseases, increasing attempts have been made to unravel the underlying mechanisms and identify therapeutic targets aimed at protecting the cell body from degeneration. However, all endeavors proved to have limited success in the long-term experimental trials. As a matter of fact, it is becoming increasingly evident that axonal degeneration rather than neuronal soma is the initial step and in turn promotes neuronal death in traumatic and neurodegenerative diseases (Coleman 2005; Fischer et al. 2004). Further elucidation of the pathological mechanisms underlying CNS axonal degeneration provides the most immediate possibility for early intervention to rescue neuronal cells and thus provides a promising future therapeutic strategy.

However, axonal degeneration comprises a complex regulatory cascade of self-destruction that can result from various stimuli, including toxins, trauma, aging, and genetic deficits (Coleman 2005; Wang et al. 2012). In recent years, a growing understanding of this field has inspired a number of interventional paradigms to better elucidate its mechanisms. One of the most common methods for reproducibly inducing axonal degeneration is through traumatic axonal injury (Hill et al. 2016; Wang et al. 2021). Therefore, many studies have concentrated on the mechanisms of degeneration following axonal injury and searched for one or several key molecules or pathways for modulation that can effectively counteract lesion-induced axonal loss. However, although there may be some overlap in the pathophysiological cascade between different models, axonal degeneration cannot be considered as an exactly uniform series of events due to diverse etiologies (Lingor et al. 2012). Hence, it is critical and necessary to use different models of neurodegeneration for comparison or to elucidate the scope of application of interventions. In addition, promising findings could hopefully translate into potential treatments for neurodegenerative diseases in the future.

## 1.2 Traumatic axonal injury

Mounting evidence for traumatic axonal injury in the CNS has illuminated the pathology of axonal degeneration in terms of temporal and spatial dynamics (Hill et al. 2016; Knöferle et al. 2010). Improved comprehension of the fundamental mechanisms underlying simple traumatic axonal injury allows us to simulate axonal degeneration in more complex neurodegenerative situations. In general, post-axonal degeneration can be divided into two discernible phases based on morphological characteristics: a transient and early-onset degenerative event, referred to as acute axonal degeneration (AAD), has quickly happened in both proximal and distal segments of the lesion, and a subacute process consisting of a slow dying back degeneration in the proximal axons and Wallerian degeneration (WD) in the distal axonal parts (Zhang et al. 2021). WD is then followed by infiltration of glial cells, including astrocytes, macrophages and Schwann cells, to clear axonal debris. However, altering physiological conditions within several hours of injury, such as decreasing extracellular calcium levels, inhibiting calcium-dependent protease activity, or expression of the *WldS* transgene, can significantly attenuate axonal degeneration and preserve the integrity of damaged axons (Conforti et al. 2000; Knöferle et al. 2010; Zhang et al. 2016). Thus, identification of potential molecular processes at distinct morphological phases may shed light on possible targets to delay or even partially rescue axonal degeneration in the CNS.

### 1.2.1 Acute axonal degeneration

In vivo live imaging experiments in the optic nerve and spinal cord have shown that axonal segments on both sides of the lesion developed AAD as soon as several minutes after focal traumatic axonal injury (Kerschensteiner et al. 2005; Knöferle et al. 2010). The prompt reaction to injury is exhibited by rapid axonal fragmentation extending up to 400  $\mu\text{m}$  adjacent to the axonal terminal on both sides between 5 and 60 min and followed by the slow formation of degenerating bulbs to accumulate cellular organelles due to disruption of axonal transport (Figure 1).

Channel-mediated extracellular  $\text{Ca}^{2+}$  influx is a key event to initiate AAD, as  $\text{Ca}^{2+}$ -channel inhibitors suppress early intra-axonal  $\text{Ca}^{2+}$  elevation and further retard the AAD progression (Knöferle et al. 2010; Koch et al. 2010). In addition, administration of  $\text{Ca}^{2+}$  ionophores significantly accelerates the axonal degenerative processes (Knöferle et al. 2010). Besides, calcium-dependent activation of proteases such as calpain leads to cytoskeletal condensation and disintegration, including cleavage of axonal microtubules

as well as neurofilaments, which corresponds to the onset of AAD (Czogalla and Sikorski 2005; Ma 2013). Furthermore, abnormal activation of calpain after axonal injury also has deleterious effects on a series of downstream substrates (Metwally et al. 2021). For example, collapsin response mediator protein-2 (CRMP2), a key downstream target of calpain, was significantly cleaved 6h after the optic nerve crush (ONC), while CRMP2 overexpression or calpain blockers alleviated axonal degeneration after axotomy (Ribas et al. 2017; Zhang and Koch 2017; Zhang et al. 2016).

Another striking characteristic feature of AAD is the excessive activation of autophagy (Yang et al. 2013). It is common to observe significant autophagosome accumulation after lesion-induced AAD. Blockade of autophagy with 3-methyladenine (3-MA) markedly reduces the number of autophagosomes and protects against axonal degeneration (Koch et al. 2010). However, pharmacological inhibition of the  $\text{Ca}^{2+}$  channel attenuates axonal degeneration more robustly, indicating that autophagy serves as a downstream target of  $\text{Ca}^{2+}$  flux (Knöferle et al. 2010). Given the critical role of autophagy in AAD implementation, it provides a potential therapeutic strategy.

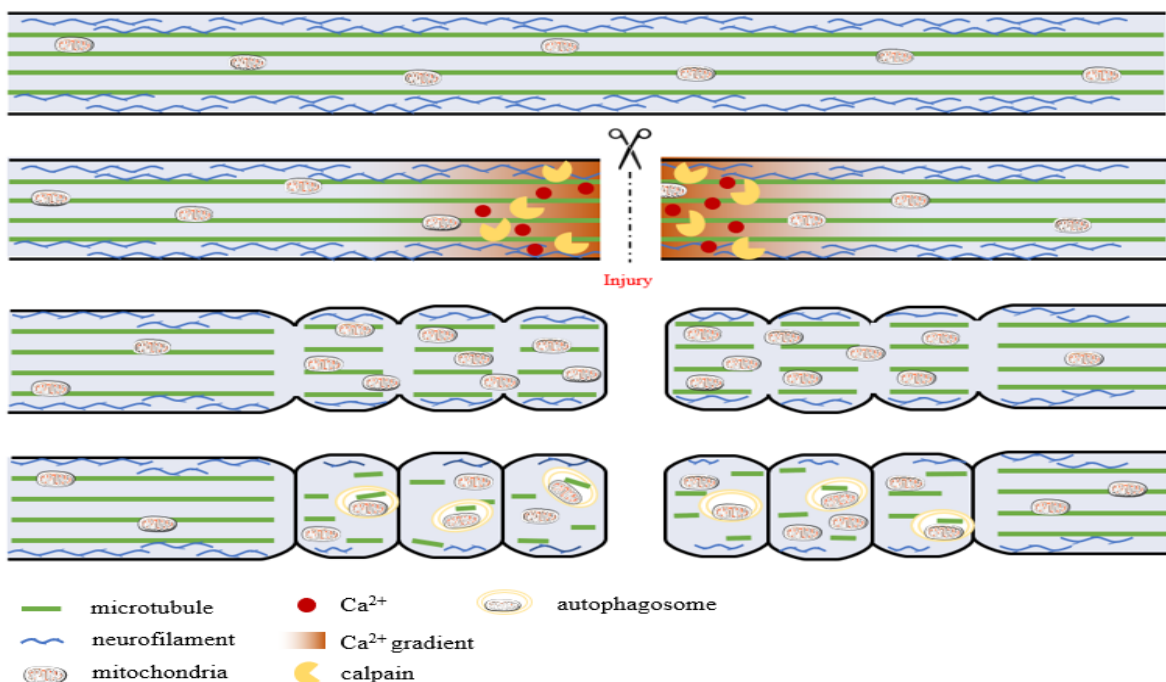


**Figure 1: Schematic diagram of the molecular and morphological processes involved in acute axonal degeneration (AAD).** As early as 5–60 min post-axonal traumatic injury, the axonal terminals on both sides demonstrate AAD, primarily regulated by rapidly increased intracellular  $\text{Ca}^{2+}$  influx and abnormal activation of calcium-dependent proteases such as calpain. Misalignment of neurofilaments and disruption of microtubules subsequently can be seen, as well as locally accumulated organelles due to dysfunctional axonal transport. Afterward, axonal bulbs are gradually formed, and autophagy is excessively induced to eliminate cytoskeletal shards and damaged organelles. Figure modified from Lingor et al. (2012).

### 1.2.2 Wallerian degeneration

Wallerian degeneration (WD) is conventionally characterized as the process of axonal degeneration located distally after traumatic injury (Waller 1851). During the first 24 to 72 h, the distal part of axons still exhibits stable morphology and performs some physiological functions. For example, action potential conduction is still maintained in transected motor neuron axons for 24 h following axotomy in vivo, despite gradual decay of evoked potentials and conduction velocities (Moldovan et al. 2009). Hereafter, the distal stump degenerates rapidly, resulting in complete fragmentation of the axons. However, the molecular mechanism underlying WD has not been completely clarified. Although increased  $\text{Ca}^{2+}$  levels in axons contribute to WD, they are not necessary to initiate its process (Conforti et al. 2014). It is suggested that a core event during WD following axonal injury is the disrupted transport of the vital survival factor nicotinamide mononucleotide adenylyltransferase 2 (NMNAT2) from the cell body to the distal axons (Gilley and Coleman 2010). Consequently, the loss of NMNAT2 results in a decrease in the coenzyme nicotinamide adenine dinucleotide (NAD), but a rise in its precursor nicotinamide mononucleotide (NMN) (Hill et al. 2016). NAD depletion, NMN accumulation or even both are considered to ultimately trigger WD (Coleman MP and Höke 2020). Afterward, activation of downstream modulators with executive functions, particularly the sterile alpha and TIR motif-containing 1 (SARM1) protein, further orchestrates rapid axonal fragmentation (Gerdtz et al. 2015; Osterloh et al. 2012).

### 1.3 Glaucoma-induced neurodegeneration

Glaucoma is a leading neurodegenerative disease that leads to progressive vision loss and irreversible blindness (Kang and Tanna 2021). It affects more than 60 million individuals in the world in 2019, and this number will escalate to an estimated 111.8 million by 2040 (Tham et al. 2014). Under normal conditions, standard intraocular pressure (IOP) is maintained by balancing the aqueous humor (AH) generation and its subsequent efflux through the trabecular meshwork (TM). According to the degree of ocular drainage canal closure in the anterior segment, there are two major subtypes of glaucoma: open-angle glaucoma and angle-closure glaucoma. Their common features are the loss of retinal ganglion cells (RGCs) and optic nerve degeneration in response to elevated IOP (Schuster et al. 2020). Despite successful pharmacological and surgical therapies to reduce IOP, the progression of visual impairment cannot be stopped in most patients with glaucoma (Gupta and Yücel 2007). Hence, there is an urgent need to understand the early pathophysiological manifestations of glaucoma in order to prevent further visual loss

during IOP-lowering treatments.

Emerging experimental animal models provide effective and practical research tools to explore the underlying mechanisms of glaucomatous neurodegeneration, especially in primates and rodents, whose eyes share numerous biological similarities with humans (McKinnon et al. 2009; Millar and Pang 2015). These models artificially simulate glaucomatous damage via genetically modified mice with glaucoma, physical blockage of the aqueous outflow pathway or pharmacologically inducible ocular hypertension (OHT), like potent glucocorticoid (GC) administration (Pang and Clark 2020). Given that RGCs are located within the retina, their axons span a considerable length, converging at the optic disc to form the optic nerve, which in turn projects to the lateral geniculate nucleus (LGN) and superior colliculus (SC), and connect the eye to the brain to transmit visual information. Damage to any of these regions can affect its functional integrity. However, the elevated IOP in glaucoma and resulting low perfusion trigger a series of apoptotic cascades in the retina that lead to the death of RGCs, including oxidative stress, excitatory amino acid neurotoxicity, ischemia, and glial/astrocyte activation (Qu et al. 2010). Additionally, mounting evidence demonstrates that glaucomatous damage also occurs in the visual center of the brain, especially in the LGN, contributing to the cell body atrophy, pronounced decline in dendritic fields and complexity (Almasieh et al. 2012). Furthermore, excessive IOP also causes mechanical stress damage to nerve fibers, especially at the optic nerve head (ONH), resulting in structural changes that compromise neurotrophic factor transport from the superior colliculus to the RGC soma, such as brain-derived neurotrophic factor (BDNF) and neurotrophic factor 4/5 (NT4/5) (Davis et al. 2016; Vidal et al. 2012). Transport deficits also appear in anterograde transport. By intravitreal administration of labeled cholera toxin subunit-B (CTB), DBA/2 transgenic mice of the glaucoma model first experienced a loss of transport at their most distal site, where the RGC axon terminates in the SC. Deficits propagate toward more anterior RGC targets in the brain, including the optic tract and nerves, and then reach the retina, where active uptake is ultimately compromised (Crish et al. 2010). Impaired transport in both directions and the consequent dysfunction of cargo trafficking, together with all the mechanisms mentioned above (Figure 2), could be involved and interact with each other, ultimately resulting in nerve degeneration and neuronal cell death (Dias et al. 2022; Qu et al. 2010).

Interestingly, growing evidence in recent years has shown that defective axonal transport in glaucoma appears to precede the structural alterations of RGCs. Vidal et al. described an important study in which the total number of Brn3a<sup>+</sup> RGCs was greater than that of

FG<sup>+</sup>- (rats) or OHSt<sup>+</sup> (mice) retrogradely traced RGCs from the SC back to the RGC soma 8 days after OHT induction by laser photocoagulation of limber tissues, indicating that some surviving RGCs had already altered retrograde transport (Vidal et al. 2012). It was also reported that in a GC-induced OHT mouse model, no functional or structural damage to the RGC soma was observed after 5 weeks of periocular injection with dexamethasone 21-acetate (Dex), but TEM imaging revealed significant axonal degeneration within the proximal portion of the optic nerve compared with Veh-injected mice, although the distal region was not involved. The transport of fluorescent CTB injected into the eye was further detected in the continuous frontal sections of the SC, exhibiting mild transport impairment in the posterior regions. In contrast, no CTB transport was found in the SC after 8 weeks of treatment with Dex. Consistent with this, PPD staining, which was employed to detect optic nerve degeneration, revealed similar axonal degeneration in both the proximal and distal optic nerve, along with significant loss of RGCs (Maddineni et al. 2020). Therefore, transport deficits are an early event in glaucoma progression. The temporal gap between impaired transport and the structural deterioration of RGCs presents itself as a conceivable therapeutic opportunity to attenuate irreversible vision damage.

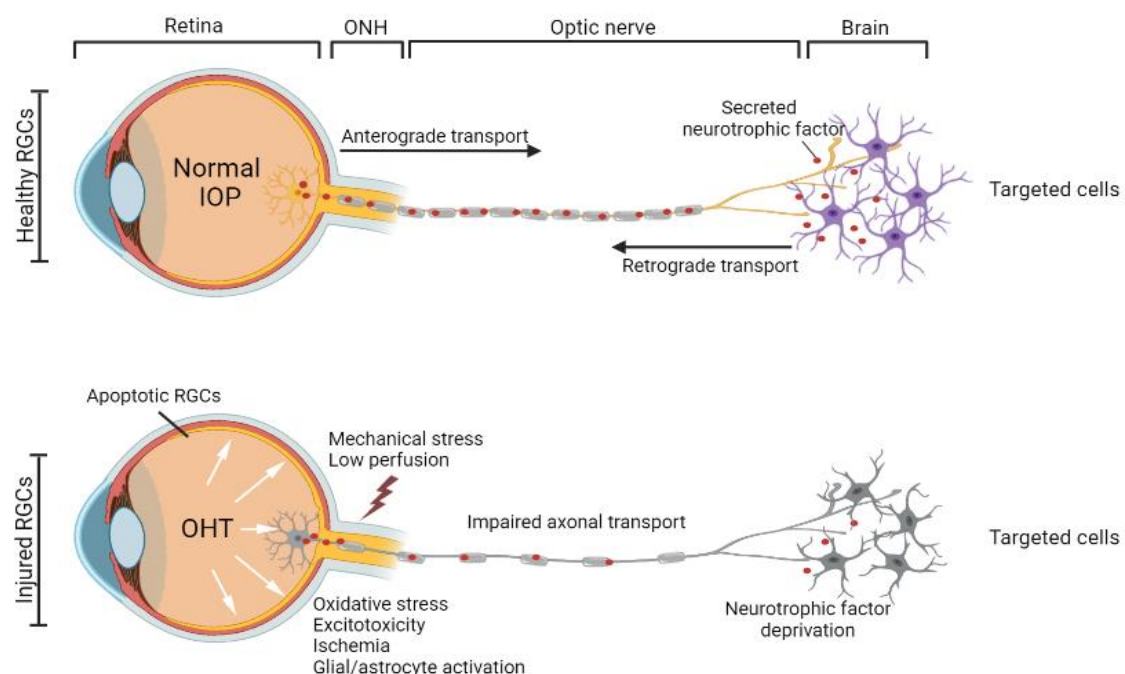


**Figure 2: Overview of pathological features involved in glaucoma.** High IOP and low ocular perfusion pressure induce a series of signaling cascades, such as axonal transport deficits, neurotrophic factor deprivation, oxidative stress, excessive excitotoxicity, local ischemia, and glial/astrocyte activation, ultimately leading to the programmed death of RGCs. ONH, optic nerve head; IOP, intraocular pressure; OHT, ocular hypertension; RGCs, retinal ganglion cells. Figure created by Biorender.com (<https://biorender.com/>).

## 1.4 Aging

It is well known that aging is one of the most important risk factors for many neurodegenerative disorders, including stroke, Parkinson's disease (PD), and Alzheimer's disease (AD). Its prevalence continues to rise with advancing age (Hou et al. 2019). In addition, aging is associated with physical deterioration, which increases susceptibility to illness and death (Rose 2009). However, nowadays the pathological mechanisms underlying aging are still poorly understood. Thus, there remain limited or no effective therapies for aging-related neurodegenerative diseases, which have a tendency to advance irreversibly at great cost to individuals and society.

The impacts of aging on the brain are multifaceted and profound. Given that neurodegenerative diseases are very common in elderly people and that completely disease-free brains are rare, it is appealing to consider neurodegenerative diseases as manifestations of accelerated aging. However, this simplification does not help to capture the underlying mechanisms between neurodegeneration and aging (Wyss 2016). The progression of aging should be determined by the interaction of environmental and genetic factors (Rodríguez et al. 2011). To better understand the biological and cellular changes during the aging process, López et al. defined nine common hallmarks and classified them into three groups: primary, antagonistic, and integrative hallmarks. The primary hallmarks consist of genomic instability, telomere attrition, epigenetic alterations, and loss of proteostasis. They are thought to be the primary drivers of aging and leading causes of functional decline. The antagonistic hallmarks indicate compensatory or antagonistic reactions to primary damage, including mitochondrial dysfunction, cellular senescence, and deregulated nutrient sensing. Their function depends primarily on intensity, exerting beneficial effects at low levels and becoming detrimental at high levels. The integrative hallmarks serve as a result of primary and antagonistic damages associated with senescence and comprise stem cell exhaustion and impaired intercellular communication (López et al. 2013). Since most of the cells in the CNS are post-mitotic, it is particularly sensitive to the effects of aging due to the cumulative damage with age and the lack of multiple forms of DNA repair (Chow and Herrup 2015). Notably, the alterations mentioned above are very common in these cells, indicating that analogous mechanisms could, to some extent, interpret diverse age-related neurodegenerative diseases. However, it remains unclear why neurons respond differently to similar environmental and genetic stimuli and develop different outcomes, such as normal aging or different neurodegenerative diseases. This further requires early



identification of presymptomatic manifestations in neurodegenerative diseases and exploration of the pathophysiological basis to avoid irreversible cellular changes.

Axonal degeneration, an early and prominent characteristic in neurodegenerative diseases, is prevalent in normal aging (Adalbert and Coleman 2013). In fact, numerous age-related alterations in cellular processes have been demonstrated to contribute to axonopathy, in which defects in axonal transport are involved and play an important role (McQuarrie et al. 1989; Millecamps and Julien 2013; Minoshima and Cross 2008). Therefore, studying axonal transport deficits may have practical implications for further understanding the molecular mechanisms that drive individuals to develop neurodegenerative diseases in old age.

Essential intracellular cargos in neuronal cells are heavily dependent on efficient transport within axons, for example, mitochondrial assembly to regions of high energy demand, autophagosome-mediated clearance of damaged organelles and mRNA trafficking for local translation (Mattedi and Vagnoni 2019). Recent advances in real-time imaging have allowed a clearer picture of how neuronal trafficking is coordinated in the aging organisms. Mitochondria are the most interesting cargos to study during aging since they provide energy for biochemical reactions in cells. Besides, their functions are tightly connected to efficient transport. Takihara et al. described mitochondrial transport in different age groups of mice through the so-called "MIMIR" technique (Minimally Invasive In Vivo Imaging of Mitochondrial Axonal Transport in RGCs). Although the total organized transport pattern remained unchanged in normal aged RGCs (23–25 months old), dynamic properties (including duration, distance, duty cycle, and velocity) were significantly reduced compared to adult mice, while the mitochondrial-free zones increased with aging (Takihara et al. 2015). Aged-dependent decline in mitochondrial transport was also found in dorsal root ganglia neurons (DRGs) derived from 5-month-old mice overexpressing tau P301S compared to those cultured from young mice of the same genotype (Mellone et al. 2013). Similarly, autophagy defects also exist with aging. A recent study showed that pronounced stalling of autophagosome biogenesis was noticed in cultured DRGs from aged mice, even though the early stages of autophagosome formation were not affected (Stavoe et al. 2019). However, transport impairment does not appear to be a ubiquitous characteristic of neuronal aging. Sleight et al. reported no change in the transport of signaling endosomes displayed by the toxic binding fragment of tetanus neurotoxin (HcT) in mice older than 13 months (Sleight and Schiavo 2016). Thus, the distinct kinetics of these cargos during aging may be the result of their intrinsically different pathophysiological properties.

However, more detailed and precise work is still required to identify the significance of cargo transport dynamics during aging.

## 1.5 Autophagy

As a highly conserved pathway of lysosomal degradation responsible for controlling the quality of cytosolic proteins and organelles, autophagy is widely considered to be important for maintaining axonal homeostasis in neurons (Wang et al. 2018). Recently, growing evidence has suggested that autophagy dysfunction is closely linked to axonal degeneration in most neurodegenerative diseases.

Broadly speaking, there are three major categories of autophagy, including chaperone-mediated autophagy (CMA), microautophagy, and macroautophagy (Parzych and Klionsky 2014). Although all three processes deliver cellular cargos to the lysosome for degradation and recycling, each has unique morphological features. Chaperone-mediated autophagy utilizes chaperones to selectively recognize cargo proteins containing a specific targeting motif (Kaushik and Cuervo 2018). During microautophagy, internalization of cytoplasmic cargo into the lysosome is facilitated by invagination or protrusion of the lysosomal membrane (Mijaljica et al. 2011). Macroautophagy involves the formation of double-membrane autophagosomes to sequester and deliver cargos to lysosomes (Stavoe AKH and Holzbaur 2019a). Among them, macroautophagy is considered the principal mechanism of catabolism and has been widely explored. In this case, the succeeding section of this dissertation shall direct its attention toward expounding on the mechanism of macroautophagy, henceforth named as autophagy.

Autophagy widely exists in eukaryotic cells. It is in charge of the turnover of targeted proteins and unwanted cellular organelles, thereby contributing to intracellular recycling (Menzies et al. 2015). Over the last two decades, our understanding of the process and molecular machinery of autophagy in yeasts and mammalian cells has grown dramatically. Mechanistically, the formation of autophagosomes involves a series of interconnected steps, including initiation, elongation, closure and degradation (Figure 3) (Melia et al. 2020; Wang et al. 2018). After activation of autophagy, a cup-like single-membrane structure termed the phagophore appears and enwraps degraded substrates in the cytoplasm. It gradually elongates and evolves into a closed, double-membrane autophagosome. Upon completion, autophagosomes mature after fusion with lysosomes to degrade sequestered materials and eventually release catabolic products (Xie and Klionsky 2007; Yang Z and Klionsky 2010). Simultaneously, most autophagy-related

genes (ATG) have been recognized to participate in autophagy biogenesis (Figure 3). The Atg1/Unc-51-like kinase 1 (ULK1) complex is the most upstream regulator of the autophagy pathway, including the kinase ULK1, ATG13, ATG101, and the focal adhesion kinase family-interacting protein of 200 kDa (FIP200) (Melia et al. 2020). It serves as an initiator of autophagy and further recruits other autophagic proteins to the putative nucleation site of autophagosomes (Parzych and Klionsky 2014). Next, the activated ULK1 complex facilitates autophagy by targeting the class III phosphatidylinositol 3-kinase (PI3K) complex, composed of vacuolar protein sorting 34 (VPS34), VPS15, ATG14L, and Beclin 1 (Menzies et al. 2015). Structurally, this complex is stabilized by the pairwork of Beclin 1/ATG14L and Vps15/Vps34 (Stjepanovic et al. 2017). Subsequent to the initiation of autophagy, Beclin 1 recruitment triggers the assembly of complexes mediated by the adaptor ATG14L, in which the WD structural domain of Vps15 arranges the proteins into the complex, thus enabling Vps34 function (Grasso et al. 2018). In the meantime, ULK1 enhances the PI3K activity of the catalytic subunit Vps34 through phosphorylation of Beclin 1 (Ser14) and ATG14L (Ser29), leading to increased phosphatidylinositol 3-phosphate (PI3P) production (Russell et al. 2013). Herein, the local enrichment of PI3P in the ER, as a signaling lipid needed for the assembly of downstream autophagic effectors, is of critical importance during the initial phases of autophagy (Wirth et al. 2013).

Afterward, a series of steps involves the elongation of the autophagic membrane, mainly relying on two ubiquitin-like conjugation systems: the Atg12–Atg5–Atg16L system and the microtubule-associated protein 1 light chain 3 (LC3)/Atg8 system (Wang et al. 2018). ATG12 is conjugated to ATG 5 through enzymatic reactions involving ATG 7 and ATG 10, and the resulting complex non-covalently binds to ATG16L1 (Noda et al. 2013). Subsequently, the formed Atg12–Atg5–Atg16L complex interacts with pre-autophagosomal membranes and promotes their elongation with the aid of LC3 recruitment (Menzies et al. 2017). In the LC3/Atg8 ubiquitin-like conjugation system, LC3 is first processed by ATG4B, which cleaves the C-terminus to form LC3-I. This cleavage is then critical for the conjugation of cytosolic isoform LC3-I with phosphatidylethanolamine (PE) to produce the lipidated isoform LC3-II by means of ATG3, ATG7, and ATG12-ATG5-ATG16L1. LC3-II is intimately linked to the extension of autophagosomal membranes and retained on completed autophagosomes, while the ATG12–ATG5–ATG16L complex dissociates from the membrane prior to the completion of autophagosome formation (Menzies et al. 2017; Nikolettou et al. 2015; Wang et al. 2018). Therefore, it is widely accepted that LC3-II is a standard autophagy

marker to monitor autophagy. Additionally, p62/sequestosome 1 (SQSTM1), a selective receptor for autophagy, links to polyubiquitinated cargos through the ubiquitin-associated domain (UBA) and delivers them to the autophagic machinery for degradation (Liu et al. 2016). Consequently, p62 indirectly reflects autophagy activity as an autophagy substrate, and its level is inversely correlated with autophagy activation (Bjørkøy et al. 2009).

Strikingly, unlike nonneuronal cells, several studies on neuronal autophagosome biogenesis, mainly *in vitro*, have described that autophagosomes are preferentially formed at the axon tip, thus emphasizing their highly compartmentalized and spatially regulated nature (Maday and Holzbaur 2014). Once formed, the newly generated double-membrane autophagosomes interact with microtubules. After an initial transient period of bidirectional motility, they subsequently undergo a unidirectional, highly progressive retrograde transport toward the soma at an average speed of 0.45  $\mu\text{m/s}$ , with very few anterograde movements observed (1%) (Maday et al. 2012). However, all these data on autophagosome transport were generated in *in vitro* models and so far, no imaging of autophagosome transport *in vivo* has been published.

Generally speaking, trafficking in autophagosomes is mediated by two major classes of motor proteins. Kinesin-1 is the plus-end-directed motor protein driving cargos to the cell periphery, whereas the dynein-dynactin complex is the major motor protein that delivers cargos to the perinuclear region (Nakamura and Yoshimori 2017). Meanwhile, nascent autophagosomes mature in transit from distal axons to the soma by fusing with lysosomes to form autolysosomes (Stavoe AKH and Holzbaur 2019a). Mechanistically, the fusion requires three distinct groups of protein families: Rab GTPases, membrane-tethering complexes and soluble N-ethylmaleimide-sensitive factor attachment protein receptors (SNAREs). Rab proteins exhibit specific localization to lysosomal membranes and serve to enlist tethering complexes, which function as molecular bridges to connect fusion-related components and facilitate their interaction. SNARE proteins direct the two corresponding membranes toward each other and provide the driving force, ultimately achieving membrane fusion (Chen YA and Scheller 2001; Nakamura and Yoshimori 2017). After fusion, acidification is induced and becomes increasingly acidic, which allows for the efficient digestion of cargo and the recycling of nutrients by lysosomal enzymes, such as hydrolases (Zhao et al. 2021).

In summary, autophagy is a conserved process of catabolic trafficking that involves massive destruction and the routine turnover of cytoplasmic components through regulated degradation of lysosomes (Martinet et al. 2009; Menzies et al. 2015).

Autophagy usually occurs at low levels, but it can be induced by a number of stress conditions, such as starvation and hypoxia (King et al. 2011). Numerous studies have described that autophagy may play a double-edged role in several diseases, including neurodegenerative diseases (Lee 2009). On the one hand, autophagy acts as a self-phagocytic pathway that facilitates cellular survival under unfavorable situations; on the other hand, excessive autophagy can induce cell death through immoderate self-cannibalization of vital cellular components, thereby exhausting cellular synthetic capacity (Martinet et al. 2009). Since neurons have permanent post-mitotic properties, polarized morphology, and actively engaged protein trafficking, they are heavily reliant on functional autophagy (Horton and Ehlers 2003; Lee 2009). Accumulated autophagosomes have often been found in a range of neurodegenerative disorders, such as Alzheimer's, Parkinson's diseases, and amyotrophic lateral sclerosis as well as acute CNS injuries (Guo et al. 2018; Jaeger und Wyss 2009). However, it still remains unclear if autophagy exerts either a protective or deleterious effect on neurodegenerative diseases. Therefore, understanding the molecular mechanisms of neuronal autophagy and the specific role of autophagy in neurodegenerative diseases may offer opportunities to develop therapeutic interventions resulting from the modulation of this process.

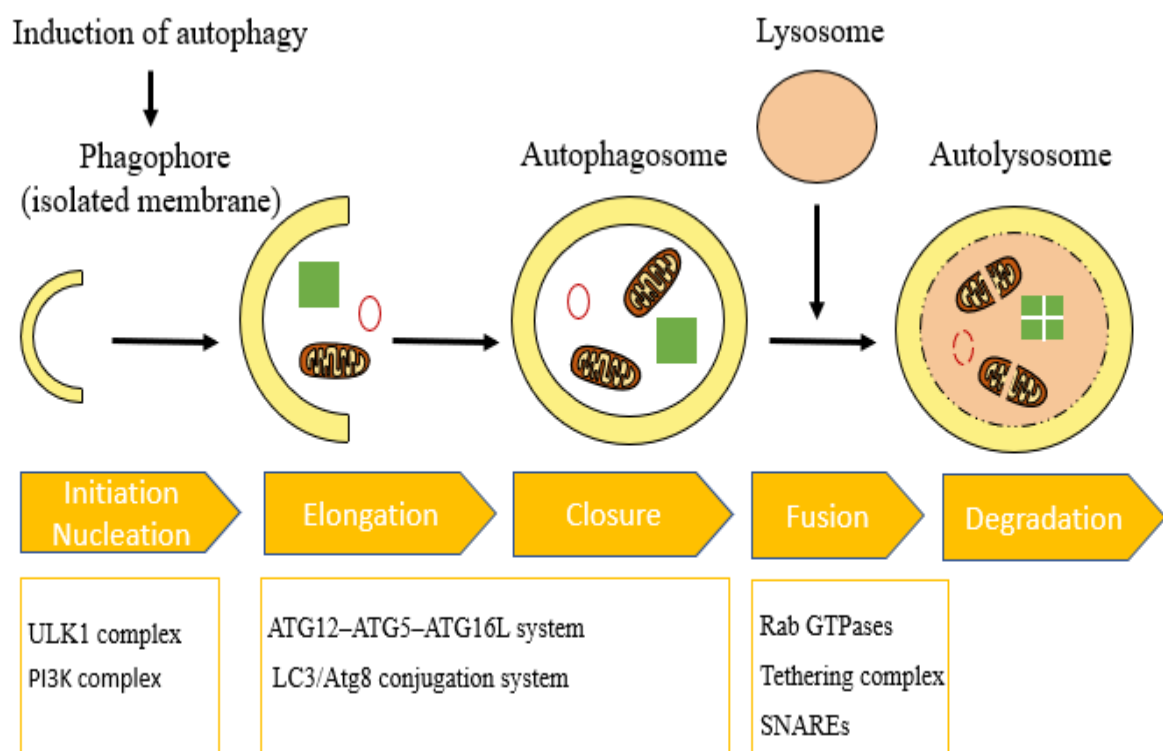


**Figure 3: Schematic diagram of the autophagic process in mammals.** Briefly, the autophagy pathway consists of several steps: initiation, nucleation, elongation, closure, maturation, and degradation. Cytoplasmic components are first recruited to an isolated membrane called phagophore, which then progressively develop into a dual-membrane autophagosome and thereafter mature into an autolysosome

following fusion with lysosomes. This process is initiated by the ULK1 complex, including ULK1, Atg13, FIP200, and Atg101. Autophagosome elongation contains two ubiquitin-like conjugation systems: the ATG12–ATG5–ATG16L system and the microtubule-associated protein 1 light chain 3 (LC3)/Atg8 system. Finally, the cargos sequestered within autophagosomes are subject to degradation via lysosomal enzymes and released as small molecules.

## 1.6 Aims of this thesis

Autophagy is strongly involved in the pathology of neurodegeneration. On the other hand, it is also important to maintain metabolic homeostasis and serves a crucial regulatory function in cell survival and death, mainly depending on the specific environment. The axon is at center stage in the early pathophysiology of most neurodegenerative conditions. Autophagosomes need to be transported along the axon for proper clearance of their contents and recycling processes. So far, it is not known, how autophagosomes are transported along the axon, in particular in neurodegeneration. Given that axonal transport defects of other cargos precede neuronal structural alterations, further elucidation of the axonal transport patterns of autophagosomes in different models of neurodegeneration may potentially promote the advancement of targeted therapeutic interventions. Therefore, the aim of this thesis was to analyze how autophagy contributes to different models of neurodegeneration.

As a prerequisite for all subsequent experiments, the first objective of this study was to construct an AAV-LC3 viral vector labeled with fluorescence to visualize autophagosome transport. Its toxicity and transduction efficiency *in vitro* and *in vivo* were assessed, and the most suitable titer was then selected for the following experiments.

The second goal was to explore the dynamic changes of autophagosome transport at different time points in the acute axonal injury model *in vitro* and *in vivo*, the rat subacute glaucoma model, and the aging model and further compare their similarities and differences.

Thirdly, focusing on the *in vivo* and *in vitro* models of acute axonal degeneration, the alterations in the autophagy-lysosomal pathway were evaluated from different perspectives, including the levels of relevant autophagic proteins, the ratio of autophagosome-lysosome fusion and degradative capacity, thus laterally validating the findings of the second step.

Finally, potential molecules regulating the process of autophagosome transport were investigated, especially several closely related key motor proteins.

## 2 Materials and Methods

### 2.1 Materials

#### 2.1.1 Animals

Embryonic day 18 (E18) Wistar rats were acquired from the Central Animal Facility, University Medical Center Göttingen, Germany, for the preparation of primary neuronal cultures. All female rats used for in vivo experiments with a body weight of 250-350g were from Charles River laboratories, Germany.

All animal experiments were carried out in compliance with the approved experimental animal licenses (11/0408 and 17/2642) issued by the responsible animal welfare authority (Niedersächsisches Landesamt für Verbraucherschutz und Lebensmittelsicherheit) and overseen by the local animal welfare committee of the University Medical Center Göttingen, Germany. Additionally, all animal experiments adhered to the principles and requirements set forth in the ARRIVE guidelines.

#### 2.1.2 Chemicals

**Table 1: Chemicals**

Chemicals	Company
B -27™ supplement	Thermo Fisher Scientific, Waltham, MA, United States
Brain-derived neurotrophic factor (BDNF)	PeproTech, Rocky Hill, NJ, USA
Boric acid	Carl Roth, Karlsruhe, Germany
Bovine serum albumin (BSA)	Sigma-Aldrich, St. Louis, Missouri, USA
Bromphenol blue	Sigma-Aldrich, St. Louis, Missouri, USA
Cell conditioning solution cc1	Ventana Medical Systems, Innocation park drive tucson, Arizona, United States
Ciliary neurotrophic factor (CNTF)	PeproTech, Rocky Hill, New Jersey, USA
Complete protease inhibitor	Roche, Basel, Switzerland
DAPI	AppliChem, Darmstadt, Germany
Dako antibody diluent	Agilent, Carpinteria, CA, United States
Deoxyribonuclease (DNase) I	Sigma-Aldrich, St. Louis, Missouri, USA
Dithiothreitol (DTT)	Sigma-Aldrich, St. Louis, Missouri, USA
DMEM Low Glucose	Biowest, Nuaille, France

<b>Chemicals</b>	<b>Company</b>
Dimethyl sulfoxide (DMSO)	AppliChem, Darmstadt, Germany
Ethanol absolute (molecular biology grade)	AppliChem, Darmstadt, Germany
ECL Prime Western Blotting Detection Reagents	Cytiva, Amersham, UK
Fetal calf serum (FCS)	Merck, Darmstadt, Germany
Glutamax	Thermo Fisher Scientific, Waltham, Massachusetts, USA
H <sub>2</sub> O <sub>2</sub>	Sigma-Aldrich, St. Louis, Missouri, USA
Hank's balanced salt solution (HBSS)	Thermo Fisher Scientific, Waltham, Massachusetts, USA
Laminin	Sigma-Aldrich, St. Louis, Missouri, USA
Luminol	Merck, Darmstadt, Germany
Methanol	AppliChem, Darmstadt, Germany
NaCl	Merck, Darmstadt, Germany
NaHCO <sub>3</sub>	AppliChem, Darmstadt, Germany
Neurobasal medium	Thermo Fisher Scientific, Waltham, Massachusetts, USA
Pepstatin A, BODIPY™ FL Conjugate	Thermo Fisher Scientific, Waltham, Massachusetts, USA
Penicillin/streptomycin/neomycin (PSN)	Thermo Fisher Scientific, Waltham, Massachusetts, USA
Penicillin-Streptomycin (PS)	Sigma-Aldrich, St. Louis, Missouri, USA
Phosphatase inhibitor	Roche, Basel, Switzerland
Phosphate buffered saline (PBS)	AppliChem, Darmstadt, Germany
Pierce™ bicinchoninic acid (BCA) Protein Assay	Thermo Fisher Scientific, Waltham, Massachusetts, USA
Poly-L-ornithine (PLO)	Sigma-Aldrich, St. Louis, MO, United States
PageRuler Plus Prestained Protein Ladder	Thermo Fisher Scientific, Waltham, Massachusetts, USA
Radioimmunoprecipitation assay buffer	Thermo Fisher Scientific, Waltham, Massachusetts, USA
Sodium dodecyl sulfate (SDS)	AppliChem, Darmstadt, Germany
HoloTransferrin	AppliChem, Darmstadt, Germany
Tris	AppliChem, Darmstadt, Germany
Trypsin	Sigma-Aldrich, St. Louis, Missouri, USA
Triton X100	AppliChem, Darmstadt, Germany



### 2.1.3 Buffers, solutions, and their recipes

**Table 2: Buffers and solutions recipes**

Buffer/solution/medium	Constituents
Calcium magnesium-free (CMF)	50 mL 10x HBSS, 7.5% NaHCO <sub>3</sub> , in 450 mL sterile distilled H <sub>2</sub> O, pH 7.4
Cortical medium	0.25% glutamax, 0.5% 1 mg/mL holo transferrin, 1% PSN, 2% B-27 supplement in neurobasal medium
Astrocyte medium	DMEM low glucose medium, 2.5% PS, 20% FCS
BODIPY FLpepstatin A	1 $\mu$ M BODIPY FLpepstatin A in DMSO
Enhanced chemiluminescence (ECL) reagent 1	100 mL 250 mM luminol, 44 $\mu$ L 90mM p-coumaric acid, 1mL 1 M Tris pH 8.5 in 8.85 mL distilled H <sub>2</sub> O
ECL reagent 2	0.6 $\mu$ L 30% H <sub>2</sub> O <sub>2</sub> , 1mL 1 M Tris pH 8.5 in 9 mL distilled H <sub>2</sub> O
Electrophoresis buffer	190 mM glycine, 25 mM Tris, in distilled H <sub>2</sub> O
Laemmli buffer	312.5 mM Tris pH 6.8, 10% SDS, 50% glycerine, 0.005% bromphenol blue, 100 mM DTT
Lysis buffer	91% RIPA buffer, 5% complete protease inhibitor, 4% phosphatase inhibitor
PBS	9.5 mg/mL PBS in distilled H <sub>2</sub> O
Tris-buffered saline (TBS)	20 mM Tris, 137 mM NaCl in distilled H <sub>2</sub> O
TBS-Tween-20 (TBS-T)	0.1% Tween-20 in TBS, pH 7.6
Transfer buffer	190 mM glycine, 25 mM Tris, 20% methanol

### 2.1.4 Viral vectors

**Table 3: Viral vectors**

Viral vectors	Source
AAV6-mScarlet-LC3	provided by Prof. Uwe Michel, Department of Neurology, University Medicine Göttingen
AAV1/2-hSyn-EGFP [Genbank ID: HQ416702]	provided by Prof. Uwe Michel, Department of Neurology, University Medicine Göttingen

## 2.1.5 Antibodies

**Table 4: Primary antibodies**

Antibody	Species	Catalog number	Company
anti-Cathepsin D	mouse	377124	Santa Cruz, Dallas, TX, United States
anti-Dynein	mouse	MMS-400p	Covance, North Carolina, United States
anti-GAPDH	mouse	5G4	Hytest Ltd., Turku, Finland
anti-LC3B	rabbit	L7543	Sigma-Aldrich, St. Louis, Missouri, United States
anti-p150Glued	mouse	610474	BD Biosciences, New Jersey, United States
anti-p62	rabbit	P0067	Sigma-Aldrich, St. Louis, Missouri, United States
anti-p-ATG16L1	rabbit	195242	Abcam, Cambridge, United Kingdom
anti-Kif 5	rabbit	3500282	Sigma-Aldrich, St. Louis, Missouri, United States
anti-SMI 32	mouse	801701	Bio legend, San Diego, California, United States

**Table 5: Secondary antibodies**

Antibody	Species	Catalog number	Company
anti-mouse HRP	horse	7076P2	Cell Signaling Technology, Cambridge, United Kingdom
anti-rabbit HRP	goat	7074P2	Cell Signaling Technology, Cambridge, United Kingdom
anti-mouse Alexa647	donkey	21447	Thermo Fisher Scientific, Waltham, Massachusetts, USA
anti-mouse Alexa594	goat	11005	Thermo Fisher Scientific, Waltham, Massachusetts, USA
anti-rabbit Alexa546	donkey	A10040	Thermo Fisher Scientific, Waltham, Massachusetts, USA
anti-rabbit Star635p	goat	1002	Abberior, Gottingen, Germany

## 2.1.6 Equipment

**Table 6: Equipment**

Equipment	Company/manufacturer
10-0 polyamide surgical suture	Ethicon, New Jersey, United states
Analytical balance BL210S	Sartorius, Göttingen, Germany
Balance LE6202S	Sartorius, Göttingen, Germany
Blotting paper Whatman	GE Healthcare, Chicago, IL, USA
Cryostat CM3050 S	Lecia, Wetzlar, Germany
Centrifuge 5418 R	Eppendorf, Hamburg, Germany
CO <sub>2</sub> incubator HERAcell 150i	ThermoFisher Scientific, Waltham, Massachusetts, USA
Cryomatrix gel	Epredia, Michigan, USA
Drying oven (37°C, 60°C)	Heraeus, Hanau, Germany
Electric drill	Proxxon, Micromot NG2/S, Föhren
Electrophoresis power supply	GE Healthcare, Chicago, IL, United States
FluoroDish 35-100	World precision instruments, Sarasota, FL, United States
Forceps	Fine Science Tools, Heidelberg, Germany
Freezer (-20°C)	Bosch, Stuttgart, Germany
Freezer (-80°C)	Ewald innovationstechnik, Rodenberg, Germany
Fridge (+4°)	Gorenje, Velenje, Slovenia
Fusion solo s	Vilber Lourmat, Eberhardzell, Germany
Glass coverslips	R.Langenbrinck, Emmendingen, Germany
Ice machine AF107	Scotsman Ice Systems, Vernon Hills, IL, United States
Observer Z1 Inverted Phase Contrast Fluorescence Microscope	Carl Zeiss Microscopy, Jena, Germany
AXIO Imager.Z2 Motorized Fluorescence Microscope	Carl Zeiss Microscopy, Jena, Germany
Inverted light microscope Axiovert 40C	Carl Zeiss Microscopy, Jena, Germany
Laminar flow hood LaminAir HB 2448	Heraeus, Hanau, Germany
Low-temperature cautery	Bovie Medical Corporation, Florida, USA
Microfluidic chambers RD450	Xona, California, United States
Mini-PROTEAN® TGX™ Precast Protein Gels (4–15%)	Bio-Rad, Hercules, CA, United States
Multimode microplate reader Spark 10M	Tecan, Männedorf, Switzerland

<b>Equipment</b>	<b>Company/manufacturer</b>
Parafilm	Bemis, Neenah, WI, United States
Pipette tips	STARLAB, Hamburg, Germany
Pipettes	Gilson, Middleton, WI, United States
Polyvinylidene difluoride (PVDF) transfer membrane	GE Healthcare, Chicago, IL, United States
Safe-lock tubes	Eppendorf, Hamburg, Germany
Scalpel	Aspen Surgical, Caledonia, MI, United States
Scissors	Fine Science Tools, Heidelberg, Germany
Shaker ST5	CAT, Staufen-Etzenbach, Germany
Thermocoagulator	Fine Science Tools, Heidelberg, Germany
Thermomixer comfort 1.5 mL	Eppendorf, Hamburg, Germany
Tono-Pen® Vet	Reichert, Depew, NY, United States
Two-photon microscope	LaVision BioTec TriM Scope, Bielefeld, Germany
Ultrasonic bath RK 100 H	BANDELIN electronic, Berlin, Germany
Ultrasonic homogenizer UP50H	Hielscher Ultrasonics, Teltow, Germany
Vertical Electrophoresis Cell	Bio-Rad, Hercules, CA, United States
Water bath 1003	GFL Gesellschaft für Labortechnik, Burgwedel, Germany
Water purification system Arium pro	Sartorius stedim, Göttingen, Germany

### 2.1.7 Software

**Table 7: Software**

<b>Software</b>	<b>Company</b>
Endnote X8	Clarivate Analytics, Philadelphia, PA, United States
Excel 2019	Microsoft, Redmond, WA, United States
EvolutionCapt Plus 6	Vilber Lourmat, Eberhardzell, Germany
GraphPad Prism 8	GraphPad Software, La Jolla, CA, USA
ImageJ	National Institutes of Health, Bethesda, MD, United States
ImSpector	LaVision, Göttingen, Germany
PowerPoint 2019	Microsoft, Redmond, WA, United States
Word 365	Microsoft, Redmond, WA, United States
ZEN 2.5 pro	Carl Zeiss Microscopy, Jena, Germany

## 2.2 Methods

### 2.2.1 cDNA Cloning and production of adeno-associated viral vectors

The cDNA cloning and construction of AAV vectors were done by Elisabeth Barski, Barbara Müller, and Prof Dr. Uwe Michel (Department of Neurology, University Medical Center Göttingen).

Briefly, rat LC3 cDNA was amplified and labelled with a basic red fluorescent protein mScarlet and finally packed into the AAV6 vector. Expression of LC3-mScarlet was controlled by a hybrid cytomegalovirus (CMV) /chicken beta-actin (CB) promoter and further augmented by a woodchuck hepatitis virus post-transcriptional regulatory element (WPRE). Before production of AAV vectors, the sequence of all plasmids was confirmed. The resulting AAV vectors were termed as AAV6-mScarlet-LC3 and detailed information was shown below (Figure 4).



**Figure 4: Vector diagram of AAV6-mScarlet-LC3.** As an adeno-associated viral vector, it expresses mScarlet fluorophores fused to LC3. ITR: AAV-6 inverted terminal repeat. CB: chicken beta-actin. CMV: cytomegalovirus promoter. WPRE: woodchuck hepatitis virus posttranscriptional regulatory element. bGH-pA: bovine growth hormone- polyadenylation site.

### 2.2.2 Neuronal cell culture in microfluidic chambers

Embryos of the Wistar rat at E18 were used to prepare primary cortical neurons. All procedures were approved by the local government authorities in accordance with the regulations of the animal research council of Lower Saxony, Germany.

#### 2.2.2.1 Preparation of microfluidic chambers

Duct tape was used to carefully remove dust and cell debris from microfluidic chambers, especially in main channels and microgrooves. Then cleaned microfluidic chambers were immersed in 70% undenatured ethanol with microgrooves up at least 10 minutes for sterilization. After complete drying under a cell culture hood, the chambers were ready for the next step.

### 2.2.2.2 Coating with poly-L-ornithine and laminin

In all in vitro experiments, Petri dishes were used and covered with PLO and laminin under the sterile hood of cell culture. PLO was first dissolved in 0.15 M sodium borate buffer at pH 8.5 resulting in a 1 mg/ml stock solution stored in a refrigerator at 4 °C. PLO was then diluted ten times with sterile double-distilled water to a final concentration of 0.1 mg/ml. 1 ml of this PLO solution was pipetted into the middle of Petri dishes and left in the hood at room temperature overnight. After washing the dishes twice with sterile double-distilled water, 1 ml of diluted laminin was applied to the dishes at a concentration of 1 g/mL. Then, the dishes were transferred into an incubator at 37 °C for at least 2 hours. After aspiration of the laminin solution and multiple washings with sterile double-distilled water, the microfluidic chambers described in 2.2.2.1 were carefully placed in the center of Petri dishes with sterile forceps. Subsequently, the chambers were gently pressed with fingers to ensure they adhered well to the dishes. At last, 180 µL of the pre-warmed cortical medium was introduced into the somatic compartment through the main channels, while the axonal compartment was filled with 120 µL of cortical neuron medium the next day. All dishes were stored in a 37 °C cell incubator until the seeding of neurons.

### 2.2.2.3 Primary cortical neuron culture and cell seeding

The rat primary cortical neurons were prepared by Elisabeth Barski (Department of Neurology, University Medical Center Göttingen).

Pregnant E18 Wistar female rats were euthanized with carbon dioxide (CO<sub>2</sub>) and pinned to a prepared pad. The skin covering the abdomen underwent disinfection with a 70% ethanol solution, after which an incision was made to expose the peritoneal cavity. All embryos were carefully taken out of the uterus and immediately placed in a pre-cooled CMF buffer on a clean bench with laminar flow. After decapitation, brain dissection and isolation of cortices were performed under a stereomicroscope to achieve precise identification in another petri dish with ice-cold CMF. To be more detailed, both hemispheres of brains were exposed and meninges were carefully removed. Cortical regions from both hemispheres were isolated, collected, and subsequently put into a Falcon tube containing 10 ml of ice-cold CMF. After aspiration of CMF, the cortices were subjected to the addition of 1 mL of trypsin (25,000 U/mL), followed by placement in a 37 °C water bath for 15 minutes. During the last 5 minutes of the water bath, 50 µL of DNase I (5 mg/mL) were supplemented. Afterward, the Falcon tube was centrifuged at 800 rpm for 1 minute at room temperature (RT). The supernatant was immediately discarded and 1 mL FCS was used to stop trypsin activities. Then, a homemade fire-

polished glass Pasteur pipette was used to gently triturate the pellets. Following centrifugation of cell suspension at 800 rpm for 4 minutes, the supernatant was removed and the resulting pellet was re-suspended by 1ml of warm culture medium. 10  $\mu$ L of cell suspension was introduced into both sides of a Neubauer counting chamber for cell counting. Before seeding cells in the microfluidic chambers, all of the medium within the wells of the somatic compartments was thoroughly sucked out. 60,000 neurons were directly added to the somatic compartment of microfluidic chambers through main channels. 1 hour later, 200  $\mu$ L of the pre-warmed cortical medium was introduced to the wells located in the somatic compartment of the microfluidic chambers. All chambers together with the dishes were subsequently maintained at 37°C under an environment comprising 5% CO<sub>2</sub> and 95% humidity.

#### 2.2.2.4 Test of virus toxicity and transduction efficacy

The AAV-mScarlet-LC3 virus was tested for toxicity and transduction efficacy on primary cortical neurons. At least 3 hours after seeding 60,000 cortical neurons in microfluidic chambers, LC3 virus was diluted at different titers in 200  $\mu$ L of fresh pre-warmed cortical medium ( $0.5 \times 10^6$  transduction units (TU),  $1 \times 10^6$  TU,  $2 \times 10^6$  TU). Neurons were transduced by drop-wise addition of the viral vector. On day in vitro (DIV) 2, half of the medium was removed from the somatic and axonal compartments and substituted with new, pre-warmed cortical medium. Further replacement of medium happened every two days until neurons were imaged. On DIV5, some axons were long enough to cross through microgrooves and enter the axonal compartment. On DIV10, cortical neurons were visualized using a Zeiss inverted microscope with a special cell incubation system to maintain 37 °C and 5% CO<sub>2</sub> concentration. Photomicrographs were taken under 40x magnification by using Zen software. For each viral titer, a minimum of two chambers including at least 4 view fields, was imaged through bright and DsRed filters (to image mScarlet fluorophore). The transduction rate was quantified by manually counting the number of neurons expressing mScarlet fluorescence in each field of view and then dividing it by the total number of neurons. Besides, the morphology of neurons and the number of dead cells were also checked as factors to reflex the toxicity of viral vector. A titer with a high degree of transduction but low toxicity was selected for subsequent in vitro experiments.

#### 2.2.2.5 Co-culture of cortical neurons and astrocytes

The rat primary astrocytes were prepared, harvested, and stored in liquid Nitrogen by

Elisabeth Barski (Department of Neurology, University Medical Center Göttingen).

Briefly, astrocytes stored in Dulbecco's Modified Eagle Medium (DMEM) complemented with 20% FCS and 10% dimethyl sulfoxide (DMSO) were taken out from the liquid nitrogen and slowly melted in a 37 °C water bath until a small piece of ice was left in the tube. All liquid inside was transferred into a 10ml falcon tube filled with 6-8ml neurobasal medium and then centrifuged at 800 rpm for 8 minutes at RT. The supernatant was discarded and substituted with pre-warmed astrocyte medium supplemented with 20% FCS. Astrocytes were counted through a Neubauer counting chamber. 30,000 astrocytes were seeded into the somatic compartment of microfluidic chambers. 1 hour later, 200  $\mu$ L of fresh, warm astrocyte medium was added to the wells in the somatic compartment of microfluidic chambers. The chambers were then placed within an incubator with 37°C and 5% CO<sub>2</sub>. Afterward, astrocytes were quickly checked every day under an inverted phase contrast microscope until the density reached one-third of the somatic compartment. Then 20,000 cortical neurons were directly seeded in the chambers as described in 2.2.2.3.

#### 2.2.2.6 Viral transduction and medium changes

After viral titer optimization,  $2 \times 10^6$  TU was determined to be the best condition due to its optimal transduction efficiency and low toxicity. In all following in vitro experiments, cells were transduced with this titer. Cell transduction was performed as described in 2.2.2.4. In primary cortical neuron culture,  $2 \times 10^6$  TU of LC3 virus was diffused in 200  $\mu$ L of cortical medium with 10% FCS and then pipetted into the somatic compartment of microfluidic chambers. At the same time, 20  $\mu$ L more medium was given to the axonal compartment to prevent neurons from entering the axonal side. However, the next day, the pressure gradient was reversed and maintained for the following several days until neurons were imaged on DIV 10 in order to let axons better elongate into axonal side of chambers. Additional changes were performed every two days. Each time, only half of the medium was replenished with fresh, pre-warmed medium. On DIV 4, brain-derived neurotrophic factor (BDNF) and ciliary neurotrophic factor (CNTF) were supplemented to cortical medium with 10% FCS according to a dilution ratio of 1:1000. On DIV 6, FCS was removed from the medium formula. Only cortical medium with BDNF and CNTF was applied until DIV 10.

In terms of the co-culture of cortical neurons and astrocytes, the viral transduction process and medium changes were the same as cortical neuron culture. Since astrocytes could support cortical neurons, all medium was serum-free. On DIV 11, neurons were imaged.



### 2.2.2.7 Axotomy

Due to the use of microfluidic chambers, selective axonal lesions were possible to achieve. On DIV 10-11, axons were axotomized by using a vacuum pump to completely suck out all medium in the axonal compartment through the main channel. Passing air bubbles in main channels caused the mechanical lesion of axons, thus inducing axonal degeneration. Afterward, the main channel was immediately replenished with 150  $\mu$ L of pre-warmed cortical medium with BDNF and CTNF as mentioned in 2.2.2.6. The chambers were quickly checked under an inverted light microscope to ensure all axons were successfully axotomized. If not, axotomy could be performed repeatedly. Afterward, chambers were placed in the microscope with a cell incubation system and then imaged as mentioned in 2.2.4.2.

### 2.2.2.8 Treatment with pepstatin A, BODIPY<sup>TM</sup> FL Conjugate

For co-culture of cortical neurons and astrocytes, a treatment with boron-dipyrromethene (BODIPY)-modified full-length (FL)-pepstatin A was performed. BODIPY-pepstatin A, a fluorophore-tagged pepstatin, is a novel tool widely used to detect cathepsin D distribution and trafficking in vitro since it is exclusively bound to active cathepsin D at the pH of 4.5 (Chen et al. 2000; Cheng et al. 2018). The substance was solubilized using DMSO and stored in a -20 °C freezer. On DIV 11, neurons were incubated with BODIPY-pepstatin A (1 $\mu$ M) for 1 hour at both somatic and axonal compartments of chambers in a cell incubator. The medium at both sides was then replaced to remove this fluorescent probe. Images were taken on the axonal side using an inverted microscope with an incubation system to trace the colocalization of active cathepsin D as determined by BODIPY-pepstatin A and mScarlet-LC3.

### 2.2.2.9 Recycling of microfluidic chamber

After all live imaging procedures, chambers were collected and repurposed for further experiments. Medium was first totally withdrawn from wells on both sides. Subsequently, the Petri dishes were then treated with 0.5% SDS and 70% ethanol to disinfect the AAV vectors. After washing with water, chambers were collected and immersed in a 50 mL beaker filled with double-distilled water for one week. Then all chambers underwent ultrasonic cleaning for 15 minutes to clear out cell debris. After drying at RT, the chambers were stored in clean Petri dishes for future use.

## 2.2.3 Live-cell microscopy and quantification

### 2.2.3.1 Real-time imaging of LC3 transport in degenerating axons in vitro

Primary cortical neurons cultured in microfluidic chambers and transduced with a mScarlet-LC3 viral vector were visualized with a Zeiss inverted fluorescent microscope outfitted with a cell incubation system to maintain 37 °C and 5% CO<sub>2</sub>. Autophagosome transport in axons labeled with mScarlet fluorophore was recorded under 40x magnification for 10 minutes at 5s intervals before, direct after, and every 2 hours until 6 hours after axotomy. In general, a minimum of two chambers including at least 3 view fields at each time point was imaged. However, selected areas differed before and after axotomy. Before axotomy, only axons with growth cones in the axonal compartment were imaged in order to distinguish transport direction, while for the time points after axotomy, microgrooves with clearly axotomized axons were recorded since after axotomy, only axons retracting back to microgrooves were considered as lesion-induced degenerating axons. All videos were carefully collected and then quantified.

### 2.2.3.2 Quantification of live-imaging in microfluidic chambers in vitro

In order to analyze the live-imaging in vitro, KymoAnalyzer, an open-source software, was used. It is a robust tool that automatically categorizes particle tracks and systematically computes a plethora of parameters, including moving lengths, speeds, and other characteristics of motor-driven transport from time-lapse live-imaging sequences (Neumann et al. 2017).

Briefly described, the KymoAnalyzer plugin was downloaded and installed in ImageJ. Time-lapse live-imaging was then imported into the software. In each video, a minimum of 3 axons was carefully tracked from the somal side to the axonal side using the polyline tool. Afterward, 2D kymographs were automatically generated. Then, particle trajectories were manually tracked. The position was recorded as coordinates in the x and y dimensions (distance and time, respectively). Following track assignments, netcargopopulation and netvelocities macro executed automatically and then displayed the final results. However, after axotomy, the motility of LC3 vesicles was damaged so that some of them moved very slowly. In this case, vesicles moving less than a net 5 μm within the 3-minute time frame (netvelocities  $\leq 0.028$  μm/s) were defined as bidirectional or stationary ones.

### 2.2.3.3 Imaging and quantification of BODIPY-pepstatin A and LC3 co-localization in vitro

Cortical neurons co-cultured with astrocytes were seeded in microfluidic chambers and

transduced with the mScarlet-LC3 viral vector. On DIV 11, BODIPY-pepstatin A was added to neurons and incubated for 1h. The medium was then replaced with fresh, pre-warmed cortical medium supplemented with BDNF and CNTF. In order to distinguish the single axon to which vesicles belonged, 3-minute videos were acquired on axonal sides before, direct after and every 2 hours until 6 hours after axotomy as described in 2.2.3.1. For colocalization analysis between active cathepsin D, as indicated by BODIPY-pepstatin A with EGFP fluorophore and mScarlet-LC3, the overlapped vesicles labeled with yellow signals were counted manually in individual axons and separately divided by the number of active cathepsin D and LC3 vesicles at each time points.

#### **2.2.4 Animal experiments**

Adult female rats provided by Charles River, weighing between 250-350g at an age of 3 months or beyond 18 months, were employed in vivo experiments. All animals were placed in a room with a temperature of  $22 \pm 2$  °C, a 12/12h light and dark cycle and free access to regular food and water. All operations on animals were undertaken with the permission of the local animal research council and according to the legislation of the State of Lower Saxony, Germany.

##### **2.2.4.1 Intravitreal injections of viral vectors**

Anesthesia was induced first with 5% isoflurane for 3 minutes, and then the flow rate was decreased to 3% for another 5 minutes until animal breaths became stable in a closed glass chamber. Afterward, 10% ketamine (95mg/kg) and 2% xylazine (7 mg/kg) were mixed and then injected intraperitoneally to maintain anesthetic state. Palpebral, corneal reflexes, and toe pinch were performed to assess if the level of anesthesia was sufficient. Only when animals were under deep anesthesia, intravitreal injections of the viral vector were administered at optimized titers 3-4 weeks prior to live imaging, leading to sufficient transduction of the retina without apparent toxicity under a stereotactic operating microscope.

In brief, the left eye bulb of the rat was well-exposed and fixed by forceps or the fingers of the left hand. The viral vector (AAV. CMV-mScarlet-LC3:  $5.4 \times 10^7$  TU per eye; AAV. hSyn-EGFP:  $1.23 \times 10^8$  TU per eye) was diluted to a volume of 5  $\mu$ L per eye in sterile PBS buffer. Intravitreal injections were then carried out using a Hamilton syringe at a distance of about 2 mm posterior to the corneal limbus. With the aid of continuous visual guidance to prevent injury to the lens and retina, the needle tip was cautiously positioned and directed toward the upper nasal quadrant. All substances were then

injected slowly over 1 minute. After about a 30-second interval, the needle was carefully retracted from the eye bulb. Ocular ointment was then rubbed on both eyes. Finally, animals were kept in a heating chamber and transferred to a quiet and dark room to let them wake up.

#### 2.2.4.2 Surgical exposure of the optic nerve

The surgery on the optic nerve was performed as reported before (Koch et al. 2011). The rat was first anesthetized. The head fur of the rat was then shaved off with a razor. Afterward, the rat was positioned on a heating cushion and stably fixed with a custom-made rat positioning system. Heart rate and peripheral oxygen saturation were continuously monitored during the surgery process. The anesthetic state was checked each hour with the methods described in 2.2.4.1. To maintain sufficient anesthesia, intraperitoneal (i.p.) injections were performed with the repetitive administration of a diminished dosage of Ketamine and Xylazine.

The following were the detailed steps of the procedure. A midline incision was made with a scalpel on the skin between the two eyes. The animal was then tipped 30° to the right and placed under a stereomicroscope. Afterward, the operation field close to the orbital rim was well exposed by retracting skins on both sides with four home-made hooks. Using a thermocoagulator, the orbita was opened, and the supraorbital vein was totally blocked. After covering the lacrimal gland with gauze swabs to protect the eye, a small electric drill was used to remove a part of the orbital bone for later objective positioning of live imaging. Physiological solution was then applied to clean the remaining bone chips. After removal of the lacrimal gland, the superior palpebral and rectus muscles were dissected and detached from their tendinous origins using coarse forceps. The eye was then rotated downwards. A fifth hook was put in the mass of muscles close to their insertion to fix the eye bulb. Care was taken to remove the connective tissue above the optic nerve and keep the central retinal artery intact. After exposure of the optic nerve sheath, the meninges wrapped around the optic nerve were removed layer by layer through the interactive use of fine forceps and scissors. Pre-warmed physiological solution was repetitively rinsed to clean remaining tissue fragments at the operation site.

#### 2.2.4.3 Crush lesion of the optic nerve

In the optic nerve crush lesion paradigm, a polyamide surgical suture (Ethicon, 10–0 Ethilon) was loosely placed approximately 1 mm proximal to the optic nerve for structural identification. After finishing real-time imaging of the basal state, the suture was firmly

knotted for 30 seconds to induce acute axonal degeneration.

#### 2.2.4.4 Establishment of the subacute glaucoma animal model

The glaucoma model was set up as reported before (Lani et al. 2019). The rats with an intravitreal injection of the mScarlet-LC3 viral vector were put under deep anesthesia through the administration of 10% ketamine (95mg/kg) and 2% xylazine as described in 2.2.4.1. Prior to starting the procedure, a hand-held tonometer (Tono-Pen® XL, Reichert) was used to measure the basal intraocular pressure (IOP) in both eyes. The rats were then placed in lateral decubitus position, and the left eyelid was kept apart by means of curved forceps. The eyeball was gently and carefully advanced forward for good exposure of the limbal vasculature. Afterward, the limbal plexus around the cornea was cauterized at 360° with a low-temperature ophthalmic cautery (Bovie Medical Corporation) through softly touching the blood vessels under a stereo Zeiss microscope. Great attention was paid to avoid damage to the periphery of the cornea. IOP measurements of both eyes were performed immediately after surgery to confirm the successful induction of ocular hypertension (OHT). Afterward, the optic nerve was surgically exposed for further live imaging of autophagosome transport as described in 2.2.4.2.

#### 2.2.4.5 Two-photon live imaging of axonal LC3 transport on the optic nerve

After exposing the optic nerve surgically, the orbital cavity received multiple washings with pre-warmed physiological solution until the solution became transparent. In vivo live imaging was then performed using a two-photon microscope (LaVision BioTec TriM Scope). The objective tip was immersed in the physiological solution. The objective position was sufficiently adjusted, even tilted ~15° to the right side of the rat, allowing the optical axis perpendicular to the labeled axons. Afterward, a conventional fluorescence microscope was used to locate the optic nerve through the suture mentioned in 2.2.4.3 as a structural marker. The labeled axons on the optic nerve were then properly aligned with the microscope. A minimum of mercury lamp intensity was applied in order to reduce photobleaching in this process. Once the microscope alignment was set up, the rat's position was carefully kept and not moved again.

By using a custom-built two-photon microscope, 200 real-time images of the optic nerve were acquired with ImSpector software. Briefly described, an optical parametric oscillator (chameleon, coherent) was used as the excitation source. The excitation wavelength of the mScarlet was continuously tuned at 1100 nm. Then, the emitted fluorescence signal was collected through a 40x immersion Zeiss objective and directed to a photomultiplier

tube (PMT) through a dichroic filter.

After the optic nerve crush injury, the imaging areas were selected about 500  $\mu\text{m}$  proximal to the reference suture, which was located at a 1mm distance from the bulbus as mentioned above. In order to reduce movement artifacts caused by animal breaths, a custom-built breath trigger was used. An accelerometer was placed at the area of maximum respiratory excursion in the upper lateral thorax of the rat to detect respiratory movements. A custom-built software synchronized respiratory movements of the animal with the image acquisition. Imaging frames were initiated with a delay of 0.2-0.4 s after the maximum respiratory excursion. The trigger delay varied based on the overall image stability, with a preference for short delays ( $\sim 0.2\text{s}$ ) at fast respiratory rates ( $>70/\text{min}$ ) and long delays ( $\sim 0.4\text{s}$ ) at slow respiratory rates (60/min). In addition, the frame duration was also adjusted according to the respiration rate, with values between 0.3 and 0.5s/Frame.

#### 2.2.4.6 Quantification of in vivo live imaging

The raw real-time live imaging was further processed for quantification using a custom-written macro set installed in Image J. Two parts were included in this macro set: in vivo tracking and Kymograph.

The live imaging was first registered into the macro and then stabilized in order to improve imaging quality. Under some circumstances, strongly shifted segments that could not be well stabilized were removed from the file using the “Create Sub-Stack” macro. Afterward, registered live imaging was converted to a projection file. A number of 10-20 axons per file were then carefully tracked from the proximal part to the distal part of the optic nerve and added as Regions of Interest (ROIs). By using “Kymograph” macro, all tracked axons were automatically transformed into Kymographs one by one, as described in 2.2.3.2. Stationary and motile trajectories of LC3 vesicles in each Kymograph were separately marked and added to the ROI-manager. After completion of all track assignments in each imaging sequence, the absolute number and velocity of different LC3 vesicles were executed automatically using the “Kymograph” macro. At last, the final results were displayed as excel files for further statistical analysis.

### 2.2.5 Immunohistochemistry

#### 2.2.5.1 Animal euthanasia and tissue processing

Four weeks prior to the surgery, AAV. hSyn-EGFP was intravitreally injected into both eyes to label the axons of bilateral optic nerves. as described in 2.2.4.1. Under deep

anesthesia, the optic nerves were then exposed, and crush injury was administered to the left optic nerve while the contralateral side acted as an internal control. After 6 hours, the rats were sacrificed with CO<sub>2</sub>. To preserve morphological structures, dissected optic nerves on both sides were removed, fixed with 4% paraformaldehyde (PFA) in PBS at 4°C overnight, and incubated into 30% sucrose solution for at least 48 h for dehydration. Afterward, optic nerves were longitudinally embedded in cryomatrix gel and sectioned using a Leica cryostat at a thickness of 16 µm. All sections were then completely dried in a 37°C oven and stored in a -20°C freezer until immunohistochemical staining.

#### 2.2.5.2 Immunohistochemical staining and quantification

To explore the colocalization of autophagosomes and lysosomes, double fluorescence staining of LC3 and cathepsin D was performed.

In brief, the frozen sections mentioned above underwent drying in a 37°C oven and then were rehydrated in TBS for 30 minutes. Afterward, sections were incubated in a TBS solution (PH = 9) at 50°C for 4 h to retrieve the antigen. Next, sections were quickly washed in TBS to remove antigen retrieval buffer, and 0.3M Glycin was used to quench autofluorescence and reduce background. Subsequently, sections were washed again in TBS, and then blocked with Dako antibody diluent solution for 1 h at room temperature. Primary antibodies (LC3 and cathepsin D) were diluted in Dako antibody diluent solution to 1:50 and applied to the sections overnight at 4°C. After the removal of the primary antibody solution, sections were washed with TBS for 3 times and incubated with secondary antibodies (Alexa 546 and Cy5) diluted at 1:500 with Dako antibody diluent solution for 1 h at RT. In the last 10 minutes, DAPI solution was applied for nuclear staining. After that, sections were rewashed 3 times with TBS, dried in an oven at 37°C, and mounted with ProLong™ Gold Antifade Mountant.

Microscopic optical section images were obtained under a 63x/1.4 NA, oil-immersion objective using an Axioplan microscope equipped with an ApoTome module in the regions approximately 500 µm away from the lesion on both sides. The module has a special pseudo-confocal capability to improve image quality. All images were acquired at 0.24 µm intervals over a 2 µm distance using a motorized stage and merged by orthogonal projection to form a single view of the tissue. For each group, from three different animals were evaluated in similar contrast. Since axons in the optic nerve were labeled by the EGFP virus as described above, we typically only analyze the colocalization of LC3 and cathepsin D in labeled axons. Therefore, after converting the

EGFP-image to 8-bit, the axons were highlighted by adjusting the threshold. This image was then inverted and subtracted from the Alexa 546 and Cy5-image using the image calculator. Finally, the resulting image containing only axonal LC3 and cathepsin D was created, and the colocalization of LC3 and cathepsin D was quantified through the JACoP plugin for ImageJ (Bolte und Cordelières 2006).

Furthermore, to explore autophagic induction 6 h after a crush lesion in the optic nerve, a phospho-ATG16L1 antibody was used to label newly forming autophagosomes. Therefore, its level directly reflects autophagy rates and is not affected by the blockade of autophagic flux (Tian et al. 2020). At the same time, SMI-32, a neurofilament protein, was utilized to identify axons in the optic nerve. The staining protocol was the same as mentioned above, except for the following points: first, the cell conditioning solution ((PH = 8.5) was used for antigen retrieval; second, p-ATG16L1 was incubated at 4°C for two overnights; third, SMI-32 was diluted at 1:500 in Dako antibody diluent solution. Sections were photographed with 40x magnification using the ApoTome device (Zeiss).

### **2.2.6 Sodium dodecyl sulfate-polyacrylamide gel electrophoresis (SDS-PAGE)**

Separation of proteins in each sample was achieved using gel electrophoresis according to their different molecular weights. Briefly described, 6 h after the crush injury, rats were euthanized by CO<sub>2</sub> inhalation. Optic nerves were dissected and excised in both proximal and distal regions, spanning a distance of 1 mm from the crush site, with the right side of the optic nerve regarded as an internal control. The samples were then homogenized, sonicated and centrifuged at 1300 rpm and 4°C for 10 minutes in a mixed lysis buffer, including Radioimmunoprecipitation assay buffer (RIPA buffer), protease inhibitor, and phosSTOP-phosphatase inhibitor. Afterward, the supernatant of each sample was carefully collected, and protein concentration was determined using bicinchoninic acid (BCA) assay. Equal amounts of protein (15 µg) from different samples were then diluted in Laemmli buffer containing 20% DTT to a final volume of 12 µl and cooked at 95°C for 5 minutes. Subsequently, the prepared proteins and protein ladders were loaded in different lanes of 4-15% precast gradient gels (BioRad). Electrophoresis was carried out until the dye front almost reached the bottom of the gel.

### **2.2.7 Immunoblotting and quantification**

After electrophoresis, the gels were carefully removed and placed on a PVDF membrane for protein transfer. Before the blot transfer process, the PVDF membrane was treated for 30 seconds in 100% methanol for activation. Then, the sandwich was prepared for



insertion into a blotting cassette filled with ice cold transfer buffer after being covered with two sheets of Whatman filter paper and sponge pads. Protein transfer from the gel to the PVDF membrane was performed at 100V for 2 h in a cooling room. Subsequently, the membrane was blocked with 5% BSA in TBS-T for 1 h at RT. Afterward, the membrane was cut into small pieces based on the molecular weight and incubated with primary antibodies overnight at 4°C. After being rinsed 4 times with TBS-T for 10 minutes each, the membrane was incubated with corresponding HRP-coupled secondary antibodies diluted with 2.5% BSA in TBS-T for 1 h at RT. The optimal concentrations for each antibody were outlined in Table 8. Afterward, the membrane underwent a series of 4 rinses in TBS-T. Before imaging, ECL detection reagents were mixed according to a ratio of 1:1 and evenly applied to the membrane. Then, the membrane was placed in a vilber Lourmat chemiluminescence imaging system controlled by EvolutionCapt Plus 6 software and imaged at different exposure times until optimal bands were obtained. Either Image J or EvolutionCapt Plus 6 software was employed to evaluate the intensities of bands. The final outcomes were standardized relative to glyceraldehyde-3-phosphate dehydrogenase (GAPDH) as loading control.

**Table 8: Antibodies and dilutions involved in Western blotting**

Target protein	Molecular weight [kDa]	Primary antibody	Secondary antibody
LC3 I	16	1:1,000	1:3,000
LC3 II	18	1:1,000	1:3,000
p62	62	1:3,000	1:3,000
Kif5	114	1:1,000	1:3,000
Dynein	74	1:300	1:3,000
P150	150	1:500	1:3,000
Cathepsin D	33	1:300	1:3,000
	46-48		
	52-60		
GAPDH	36	1:10,000	1:5,000

### 2.2.8 Statistical analyses

Statistical analyses were carried out by GraphPad Prism 8 software. Specifically, a two-tailed unpaired t-test was employed to compare two groups, whereas the difference among multiple groups was evaluated through one-way ANOVA or one-way repeated measurement (RM) ANOVA, followed by Turkey's post-hoc tests. If the data did not

conform to a normal distribution, then Mann-Whitney test was applied in measurements of two groups, while comparisons of multiple groups were conducted by Kruskal-Wallis test or Friedman test followed by Dunn's post-hoc tests. Error bars represented means  $\pm$  standard error of the mean (SEM). Significances were determined when  $P < 0.05$ . (\* $P < 0.05$ ; \*\* $P < 0.01$ ; \*\*\* $P < 0.001$ ; \*\*\*\* $P < 0.0001$ ; N.S.: not significant).

### 3 Results

#### 3.1 Experimental set-up for an in vitro model of acute axonal degeneration

To study transport of autophagosomes during acute axonal degeneration in vitro, rat primary cortical neurons in microfluidic chambers were transduced with AAV-mScarlet-LC3 on DIV1. Successful transduction was confirmed through detectable mScarlet fluorescence on DIV10 (Figure 5 B). Under the 40x objective, mScarlet labeled autophagosomes were easily distinguished (Figure 5 C), which allowed for the following analysis. The in vitro acute axonal degeneration model was established using axotomy in the axonal compartment based on the description by Park et al. (Park et al. 2006), as depicted in Figure 5 A. Live microscopy was carried out on the axons before, directly after, and every 2h until 6h after axotomy within the region extending up to 250  $\mu\text{m}$  proximal to the site of the lesion.

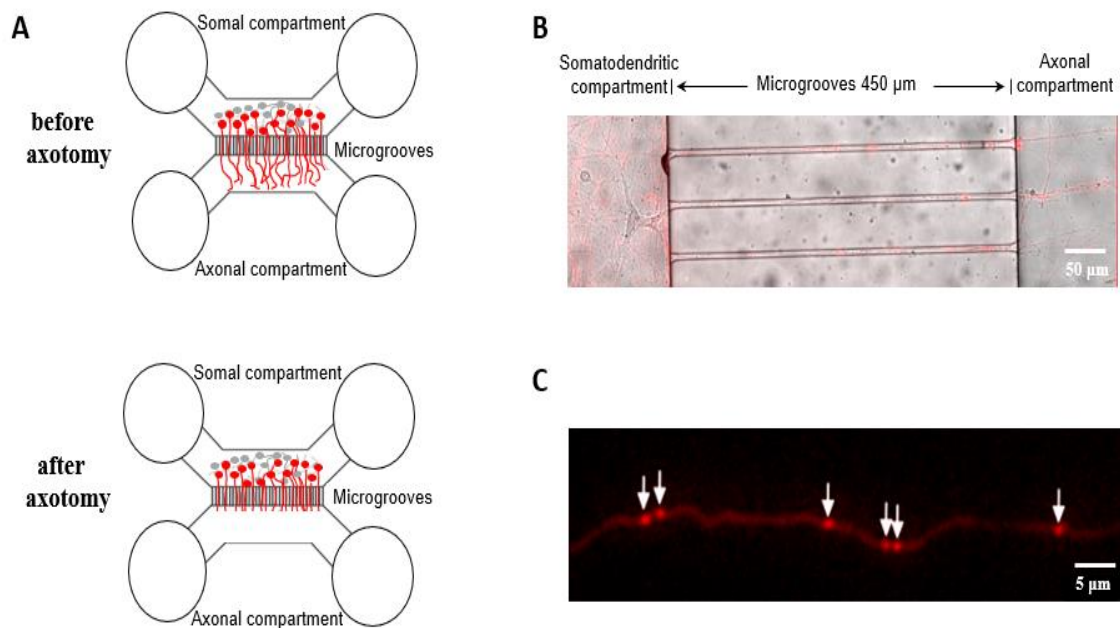


**Figure 5: Acute axonal degeneration model in vitro.** On DIV 1, AAV-mScarlet-LC3 was introduced into the cortical neurons of rats, which were subsequently imaged on DIV 10. **(A)** Schematic drawing of the experimental set-up in microfluidic chambers. Each microfluidic chamber comprises 4 wells and two compartments connected by 450  $\mu\text{m}$  long microgrooves. The soma compartment serves as the locus for seeding primary cortical neurons. Only axons have the ability to traverse the microgrooves and reach the opposite side, named the axonal compartment. Axotomy is performed only in the axonal compartment to induce acute axonal degeneration. **(B)** Exemplary image of rat cortical neurons transduced with specified LC3 AAV vectors in the microfluidic chamber on DIV 10. Scale bar: 50  $\mu\text{m}$ . **(C)** Representative clearly labeled autophagosomes on the axon transduced with the given LC3 AAV vector on DIV 10. Scale bar: 5  $\mu\text{m}$ .

### 3.2 Evaluation of axonal transport of autophagosomes after axotomy in vitro

Having achieved effective transduction with AAV-mScarlet-LC3, the next step was to explore if transport of autophagic vesicles changes during axonal degeneration using the in vitro model established above. Since mounting evidence indicates that axonal transport is altered prior to the death of neuronal cells (Wang et al. 2018), it has not yet been addressed to compare the axonal transport of autophagosomes before and at different time intervals post-injury (Figure 6).

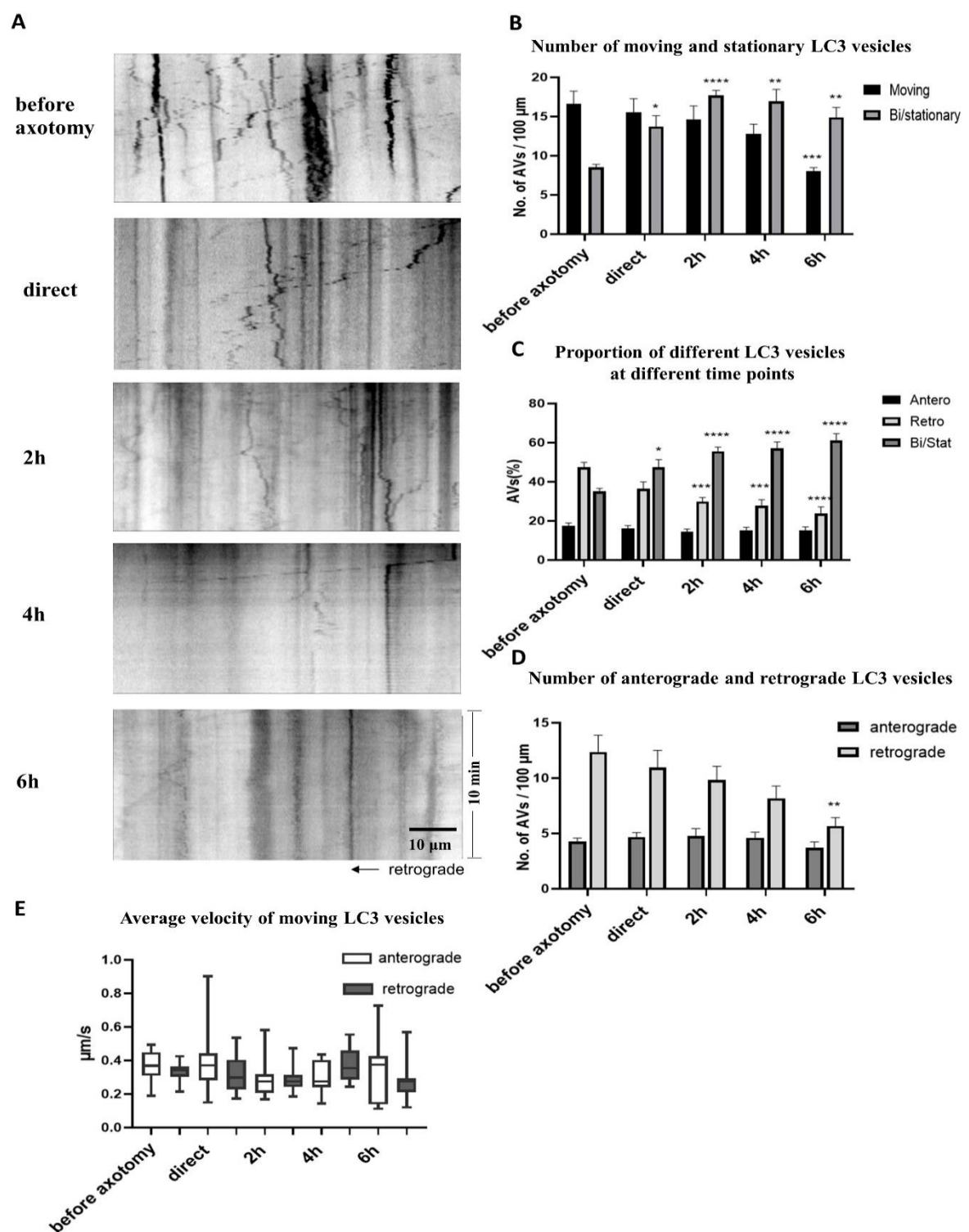


**Figure 6: Live imaging of autophagosomes in rat primary cortical neurons after axotomy in vitro on DIV 10. (A)** Exemplary kymographs of autophagosomes along the axons before and at various time intervals following axotomy within 10 minutes (y-axis). **(B, C, D)** Quantification of autophagosome movements before and after axotomy. **(D)** Quantification of the average velocity of autophagosomes before and after axotomy. In all quantifications, At least 27 axons in the regions with a distance of 250  $\mu\text{m}$  proximal to the lesion site were included. \* $P < 0.05$ ; \*\* $P < 0.01$ ; \*\*\*\* $P < 0.0001$  by one-way ANOVA and Turkey's multiple comparisons test or Kruskal-Wallis test and Dunn's multiple comparisons test based on normality tests.

Prior to analysis, autophagosomes were classified into two main categories: moving and stationary vesicles (the latter class including bidirectional moving vesicles), based on whether their net movement was greater than 5  $\mu\text{m}$  within the 3-minute imaging window (net velocity  $> 0.028 \mu\text{m/s}$ ).

After axotomy, the bidirectional and stationary autophagosomes immediately increased to  $13.7 \pm 1.4$  per 100  $\mu\text{m}$  and reached the peak at  $17.7 \pm 0.6$  per 100  $\mu\text{m}$  2h after axotomy compared to  $8.5 \pm 0.4$  per 100  $\mu\text{m}$  before axotomy. In addition, their numbers never returned to normal values even 6h after axotomy ( $14.9 \pm 1.3$  per 100  $\mu\text{m}$ ). On the contrary, a significant reduction in the number of motile autophagosomes was found, from  $16.7 \pm 1.6$  per 100  $\mu\text{m}$  before axotomy to  $8.0 \pm 0.4$  per 100  $\mu\text{m}$  6h after axotomy (Figure 6 B). Similar to the number of bidirectional and stationary autophagosomes, the percentage of bidirectional and stationary autophagosomes also increased significantly after axotomy ( $47.5 \pm 3.9\%$ ) and maintained an upward trend until 6h after axotomy (2h after:  $55.6 \pm 2.1\%$ ; 4h after:  $57.0 \pm 3.3\%$ ; 6h after:  $61.1 \pm 3.6\%$ ) compared to before axotomy ( $35.0 \pm 1.6\%$ ). As for the proportion of motile vesicles, there was no statistical significance in anterograde transport, while the percentage of vesicles moving retrogradely significantly decreased at 2h after axotomy ( $29.8 \pm 2.0\%$ ) compared to before axotomy ( $47.4 \pm 2.5\%$ ) and persisted until 6h after axotomy ( $23.8 \pm 3.4\%$ ) (Figure 6 C). These findings were further confirmed by the absolute number of moving autophagosomes. Only the retrogradely transported vesicles were significantly reduced at 6h after axotomy ( $5.7 \pm 0.8$  per 100  $\mu\text{m}$ ) in comparison with the data before axotomy ( $12.4 \pm 1.5$  per 100  $\mu\text{m}$ ) (Figure 6 D). However, the speed of motile autophagosomes was not notably affected at all observed time points (Figure 6 E). Overall, axotomy significantly impaired autophagosome transport, as evidenced by restricted retrograde motility and the rapid elevation of stationary vesicles. This may be due to the fact that after axotomy, the substances required for anterograde transport can still be replenished from the cell body in a short period, whereas retrograde transport originating from axon terminals is more vulnerable to disruption.

### 3.3 Establishment of in vivo models of axonal degeneration in the optic nerve

To better understand how autophagy contributes to axonal degeneration in vivo and to see if in vitro parameters are consistent with the in vivo situation, we developed three in vivo axonal degeneration models and performed live microscopy in the optic nerve at different time points: 1) crush lesion model in young adult rats (3 months); 2) subacute glaucoma model in young adult rats (3 months); 3) aging in old rats (18 months).

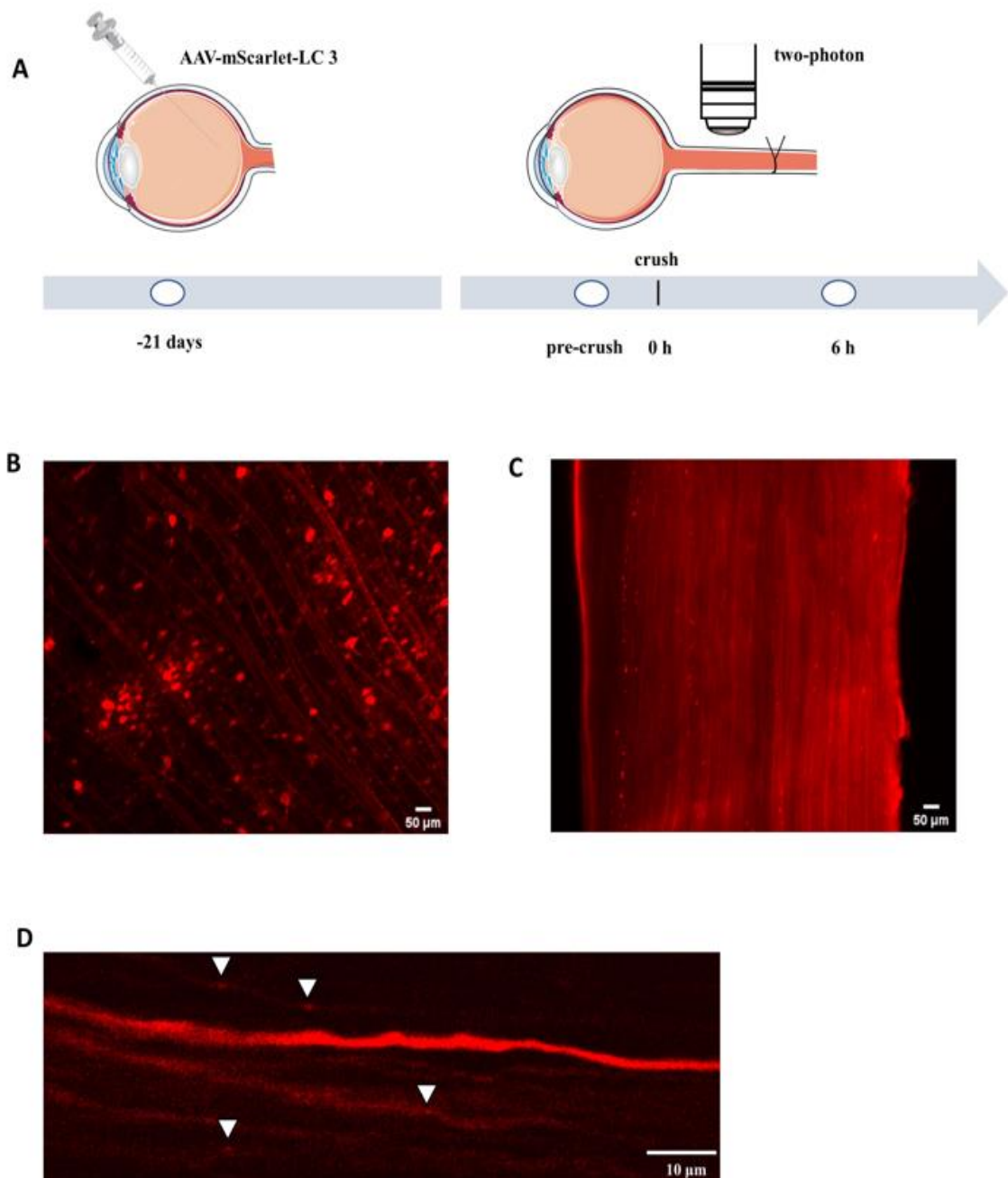


**Figure 7: Live imaging of autophagosomes in vivo.** (A) Schematic diagram of the experimental setup of crush lesion on the optic nerve. The viral vector was intravitreally injected 3 weeks before optic nerve surgery. In this model, a suture approximately 1mm away from the eye bulb was closed for 30 seconds to create a completely axotomy on the optic nerve. Then the autophagosome transport was evaluated before and over 6h after crush at 500  $\mu\text{m}$  proximal to the lesion site. (B) 10x magnification flat mounting section of the retina 3 weeks after AAV injection. (C) Longitudinal section of the optic nerve 3 weeks after AAV injection under 10x magnification. (D) Representative two-photon microscopy of the optic nerve. White arrows indicated the LC3 viral vector labeled autophagosomes in the single axon. Figure A adjusted from Smart-servier medical ART, <https://smart.servier.com/>.

In all in vivo models, rats were intravitreally injected with AAV-mScarlet-LC3 at 21 days prior to optic nerve exposure surgery (Figure 7 A). This allowed for sufficient labeling of axons in the retina (Figure 7 B) and optic nerve (Figure 7 C), a prerequisite for the following live imaging. After optic nerve exposure according to a previous protocol in our research group (Koch et al. 2011), superficially labeled axons were imaged under a two-photon microscope while animals were under deep anesthesia. In order to reduce the disruption of animal's breathing and stabilize live imaging, each picture was captured in synchronization with the respiratory cycle detected by an accelerometer on the chest. This set-up allowed to clearly visualize the movements of autophagosomes in the optic nerve (Figure 7 D).

### 3.3.1 Autophagosome trafficking in young animals at basal levels

After the successful establishment of the above model, the movement pattern of autophagosomes in the optic nerve was investigated under the basal state. In young adult rats (age: 3 months), the number of moving LC3 vesicles was  $10.81 \pm 3.03$  per minute per mm, while the number of stationary LC3 vesicles was considerably higher at  $53.12 \pm 7.03$  per mm. Among all moving LC3 vesicles, 85.21% were retrogradely transported, occupying the dominant position in the transport process. The average velocity of retrograde transport was  $461.3 \pm 60.02$  nm/s, which was also faster than the average velocity of the antegrade transport with  $316.4 \pm 81.12$  nm/s.

### 3.3.2 Evaluation of autophagosome transport in aging

Aging is a major risk factor in the majority of neurodegenerative diseases. Since neurons are highly polarized cells whose elongated axons are usually located far away from the cell body, axonal transport is essential for maintaining homeostasis and biological functionality. However, aging may challenge this process and potentially increase susceptibility to neurodegenerative diseases, as adult neurons in the central nervous system are post-mitotic and lose their regenerative function.

For the purpose of investigating the effects of aging on autophagosome transport in the rat optic nerve, live imaging was performed in two groups of different ages: a 3-month-old young group and an 18-month-old old group. The transport properties of autophagosomes varied significantly in different age groups. Compared to  $10.81 \pm 3.03$  per minute per mm in the young group, the number of motile LC3 vesicles significantly decreased to  $4.20 \pm 1.04$  per minute per mm in the old group (Figure 8 B). Interestingly, we only observed a significant reduction with age in the retrograde moving LC3 vesicles ( $8.97 \pm 2.14$  per minute per mm in the young group and  $2.78 \pm 0.69$  per minute per mm in the old group), whereas the number of anterograde LC3 vesicles was relatively stable (Figure 8 D). Correspondingly, the percentage of different LC3 vesicles showed the same results (Figure 8 E). However, the number of stationary LC3 vesicles was significantly elevated with age, reaching  $92.34 \pm 3.83$  per mm, compared with  $53.12 \pm 7.03$  per mm in the young group (Figure 8 C). In terms of motility, only the average velocity of retrograde transport was severely impaired in aged animals at  $184.0 \pm 28.19$  nm/s compared to  $461.3 \pm 60.02$  nm/s in young animals (Figure 8 F).

Taken together, autophagosome transport in the optic nerve of aged animals is characterized by strongly impaired motility of retrograde transport and an increased stationary fraction.

### 3.3.3 Transport of autophagosomes in the crush lesion model

#### 3.3.3.1 Assessment of autophagosome trafficking in the crush lesion model

Having conducted all previous experiments under resting conditions, we wondered whether axonal transport of autophagosomes would be affected in pathological circumstances. Therefore, we performed crush lesion to the optic nerve and analyzed autophagosome trafficking before and thereafter up to 6h after lesion. Optic nerve crush (ONC) serves as an excellent model for studying traumatic optic neuropathy since it results in axonal degeneration and retinal ganglion cell death (Figure 9).

In vivo, before crush, the number of moving LC3 vesicles was  $14.46 \pm 4.09$  per minute per mm, whereas the number of stationary ones was considerably higher than that of moving vesicles at  $48.95 \pm 10.64$  per mm (Figure 9 C and D). However, a majority of motile LC3 vesicles lost their motor function after crush lesion. Even directly after crush, the number of motile LC3 vesicles decreased immediately to  $7.21 \pm 0.88$  per minute per mm, and the situation became worse at 6h after crush injury, with a value of  $0.69 \pm 0.44$  per minute per mm (Figure 9 C). In contrast, the number of stationary vesicles significantly increased



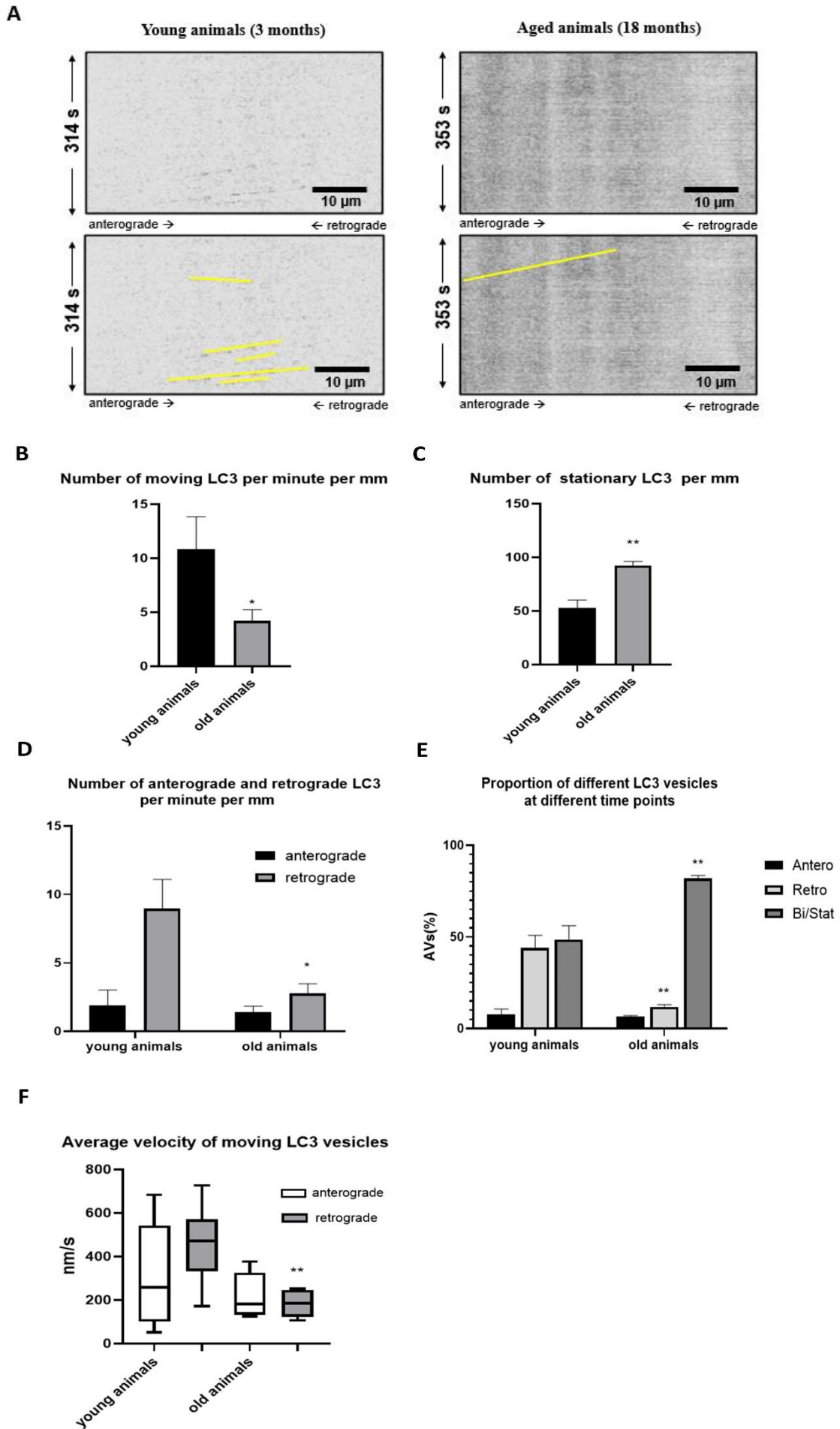


**Figure 8: In vivo autophagosome transport of the optic nerve in young adult rats (3 months) and aged rats (18 months).** (A) Representative kymographs and movement trajectories of LC3 transport in the optic nerve of young and aged rats. (B, C, D) Quantification of the number of motile and stationary LC3 vesicles in the optic nerve of rats with different ages. (E) Quantification of proportions of different LC3 vesicles at different ages. (F) Quantification of the average velocity of motile LC3 vesicles at different ages. In all quantifications, a minimum of 10 axons per time point per animal was evaluated at approximately 500  $\mu\text{m}$  proximal to the lesion site. A total of 5 animals were included. \* $P < 0.05$ ; \*\* $P < 0.01$  by unpaired t test or Mann-Whitney test based on the normality test of variables.

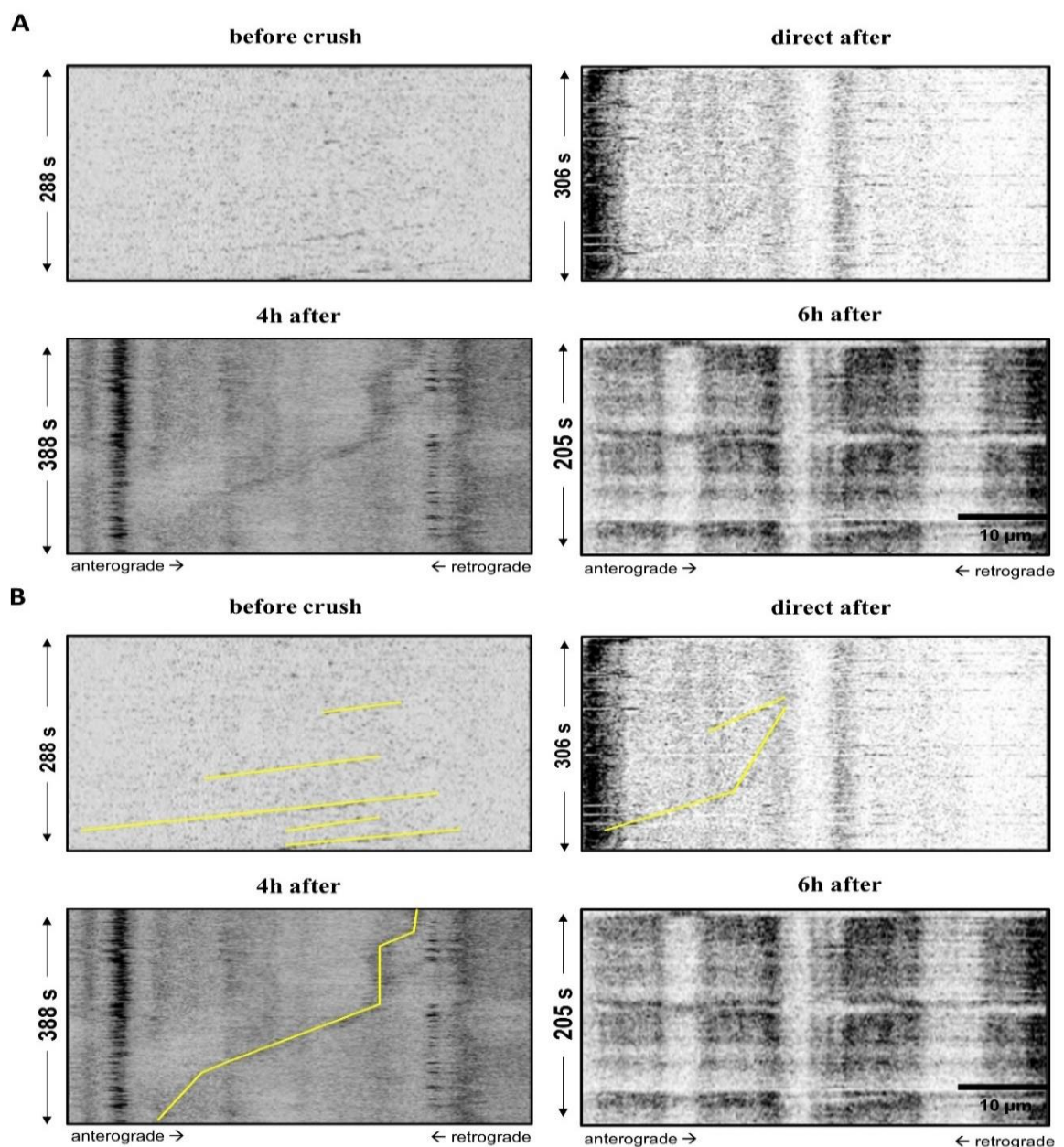
to  $133.37 \pm 8.54$  per mm direct after crush lesion compared to before crush and continued to rise until reaching a peak of  $183.25 \pm 16.04$  per mm at 6h after lesion (Figure 9 D). However, only retrogradely moving LC3 vesicles of all motile autophagosomes were affected by the crush injury. The number of anterograde LC3 vesicles was relatively stable within 4 hours after crush injury (direct after:  $3.76 \pm 0.98$  per minute per mm; 2h after:  $2.88 \pm 0.71$  per minute per mm; 4h after:  $3.39 \pm 0.78$  per minute per mm) compared with that before crush ( $2.39 \pm 1.82$  per minute per mm). Although this number dropped to  $0.64 \pm 0.39$  per minute per mm at 6h after crush, there was no statistical significance (Figure 9 E). As opposed to that, the number of retrograde LC3 vesicles decreased rapidly after crush injury, with a significant difference occurring as early as 2h after crush ( $3.60 \pm 0.66$  per minute per mm) compared to  $12.15 \pm 2.40$  per minute per mm before crush (Figure 9 E). These findings were quite consistent with the proportions of different LC3 vesicles at the given time points (Figure 9 G). In terms of moving speed, before crush, the average velocity of anterograde transport was  $359.7 \pm 130.6$  nm/s, while the velocity of retrograde transport was even faster at  $540.41 \pm 52.95$  nm/s. However, the average velocity of retrograde transport was significantly reduced at 6h after crush lesion, but the velocity of anterograde transport had no difference at all time points (Figure 9 F).

Both in vivo and in vitro, motile LC3 vesicles accounted for more than 60% of all autophagosomes at the basal condition. However, there was a difference between anterograde and retrograde transport. In vitro, only 73% of motile vesicles moved retrogradely, while this number increased to 85% in vivo. The velocity of retrograde transport was also faster in vivo with an average speed of  $540.41 \pm 52.95$  nm/s compared to the in vitro situation with an average speed of  $333.07 \pm 15.09$  nm/s, although there was no difference in anterograde transport (Figure 9 F). Of all motile autophagosomes observed in vivo and in vitro after traumatic axonal damage, only the number of retrograde LC3 vesicles decreased significantly. However, the number of retrogradely moving LC3 vesicles decreased more rapidly in vivo, with a remarkable

decline at 2h after crush injury, whereas statistical significance was observed only 6 h after axotomy in vitro (Figure 9 E). The motility also behaved in a different way between in vitro and in vivo experiments. Unlike in vivo, the average velocity in both directions did not change significantly at all observed time points in vitro.

### 3.3.3.2 Colocalization of LC3 and active Cath D after axotomy in vitro

Having elucidated the autophagosome transport patterns in different axonal degeneration models, we next wondered if the fusion of autophagosomes with lysosomes and their degradative capacity were affected by axonal degeneration, explaining their accumulation and retrograde transport deficit.



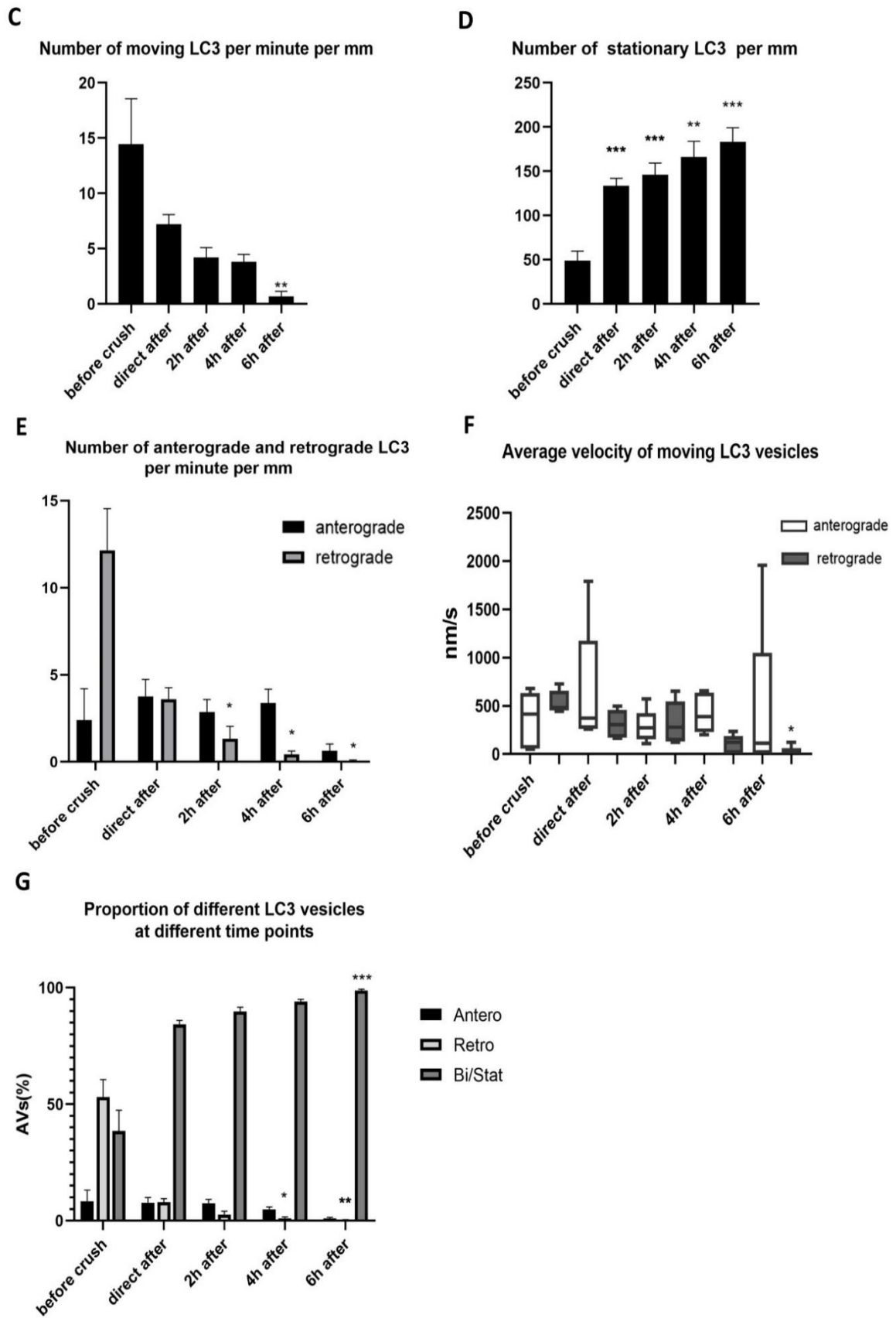


**Figure 9: In vivo autophagosome transport in the optic nerve of rats after crush lesion.** (A, B) Representative kymographs and moving trajectories of LC3 transport in the rat optic nerve before and at the observed time points post-crush lesion. (C, D, E) Quantification of the number of motile and stationary LC3 vesicles in the optic nerve of rats before and at the given time points following crush lesion. (F) Quantification of the average velocity of different moving LC3 vesicles before and at the given time intervals following crush lesion. (G) Quantification of proportions of different LC3 vesicles before and at the given time points after crush lesion. In all quantifications, a minimum of 10 axons per time point per animal was evaluated at a distance of roughly 500  $\mu\text{m}$  proximal to the location of the lesion. A total of 5 animals were included. \* $P < 0.05$ ; \*\* $P < 0.01$ ; \*\*\* $P < 0.001$  by one-way repeated measures ANOVA and Turkey's multiple comparisons test or Friedman test and Dunn's multiple comparisons test on the basis of normality tests of variables.

BODIPY–pepstatin A is a useful probe with green fluorescence that binds specifically to active cathepsin D, an aspartyl protease, in acidified environments at the pH of 4.5. In living cells, BODIPY–pepstatin A is taken up by endocytosis and subsequently transported to lysosomes. As cathepsin D is ubiquitously distributed in lysosomes and plays pivotal roles in intracellular protein degradation, we therefore used BODIPY–pepstatin A to visualize lysosomes and further reflect whether autolysosomes following the fusion of autophagosomes and lysosomes represent acidified structures containing activated hydrolases, such as cathepsin D.

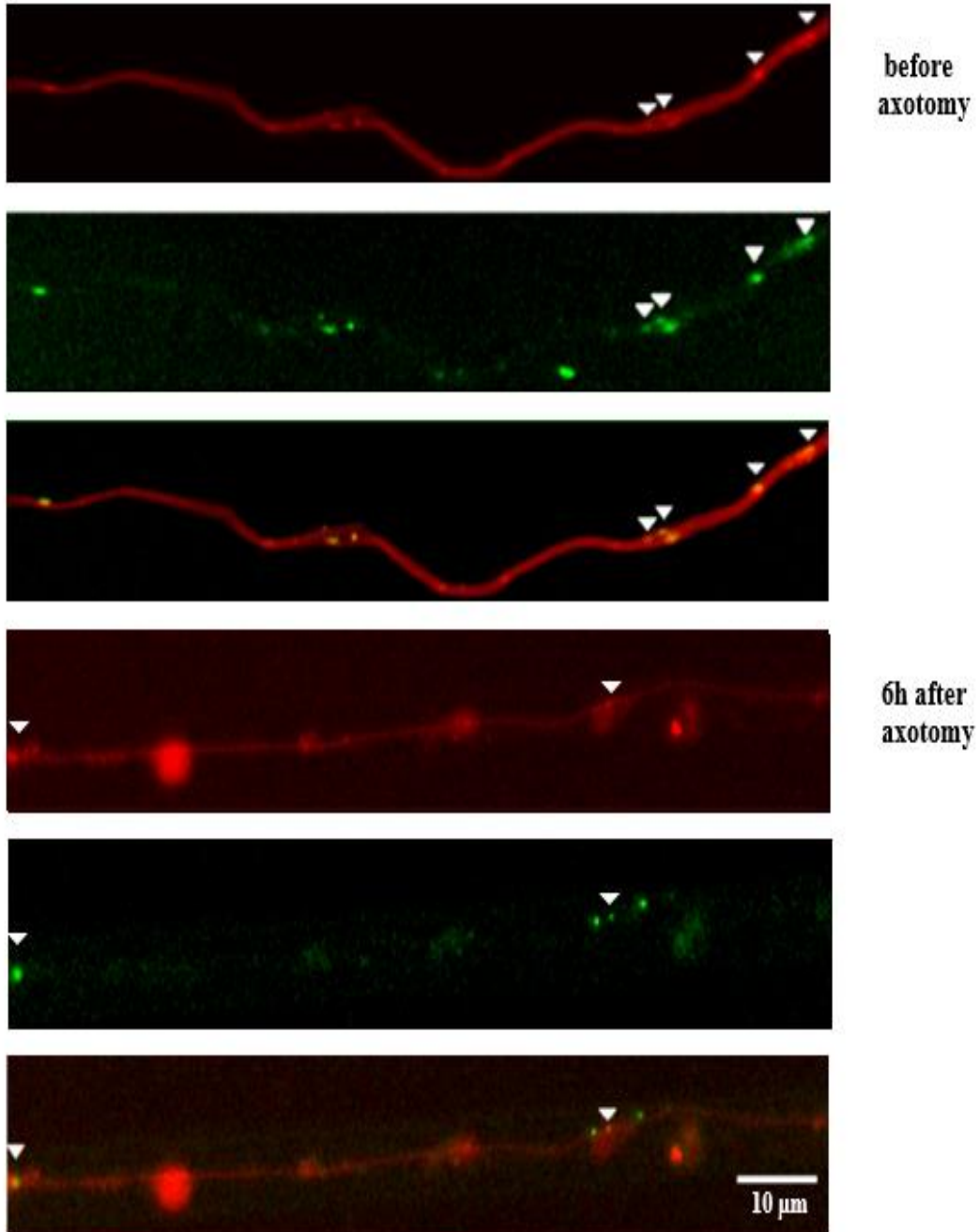
Primary cortical neurons co-cultured with astrocytes were transduced with the same mScarlet-LC3 viral vector on DIV 1 in microfluidic chambers. On DIV 11, axons were long enough to grow across microgrooves and enter the axonal compartment. At that time-point, neurons were treated with 1  $\mu\text{M}$  BODIPY–pepstatin A both in somatic and axonal compartments for 1h. After replacing the medium in the chambers, live imaging was conducted before and every 2 up to 6 hours after axotomy to explore the colocalization of mScarlet-LC3 and BODIPY-pepstatin A on the axonal side. The ratio of colocalization was assessed by manually counting particles in axons within approximately 250  $\mu\text{m}$  from the axon terminal.

We found the ratio of LC3 colocalized with active cathepsin D, an indicator of lysosome-autophagosome fusion, was relatively low at the basal condition. Only  $29 \pm 1.86\%$  of viral labelled LC3 vesicles contained active cathepsin D (Figure 10 D). However, a large proportion ( $59.48 \pm 2.81\%$ ) of active cathepsin D labeled vesicles were positive for LC3 (Figure 10 E). After axotomy, these two numbers gradually dropped and reached their lowest point at 6h after axotomy ( $14.44 \pm 2.43\%$  of labeled LC3 vesicles colocalized with active cathepsin D and  $25.96 \pm 3.97\%$  of active cathepsin D vesicles still positive for LC3, respectively) (Figure 10 D and E). This indicated that axotomy has an adverse impact on the fusion of autophagosomes and lysosomes containing mature hydrolases. Besides, we also observed a notable decline both in the number of labeled LC3 vesicles from

$0.15 \pm 0.008$  per  $\mu\text{m}$  before axotomy to  $0.1 \pm 0.008$  per  $\mu\text{m}$  6h after axotomy and the number of active cathepsin D from  $0.07 \pm 0.005$  per  $\mu\text{m}$  before axotomy to  $0.05 \pm 0.004$  per  $\mu\text{m}$  6h after axotomy (Figure 10 B and C).

**A**

**Cortical neurons cultured in microfluidic chamber**  
**Axonal compartment mScarlet-LC3 BODIPY-pepstatin A**



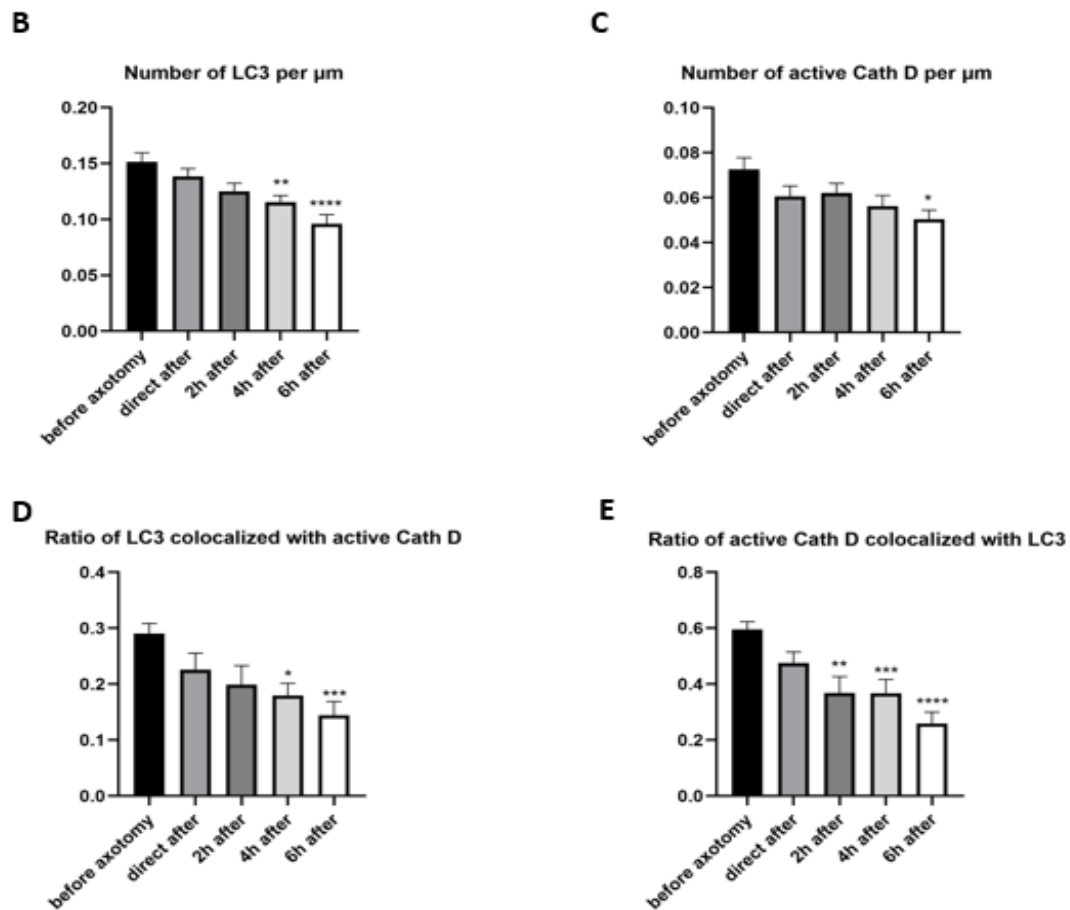


**Figure 10: Decreased colocalization of LC3 and active Cath D after axotomy in vitro.** (A) Representative images illustrating LC3 partial colocalization with active cathepsin D marked by BODIPY–pepstatin A in the axons of cortical neurons before and 6h after axotomy. Arrows indicate LC3-positive vesicles with detectable BODIPY–pepstatin A. (B, C) Quantification of the number of LC3 and active cathepsin D vesicles per  $\mu\text{m}$  in cortical neuronal axons at the given time points. (D) Quantitative analysis of LC3 labeled vesicles positive for active cathepsin D at the observed time points. (E) Quantitative analysis of BODIPY–pepstatin A positive vesicles colocalized with LC3 labeled by the given viral vector at the indicated time points. Data was quantified from at least 23 neuronal axons at each time point in three independent experiments. \* $P < 0.05$ ; \*\* $P < 0.01$ ; \*\*\* $P < 0.001$ ; \*\*\*\* $P < 0.0001$  by one-way ANOVA and Turkey’s multiple comparisons test or Kruskal-Wallis test and Dunn’s multiple comparisons test in accordance with normality tests of variables.

### 3.3.3.3 Colocalization of LC3 and active Cath D after axotomy in vivo

To further investigate the fusion of autophagosomes and lysosomes following acute axonal degeneration in vivo, we quantified the colocalization of axonal LC3 and cathepsin D in the optic nerve at a distance of approximately  $500 \mu\text{m}$  from the lesion site in both directions using Pearson’s correlation coefficient (Figure 11 A and B). Analysis revealed very little colocalization of LC3 and cathepsin D ( $0.07 \pm 0.007$ ) in the contralateral unlesioned control. At 6h after crush injury, the colocalization increased significantly in the distal parts of the optic nerve, although its value was still relatively low at  $0.14 \pm 0.013$ . However, no big difference was noticed between the proximal stumps and unlesioned control.



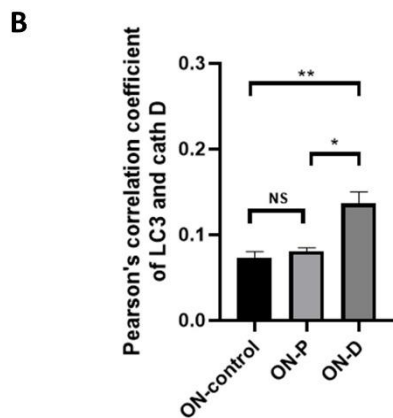
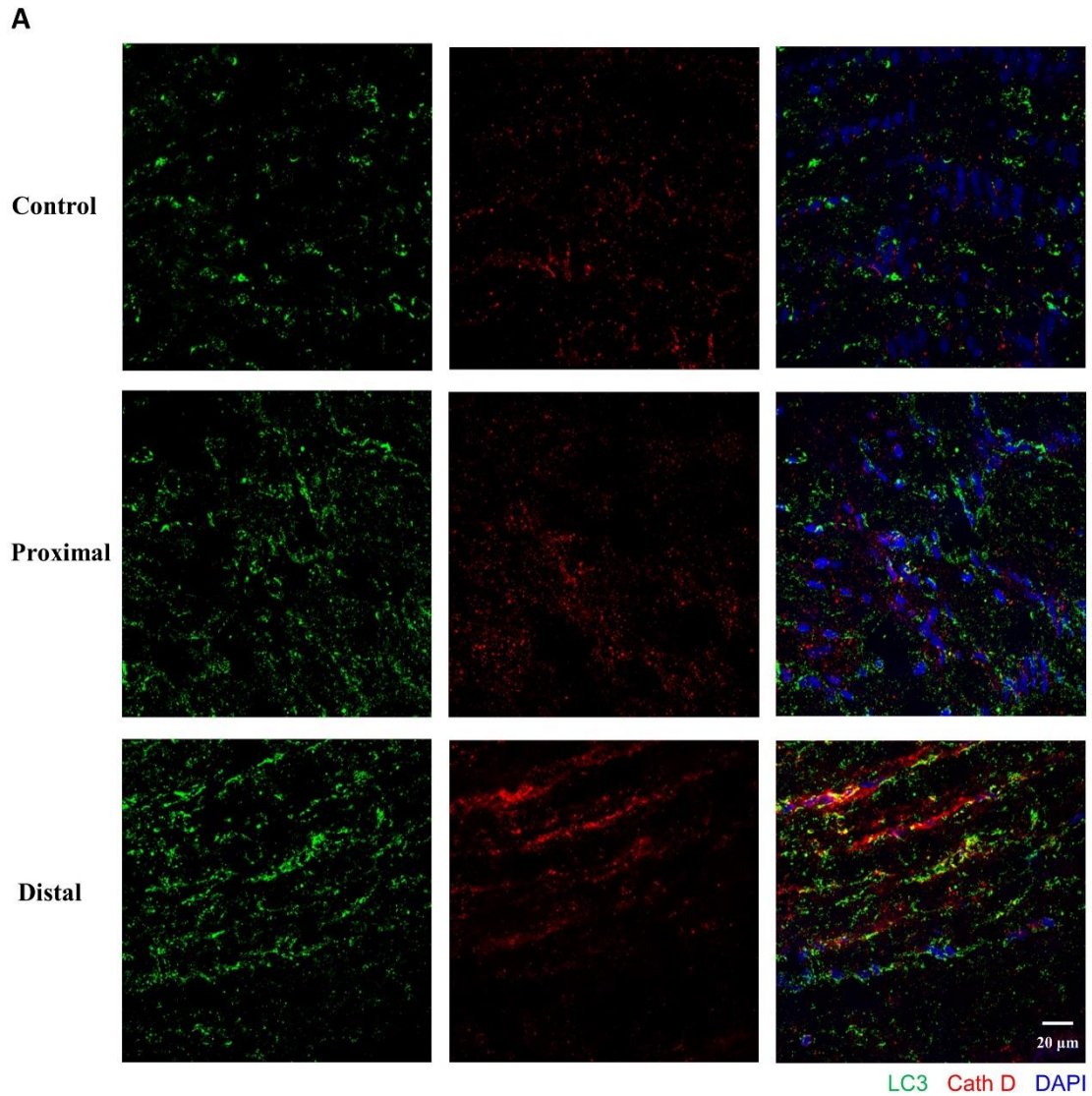


**Figure 11: Colocalization of LC3 and cathepsin D in the rat optic nerve 6 hours after crush lesion.**

(A) Representative immunofluorescence staining of LC3 and cathepsin D at 6h post-injury in the different regions of the optic nerve located approximately 500 µm away from the injury site compared with the contralateral side. (B) Quantification of the colocalization of LC3 and cathepsin D in the given regions of the optic nerve. Data from 3 animals were quantified and each group consisted of 15 images. \* $P < 0.05$ ; \*\* $P < 0.01$  N.S. no significant difference, determined by one-way ANOVA and Turkey's multiple comparisons tests.



### 3.3.3.4 Activation of autophagy after optic nerve crush injury in rats

During the process of autophagy, the conversion of LC3-I to LC3-II requires the involvement of an LC3 conjugation system comprising ATG16L1/ATG5-12, whereby phosphatidylethanolamine is incorporated into LC3-I. Thus, the ATG16L1-containing complex is indispensable to autophagy. Besides, it has been recently demonstrated that the level of phosphorylated ATG16L1 (p-ATG16L1) is directly associated with the autophagy rate (Robichaud et al. 2022; Tian et al. 2020). Here, we examined the

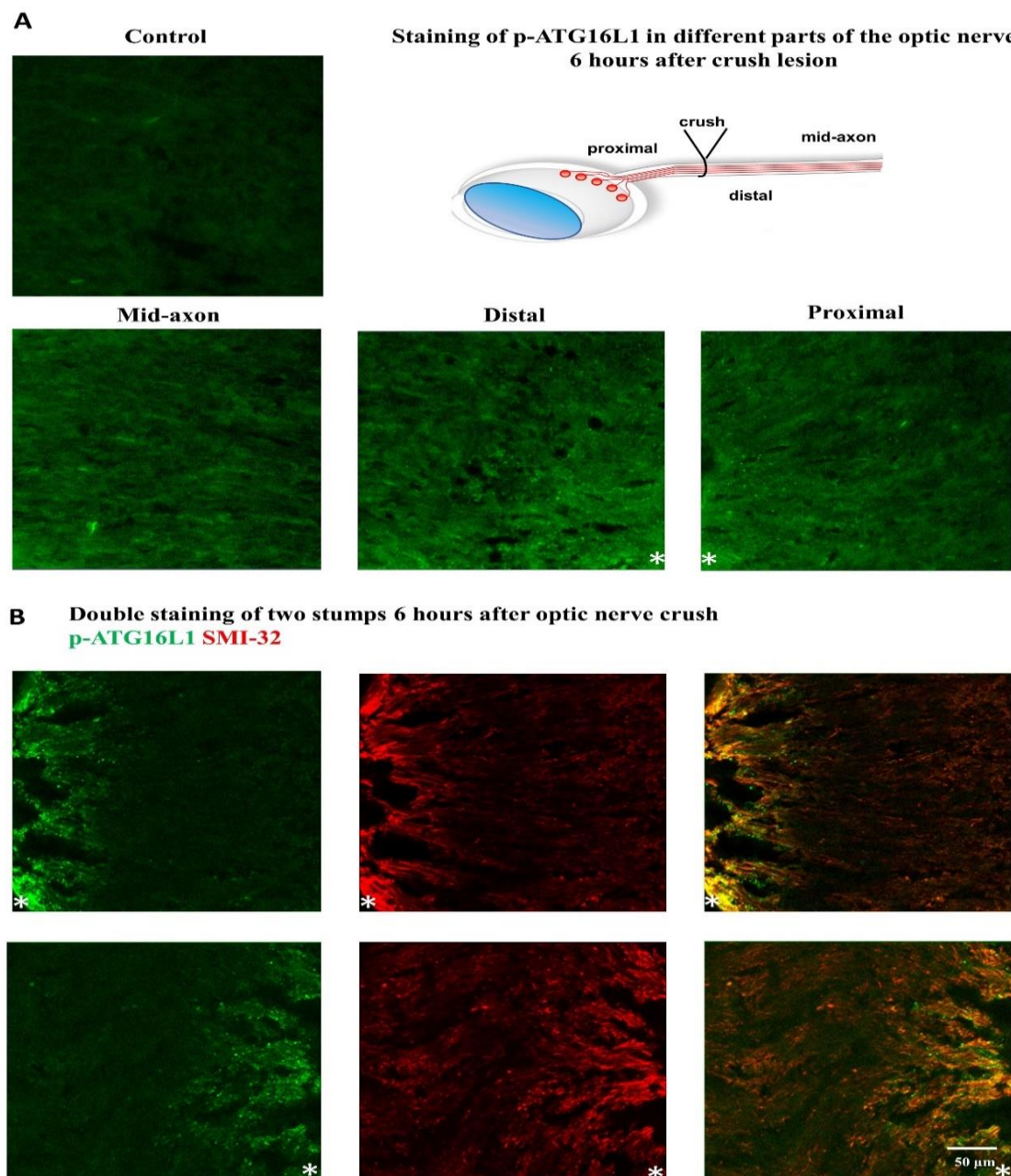


**Figure 12: Crushed-induced autophagy in rat optic nerve.** (A) Representative immunofluorescence staining for p-ATG16L1 in the contralateral unlesioned control and different parts of the optic nerve 6 hours after crush injury. (B) Representative double immunofluorescence staining of p-ATG16L1 (green) and SMI-32 (red) at the proximal and distal stumps in the optic nerve 6h post-injury. Asterisks indicate the lesion site.

expression of p-ATG16L1 to figure out if autophagy is activated by the optic nerve crush. At 6h following the crush injury, a considerable number of p-ATG16L1 positive puncta were observed at both terminals of the optic nerve, whereas there was little expression in the untreated contralateral control or intermediate optic nerve away from the crush site (Figure 12 A). Further double fluorescence staining revealed that a considerable portion of the p-ATG16L1 positive puncta overlapped with SMI-32, indicating that autophagy was induced within axons (Figure 12 B).

### 3.3.3.5 Crush lesion alters autophagic flux and the motor protein distribution in the rat optic nerve

Our previous *in vivo* live imaging demonstrated that the motility of autophagosomes was impaired in the optic nerve of rats following lesion-induced axonal degeneration. Besides, autophagy was also induced during this process. The next step was to further analyze these findings at the protein level and investigate the underlying mechanisms.

Optic nerve protein lysates were obtained 6h after the crush lesion from both terminals within 1 mm of the injury site. Compared with the untreated contralateral control, a significant increase in the LC3 II/I ratio was observed on both sides of the optic nerve following the crush lesion (Figure 13 B). In addition, p62 levels also had a dramatic elevation at both stumps 6h after crush lesion (Figure 13 C).

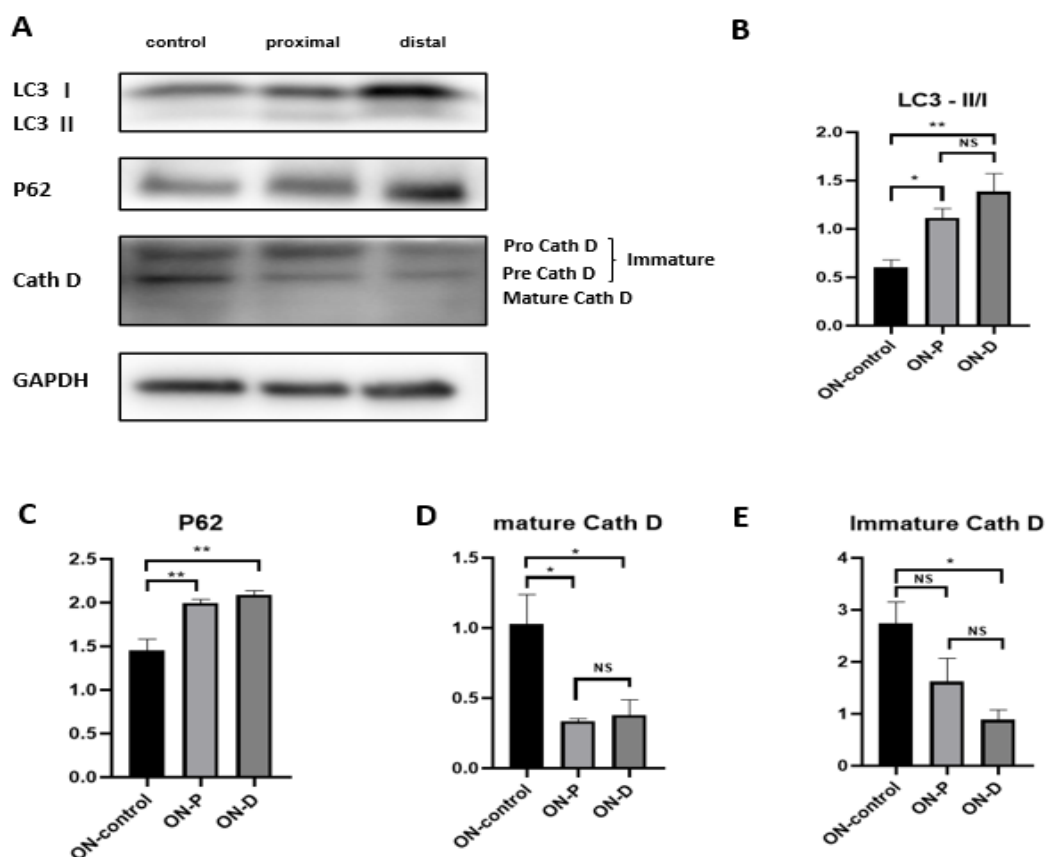


**Figure 13: Changes of autophagic pathways in the rat optic nerve 6 hours after crush lesion.** (A) Representative immunoblots of LC3 II/I, p62, cathepsin D, and GAPDH at two stumps of the optic nerve 6h after crush injury compared with the contralateral side. (B-E) Quantifications of the band intensities of LC3 II/I, p62, and Cathepsin D normalized to GAPDH as loading control. Blots were quantified from at least 3 animals. \*P < 0.05; \*\*P < 0.01 N.S. no significant difference, determined by one-way ANOVA and Turkey's multiple comparisons test.

In addition, we also explored changes in proteolytic capacity, as this is a crucial component of the autophagy-lysosome process and plays a vital role in maintaining neuronal cell homeostasis (Vidoni et al. 2016). Here, the protein level of different isoforms of cathepsin D, an essential aspartyl protease that predominantly locates in lysosomes, was evaluated. Cathepsin D is specifically directed to cellular vesicular structures and undergoes a gradual maturation process facilitated by an acidic environment, thereby enabling the successful degradation of proteins (Benes et al. 2008). In the blots, crush lesion in the optic nerve caused a significant reduction in the level of mature cathepsin D within the proximal and distal segments compared with the contralateral side. However, the protein levels were not different between the proximal and distal sides. (Figure 13 D). Besides, the immature cathepsin D level, including pro- and pre- isoforms, was also significantly decreased but only on the distal sides of the crush compared with the contralateral side (Figure 13 E). Altogether, cathepsin D levels were remarkably reduced 6h after optic nerve crush, indicating impaired autophagic degradation.

We further investigated the levels of motor proteins, which are important components for cellular transport, such as autophagosomes. Kinesin-1 is a major motor protein required for anterograde autophagosome transport, whereas the dynein- dynactin complex is in charge of retrograde trafficking of autophagosomes (Fu and Holzbaur 2014). At 6h after crush injury, we found a significant increase of Kif 5, a member of the kinesin 1 family, in the proximal parts of the optic nerve, compared with the distal parts and the contralateral unlesioned side (Figure 14 B). As the lesion could interrupt the regular transport of the optic nerve, it is conceivable that Kif 5 was accumulated from the cell body to the proximal terminal but spread out from the distal sides of the optic nerve. Interestingly, no alterations in dynein protein levels were detected, but its adaptor p150Glued, the biggest component of the dynactin complex, was dramatically reduced after crush injury both on the proximal and distal sides (Figure 14 C and D). Although the p150Glued level at the distal stump was not statistically different from that in the contralateral unlesioned control, the value was at the statistical threshold (P = 0.0526) (Figure 14 D). Taken together, these findings indicated that crush-induced axonal

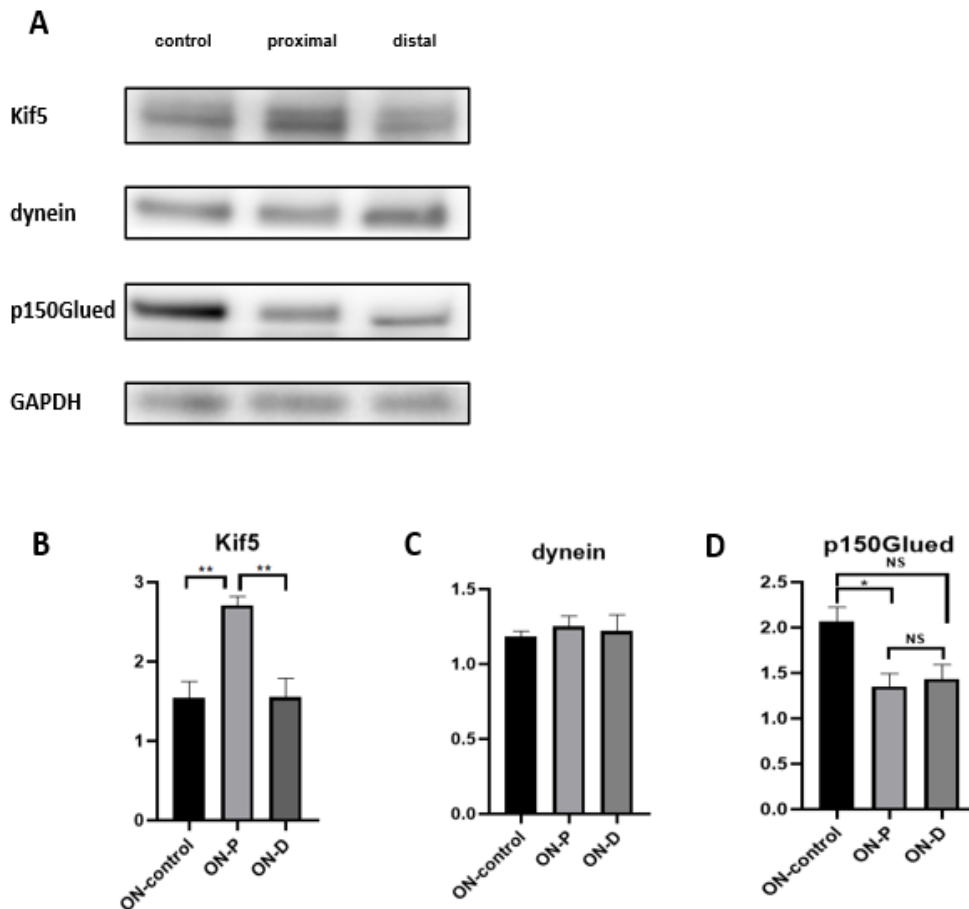


**Figure 14: Motor protein levels in the rat optic nerve 6 hours after crush lesion.** (A) Representative immunoblots of kif5, dynein, p150Glued and GAPDH at two stumps of the optic nerve 6h after crush injury compared with the contralateral side. (B-D) Quantifications of the band intensities of kif5, dynein and p150Glued normalized to GAPDH as loading control. Blots were quantified from at least 3 animals. \*P < 0.05; \*\*P < 0.01 N.S. no significant difference, determined by one-way ANOVA and Turkey's multiple comparisons.

degeneration in the optic nerve altered the distribution patterns of motor proteins in vivo, leading to the accumulation of Kif5 in the proximal parts of the optic nerve and a marked reduction in p150Glued at both stumps.

### 3.3.4 Analysis of autophagosome transport in a subacute glaucoma model

#### 3.3.4.1 Establishment of a subacute glaucoma model based on limbal vascular plexus cauterization

Since the previous experiments had been performed under acute axonal degeneration, we wondered if the results were also applicable to other models of neurodegeneration, and thus a subacute model of glaucoma was chosen. In this model, the method of inducing unilateral ocular hypertension (OHT) was developed through low-temperature

cauterization of the vascular plexus surrounding the corneal limbus, an integral component of the drainage pathway for aqueous humor (Lani et al. 2019). After cautery, intraocular pressure (IOP) remained at a high level for the first few days and then gradually decreased due to corneal revascularization. 91.5% of the animals achieved complete recovery and displayed no clinical ocular abnormalities 14 days after surgery according to the published paper mentioned above. In this case, the surgery only resulted in a transient rise in IOP. Compared to crush injury, this was a milder way to induce optic nerve degeneration through elevated IOP. Besides, the relatively large size of the eye bulbs in rats made it accessible for surgical procedures.

Bilateral IOP measurements were performed using a hand-held tonometer. The measurements were repeated at least three times before and after the cauterization of the left eye. The mean values were listed in Table 9. The IOP after cautery on the left side was almost 3.5 times higher than before cautery.

**Table 9: IOP measurements in OHT and control eyes in 5 rats**

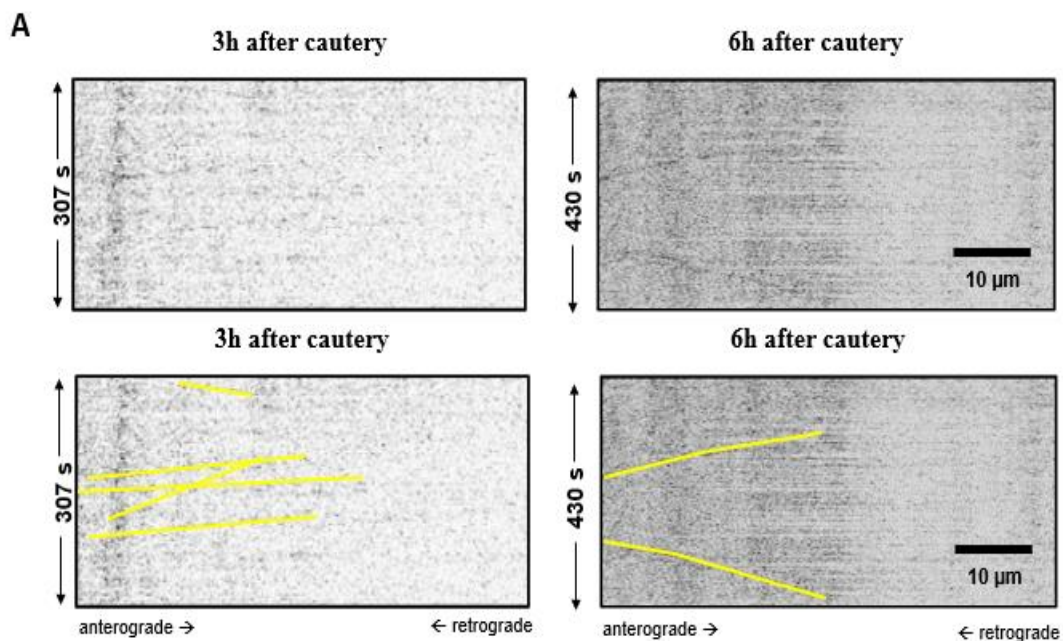
Animals	Cauterization	IOP LE [mmHg]	IOP RE [mmHg]
Animal 1	pre	4.3	8.3
	post	26.67	8
Animal 2	pre	7.67	6.67
	post	18.17	5.67
Animal 3	pre	8.33	9
	post	21.67	5
Animal 4	pre	6.67	9
	post	29.67	8
Animal 5	pre	10	10
	post	18.33	8

#### 3.3.4.2 Evaluation of autophagosome transport in the glaucoma model

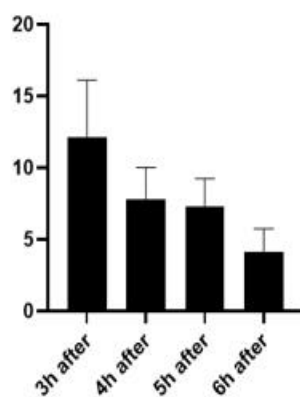
After the successful establishment of a subacute glaucoma model in the left eye as shown in Table 9, the optic nerve was surgically exposed, and live imaging was then carried out from 3 to 6 hours after cautery.

Here, very similar findings were observed compared with the previously crush lesion model. During the 3h of recording time, a substantial reduction in the number of motile autophagosomes was observed, from  $12.14 \pm 3.97$  per minute per mm at 3h after cautery to  $4.15 \pm 1.58$  per minute per mm at 6h after cautery. In contrast, the number of stationary vesicles increased rapidly, with a number of  $144.75 \pm 10.35$  per mm at 6h after cautery,

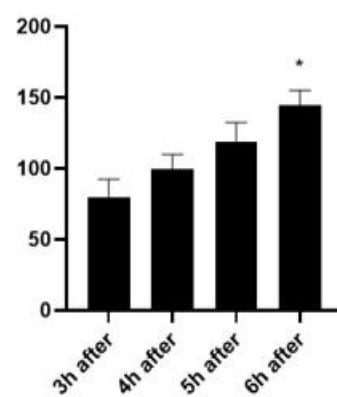
almost twice as many as  $79.21 \pm 13.10$  per mm at 3 h after cautery (Figure 15 C). In the further detection of directionality of motile LC3 vesicles, only a remarkable reduction in the number of retrograde vesicles was found at  $2.75 \pm 1.31$  per minute per mm 6h after cautery, compared to  $8.99 \pm 3.14$  per minute per mm 3h after cautery (Figure 15 D). These findings were consistent with changes in the percentage of different LC3 vesicles at the given time points. Although the percentage of retrogradely moving LC3 vesicles decreased dramatically, there was no big difference in the percentage of anterogradely moving LC3 vesicles at the analyzed time points (Figure 15 F). Furthermore, only the retrograde velocity of LC3 vesicles showed a clear downward trend, from  $397.1 \pm 67.31$  nm/s 3h after cautery to  $238.90 \pm 73.20$  nm/s 6h after cautery (Figure 15 E).



**B** Number of moving LC3 per minute per mm



**C** Number of stationary LC3 per mm



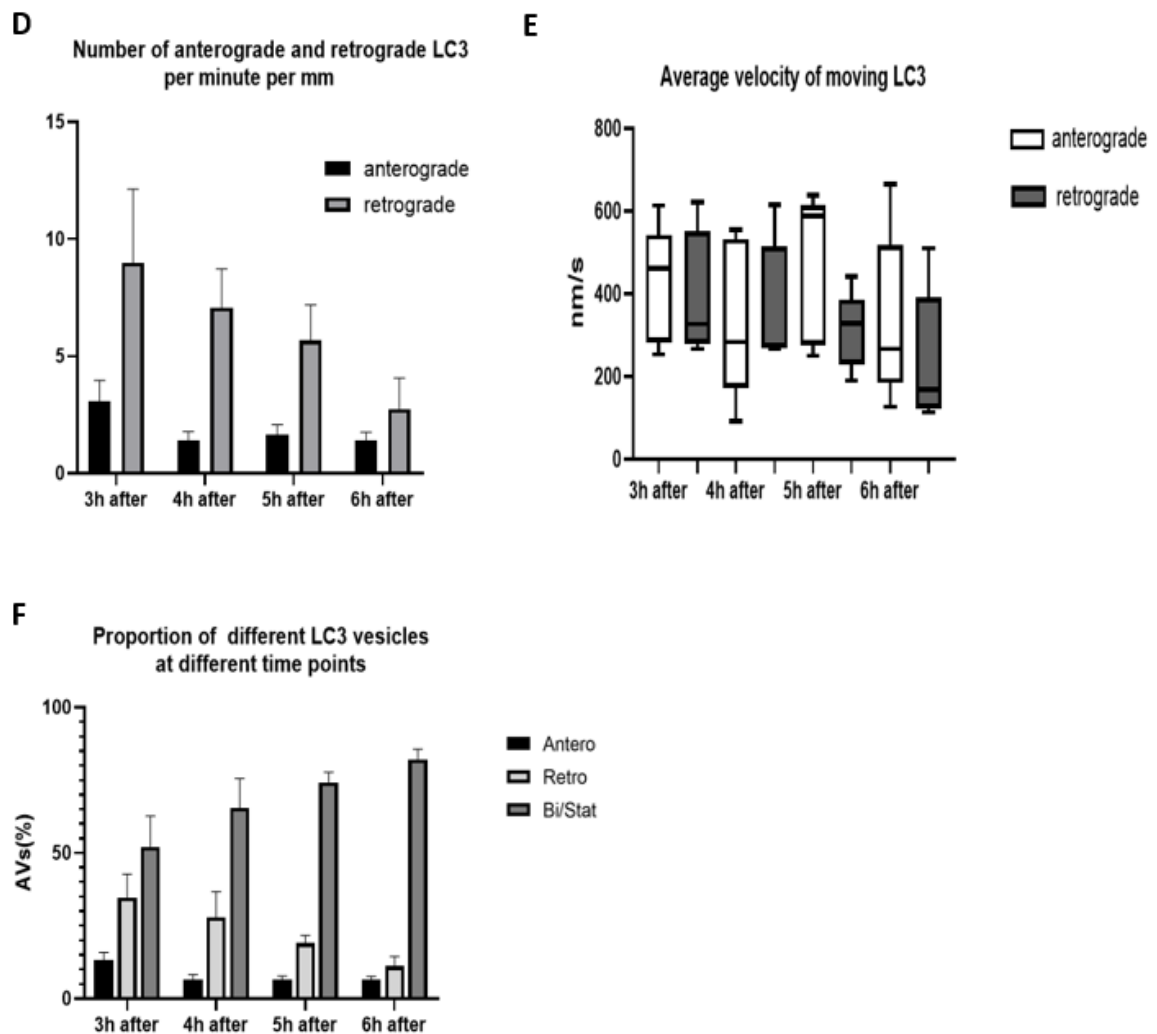


**Figure 15: In vivo autophagosome transport in the optic nerve of rats after cautery.** (A) Representative kymographs and moving trajectories of LC3 transport in the rat optic nerve before and at the given time points after cautery. (B, C, D) Quantification of the number of motile and stationary LC3 vesicles in the optic nerve of rats at the given time points after cautery. (E) Quantification of the average velocity of different moving LC3 vesicles at the given time points after cautery. (F) Quantification of proportions of different LC3 vesicles at the given time points after cautery. In all quantifications, a minimum of 10 axons per time point per animal was evaluated. A total of 5 animals were included. One-way repeated measures ANOVA and Turkey's multiple comparisons test or Friedman test and Dunn's multiple comparisons test were applied based on normality tests of variables.



## 4 Discussion

Axonal degeneration is a prevalent hallmark of normal aging, trauma, and neurodegenerative CNS diseases. As an early event, it usually occurs prior to neuronal cell death, which has potential therapeutic implications (Salvadores et al. 2017). However, attempts to develop efficient axonal neuroprotective therapies have not yet been clinically successful. Given that neurons exhibit a high degree of cellular polarization with distinctive morphological and compartmental specializations, functional axonal transport is important to maintain axonal integrity and normal physiological metabolism (Fang et al. 2012). Therefore, further elucidation of axonal transport enhances our understanding of the mechanisms underlying axonal pathology and contributes to the discovery of new therapeutic avenues against neurodegeneration.

Importantly, autophagy, as a profoundly conserved metabolism of lysosomal degradation, is crucial for neuronal and axonal homeostasis (Maday 2016). Notably, growing evidence suggests that autophagy may exert a dual function in axonal degeneration (Wang et al. 2018). The protective effect is mainly associated with the elimination of dysfunctional organelles and aggregated proteins, while excessive activation of autophagy is thought to promote neuronal loss (Yang et al. 2013). However, the precise function of autophagy in neurodegeneration still remains elusive, although changes in autophagic flux can be indirectly reflected by diverse monitoring analyses of autophagy-related molecules, including autophagic substrates (Yang et al. 2018). Therefore, tools that more precisely display autophagy alterations are required, particularly *in vivo*. Advances in the field of live imaging, especially in animal models, enable us to closely monitor this process and develop a deeper comprehension of autophagy mechanisms (Kerschensteiner et al. 2005; Koch et al. 2011). Based on a previous study in our lab indicating that autophagy was closely linked to axonal degeneration (Knöferle et al. 2010), the present research further explored the dynamic alterations of autophagy in several axonal degeneration models and tried to identify the potential molecular mechanisms.

### 4.1 Dynamic changes in axonal trafficking of autophagosomes after axotomy *in vitro*

Based on the evidence that autophagy contributes to axonal degeneration, we investigated how autophagy kinetics were altered in primary cortical neurons after traumatic injury (Wang et al. 2018; Yang et al. 2013). Axotomy was performed on the axon side, as



described before (Vahsen et al. 2020). We found that the motility of retrograde transport was significantly diminished, although there was no difference in the average velocity over the observation period. According to previous research, autophagosomes are continuously formed at the tip of axons, followed by retrograde movement toward the cell body. (Maday and Holzbaur 2014; Maday et al. 2012). Thus, decreased autophagosome biogenesis after axotomy may be one of the reasons for reduced retrograde transport. Besides, energy deficits can occur after axonal injury due to mitochondrial damage, decreased mitochondrial transport, and increased energy consumption (Sheng 2017). In contrast to the unidirectional treading of kinesin-1 motors, recent *in vitro* and *in vivo* measurements suggest that retrograde transport manifests itself as movement in teams of 6–12 motors, which is not only less efficient than anterograde transport but also requires more energy expenditure (Maday et al. 2014). As a result, retrograde transport is more prone to be impaired than anterograde transport after axonal injury. This could explain why we saw fewer autophagosomes moving retrogradely after axotomy. Moreover, we noticed that after axotomy, the number of autophagosomes at the axon terminal slowly increased, peaked at 2h after axotomy, and declined gradually thereafter, mainly due to a rapid rise in the number of stationary autophagosomes and a relatively slow decline in the number of retrogradely transported vesicles. The reason could be that autophagosomes are temporarily retained in the observed region due to their reduced retrograde motility. However, since the axon tip was removed after axotomy, autophagosome generation was severely disrupted. The total number of autophagosomes had a downward trend since 2h after axotomy, but there was no statistical difference in the given time points compared with the basal condition, probably due to the insufficient observation period and relatively long residual axons in the axonal compartment. Therefore, the later *in vitro* experimental setup was improved by decreasing the number of seeded cortical neurons in the microfluidic chambers in order to achieve a more successful axotomy and shorten the length of the remaining axons on the axon side.

## **4.2 In vivo autophagosome trafficking in axonal degeneration models**

Until now, most of our knowledge about autophagosome trafficking in neuronal cells has come from *in vitro* studies. However, the transport patterns *in vivo*, especially in vertebrate models, have been rarely described (Lopez et al. 2018). Here, a two-photon microscope was used to investigate autophagosome trafficking in the rat optic nerve, based on its relatively easy exposure and manipulation (Koch et al. 2011). We observed

that a significant proportion of LC3 vesicles remained stationary throughout the imaging process. Retrograde vesicles accounted for 85% of the total number of moving vesicles, and the average speed of retrograde transport was also slightly higher than the average speed of anterograde transport. This finding provides an impression of autophagosome transport *in vivo*, allowing us to better understand the physiological function of autophagosomes. Next, autophagosome trafficking was explored in three different models of axonal degeneration: an acute crush injury model, a subacute glaucoma model, and aging. Similar to the *in vitro* data, we found a remarkable increase in the number of stationary autophagosomes but a decline in the number of retrogradely moving vesicles both in the crush lesion model and glaucoma model. In addition, the *in vivo* data also showed a decline in the average velocity of retrograde transport. However, compared with the glaucoma model, autophagosome trafficking changed more rapidly in the crush injury model. Overall, the total number of autophagosomes continued to rise following degeneration induction, consistent with a great deal of research on neurodegenerative diseases showing autophagosome accumulation, but our study illustrated a dynamic process of changes in autophagosome trafficking (Ciechanover and Kwon 2015; Park et al. 2020).

In terms of aging, the motility of autophagosome trafficking, especially retrograde transport, was significantly impaired compared with young animals. Additionally, the total number of autophagosomes increased substantially, which was in line with a previous study in our lab demonstrating that aged animals contained more LC3 puncta than young animals in the optic nerve through fluorescence staining (data not shown). These findings may imply that autophagosomes within the imaged areas were accumulated because of transport defects. However, it was still insufficient to evaluate whether this increase represented an induction or blockade of autophagy. Furthermore, autophagosome biogenesis and autophagic activities with age are still inconsistent among different species (Stavoe AKH and Holzbaur 2019b). For example, in mouse DRG neurons, a reduction in autophagosome biogenesis at axon terminals with increasing age was observed by quantifying the formation of GFP-LC3B-positive puncta (Stavoe AK et al. 2019). Meanwhile, another study also found that hippocampal autophagy activity in mice decreased during aging (Glatigny et al. 2019). On the contrary, transcriptome and proteome analysis in rat brains revealed no significant alterations in the components of the autophagy pathway between 6 months and 24 months (Ori et al. 2015). Overall, since the effect of age on neuronal autophagy seems to be more variable than that on other tissues (Chang et al. 2017), we emphasize that additional experiments are required to

completely comprehend the role of autophagy in aging.

### **4.3 Fusion of autophagosomes and lysosomes following axonal injury**

Considering that autophagosome-lysosome fusion is a prerequisite for the degradation of autophagic substrates, the fusion ratio was assessed both *in vitro* and *in vivo*. Since lysosomes act as degradation hubs for autophagic components, choosing appropriate markers for lysosomes increases confidence in the accuracy of the assessment. Although LAMP1 is commonly employed as a marker for lysosomes, and LAMP1-positive organelles are conventionally identified as lysosomes, a substantial proportion of lamp1-labeled organelles lacks lysosomal hydrolases, implying that they are actually not lysosomes (Cheng et al. 2018). To this end, cathepsin D, an aspartyl protease that mainly exists within lysosomes, was used to label lysosomes in this thesis.

Given that maintaining an acidic environment is necessary to activate hydrolases and then degrade cellular components, BODIPY-pepstatin A was chosen to specifically visualize activated cathepsin D with a pH of 4.5 in acidic environments *in vitro* (Chen et al. 2000). However, it is not easy to find effective probes *in vivo* that label not only an acidic environment but also lysosomal hydrolases. Hence, we only performed cathepsin D staining. In this case, all isoforms of cathepsin D were visualized. It should be noted that when interpreting, endosomes were also labeled in addition to lysosomes, as endosomes usually deliver newly synthesized lysosomal enzymes and membrane proteins to lysosomes (Barral et al. 2022).

*In vitro*, within the imaging period of 6h after axotomy, we observed a substantial decline in the number of LC3 vesicles and active cathepsin D. Besides, the colocalization ratio of LC3 and active cathepsin D was also significantly decreased. Regarding the fusion of autophagosomes and endosomes/lysosomes following acute axonal degeneration *in vivo*, Pearson's correlation coefficients demonstrated a notable increase in the distal but not proximal parts of the optic nerve compared to the contralateral unlesioned control, indicating the accumulation of fused autophagosomes and endosomes/lysosomes at the distal stump. However, there was no difference between the unlesioned control and the proximal terminals.

Furthermore, since successful autophagic degradation relies on the fusion of autophagosomes with multiple late endosomes/lysosomes to maintain an adequately acidic environment for hydrolases to function (Jahreiss et al. 2008; Zhao and Zhang 2019), this finding may imply that axonal injury leads to impaired autophagosome maturation.

As a result, autophagosomes are unable to turn over and accumulate as nondegradable autophagic vacuoles, which have been widely reported in both neurodegenerative diseases and traumatic neuropathies (Ray 2020; Wu and Lipinski 2019; Zhao et al. 2021).

#### **4.4 Autophagy is induced following acute axonal injury in vivo**

To explore autophagy induction after crush lesion of the optic nerve, fluorescence staining of p-ATG16L1 and the expression levels of the autophagic pathway components were examined. The staining showed that p-ATG16L1 puncta were abundant on both sides of the lesion site, while the signal was barely visible in the uninjured control. Besides, the level of p-ATG16L1 is intimately linked to autophagy biogenesis (Tian et al. 2020). Hence, upregulation of p-ATG16L1 expression may indicate an increase in newly synthesized autophagosomes. Despite previous descriptions of autophagosome biogenesis preferentially occurring at the distal tip of axons under physiological conditions, mid-axons still exhibited a limited amount of autophagosome generation (Maday and Holzbaur 2014). After axonal injury, the massive demand for substrate degradation as well as cellular reconstruction, especially at the lesion site, may have altered the original autophagosome biosynthesis pattern but this still remains to be validated by additional studies.

Corresponding to our p-ATG16L1 fluorescence result, a notable increase in the LC3 II/I ratio, an indicator of autophagic turnover (Klionsky et al. 2008), and higher levels of the autophagic substrate p62 were observed on the proximal and distal sides of the optic nerve 6h after lesion. This was consistent with previous studies in our laboratory in which LC3 and p62 expression levels were quantified by fluorescent staining (Knöferle et al. 2010; Koch et al. 2010). Overall, these findings above could therefore indicate that axonal injury leads to autophagy activation with increased degradation of cellular material or blockage of autophagic flux.

#### **4.5 Degradative capacity in the autophagy pathway is impaired after axonal lesion**

Considering the vital role of lysosomal hydrolases in autophagic degradation, protein levels of cathepsin D were evaluated following axonal injury. 6h after the crush lesion, mature cathepsin D levels were considerably lowered at both terminals of the optic nerve, but immature cathepsin D levels were exclusively reduced on the distal side because of the supplement from the adjacent cell body in the proximity, compared with control.

Additionally, reduced protein levels and activity of cathepsin D were also recently detected, along with impaired autophagic flux after CNS trauma, including traumatic brain injury (TBI) and spinal cord injury (SCI) (Lipinski et al. 2015; Sarkar et al. 2014). However, since intraluminal acidification (Song et al. 2020) and microtubule-dependent axonal transport (Ferguson 2018; Lee et al. 2011) are both crucial for the efficient operation of the lysosomal digestive system, it still remains to be clarified by further research which process is dominant or whether this is a result of their interaction.

#### **4.6 Crush lesion selectively disrupts the retrograde axonal transport in the optic nerve**

Having demonstrated significant defects in retrograde transport of autophagosomes following crush lesion to the optic nerve, we aimed to explore the underlying molecular mechanisms. After assessing the levels of several key motor proteins involved in autophagosome transport, a significant reduction in p150Glued was found after axonal injury, but no significant difference in dynein. P150Glued is the biggest component of the dynactin complex, which facilitates dynein activation and, together with dynein, effectively enables the long-distance retrograde transport of cargo (Kobayashi et al. 2006; McKenney et al. 2014). Hence, p150Glued deficiency could reasonably explain our previous finding of severely impaired retrograde transport following crush lesion in the optic nerve. Consistently, recently published studies have also shown that the G59S mutation in p150Glued and the depletion of p150Glued causes a partial loss of capacity of dynein/dynactin-mediated retrograde transport and the accumulation of retrogradely transported cargos, such as synaptophysin or autophagosomes, thus exacerbating neurodegeneration (Bercier et al. 2019; Ikenaka et al. 2013; Lai et al. 2007).

To date, it is unknown why the optic nerve crush selectively caused the reduction in p150Glued. In fact, compared to dynein, dynactin1/p150Glued is more vulnerable to toxic exposures, especially excitotoxicity (Katsuno et al. 2006; Xu et al. 2021). Recently, a growing body of evidence has suggested that glutamate levels appear elevated after traumatic optic nerve injury, as well as upregulation of glutamate transporter mRNA (Mawrin et al. 2003; Vorwerk et al. 2004). Moreover, the administration of glutamate antagonists or blockers of glutamate receptors provided neuroprotective effects (Schmitt and Sabel 1996; Vorwerk et al. 2001). Accordingly, we hypothesize that glutamate excitotoxicity induced by optic nerve injury may adversely affect p150Glued. Interestingly, Fujiwara et al. found that glutamate excitotoxicity generated a variant form

of p150Glued with C-terminal truncation, thus exacerbating axonal degeneration. Consistently, overexpression of p150Glued attenuated axonal degeneration and suppressed cell body death (Fujiwara et al. 2012). However, this study also showed a 35% drop in the dynein intermediate chain (DIC). Therefore, lesion-induced glutamate excitotoxicity alone may not adequately explain our findings.

Another possible explanation is that p150Glued was cleaved by caspases during cellular apoptosis, but dynein intermediate chain (DIC) was decreased even more rapidly in this process (Lane et al. 2001). Since apoptosis generally occurs relatively late after trauma, this is not well aligned with our findings that the impaired motility of retrograde transport happened rapidly following crush injury.

Thus, we demonstrate that decreased p150Glued is correlated to the breakdown of retrograde transport of autophagosomes in a model of lesion-induced axonal degeneration. Besides, p150Glued may be engaged in various cellular processes and could be influenced by multiple factors. However, the reason for its rapid decrease is currently unclear and needs to be elucidated by further studies.

#### **4.7 Conclusion**

In conclusion, this study has shown that the retrograde transport capacity of autophagosomes is significantly diminished in multiple models of CNS trauma and neurodegenerative diseases, both in vitro and in vivo. Specifically, in the rat optic nerve crush model, autophagy is dramatically activated, but impaired retrograde transport results in the accumulation of autophagosomes as well as increased cellular materials that need degradation; moreover, the lysosomal degradative capacity is also damaged. Although the retrograde mobility of autophagosomes was reduced, it seems not to affect the fusion with other vesicles in the autophagic pathway. Mechanistically, the significant reduction of p150Glued may contribute to the severe impairment of retrograde transport in this model, which may represent a potential therapeutic target for traumatic and neurodegenerative diseases of the central nervous system.

## 5 Summary

Axonal degeneration represents a prevalent and early pathophysiological manifestation observed in various traumatic and neurodegenerative diseases of the central nervous system. It usually leads to progressive dysfunction of damaged neurons as a consequence of their reduced inherent regenerative potential and increased external growth inhibitors. Since current therapeutic strategies are very limited and can only delay the progression of CNS diseases, there is an urgent need for a more profound comprehension of the molecular mechanisms underlying axonal degeneration to identify prospective therapeutic targets. During axonal degeneration, autophagy, a conserved degradation mechanism of lysosomes, is indispensable for maintaining neuronal axonal homeostasis by controlling cellular protein and organelle quality. However, although autophagy has been previously demonstrated to be closely associated with axonal degeneration, its exact role in this process is still unclear. In particular, given the complexity of autophagic activity, the accumulation of autophagosomes in degenerating axons remains difficult to identify whether the autophagic flux is activated or the autophagic process is blocked, especially *in vivo* with existing tools.

To dynamically monitor autophagic changes in axonal degeneration, autophagosomes were visualized in primary cortical neurons and in the optic nerve transduced with an adenovirus-associated viral vector expressing LC3, a standard marker of autophagosomes. After selective neuronal axonal injury in microfluidic chambers, the retrograde movements of autophagosomes were compromised, and the number of stationary vesicles increased significantly compared to the basal state. Similarly, in the optic nerve crush model and the subacute glaucoma model *in vivo*, the retrograde transport capacity of autophagosomes was also impaired, as evidenced by a noticeable decrease in the amount and speed of retrogradely moving vesicles. In addition, in the aging model, old rats at 18 months of age also had fewer autophagosomes moving backward and a slower velocity of retrograde transport, accompanied by increased number of stationary vesicles, compared to 3-month-old young rats. We next explored the potential mechanism of impaired retrograde transport of autophagosomes in the model of optic nerve crush. The induction of autophagy following axonal injury was confirmed by fluorescence staining of p-ATG16L1 locally at lesion site of the optic nerve and by immunoblotting of the LC3-II/I ratio. Further, the decrease in the proportion of LC3 that overlapped with active cathepsin D *in vitro* and the increased LC3 vesicles positive for cathepsin D that accumulated on the distal sides of the optic nerve *in vivo* after axonal lesion suggested

that axonal injury may not affect the autophagosome and endosome/lysosome fusion. Additionally, decreased levels of mature cathepsin D after optic nerve injury indicated impaired hydrolytic capacity of lysosomes. Thus, elevated p62 protein levels in this process were indicative of deficits in autophagic degradation, which meant the blockade of autophagic flux. Apart from that, the detection of key motor protein levels in the optic nerve following crush injury revealed a substantial decrease in p150Glued, which may account for the impaired retrograde transport of autophagosomes.

Together, the findings of this thesis provide further insight into the function of retrograde transport of axonal autophagosomes in CNS trauma and degenerative diseases. Additionally, we find that the retrograde transporter protein p150Glued holds promise as a potentially innovative target for therapeutic intervention in lesion-induced neurodegeneration. However, the detailed mechanism of p150Glued changes during this process remains to be clarified.



## 6 Bibliography

Adalbert R, Coleman MP (2013): Review: Axon pathology in age-related neurodegenerative disorders. *Neuropathol Appl Neurobiol* 39, 90-108

Akamatsu Y, Hanafy KA (2020): Cell Death and Recovery in Traumatic Brain Injury. *Neurotherapeutics* 17, 446-456

Almasieh M, Wilson AM, Morquette B, Cueva Vargas JL, Di Polo A (2012): The molecular basis of retinal ganglion cell death in glaucoma. *Prog Retin Eye Res* 31, 152-181

Barral DC, Staiano L, Guimas Almeida C, Cutler DF, Eden ER, Futter CE, Galione A, Marques ARA, Medina DL, Napolitano G, et al. (2022): Current methods to analyze lysosome morphology, positioning, motility and function. *Traffic* 23, 238-269

Benes P, Vetvicka V, Fusek M (2008): Cathepsin D--many functions of one aspartic protease. *Crit Rev Oncol Hematol* 68, 12-28

Bercier V, Hubbard JM, Fidelin K, Durore K, Auer TO, Revenu C, Wyart C, Del Bene F (2019): Dynactin1 depletion leads to neuromuscular synapse instability and functional abnormalities. *Mol Neurodegener* 14, 27

Bjørkøy G, Lamark T, Pankiv S, Øvervatn A, Brech A, Johansen T (2009): Monitoring autophagic degradation of p62/SQSTM1. *Methods Enzymol* 452, 181-197

Bolte S, Cordelières FP (2006): A guided tour into subcellular colocalization analysis in light microscopy. *J Microsc* 224, 213-232

Chang JT, Kumsta C, Hellman AB, Adams LM, Hansen M (2017): Spatiotemporal regulation of autophagy during aging. *Elife* 6, e18459

Chen CS, Chen WN, Zhou M, Arttamangkul S, Haugland RP (2000): Probing the cathepsin D using a BODIPY FL-pepstatin A: applications in fluorescence polarization and microscopy. *J Biochem Biophys Methods* 42, 137-151

Chen YA, Scheller RH (2001): SNARE-mediated membrane fusion. *Nature Reviews Molecular Cell Biology* 2, 98-106

Cheng XT, Xie YX, Zhou B, Huang N, Farfel-Becker T, Sheng Z-H (2018): Characterization of LAMP1-labeled nondegradative lysosomal and endocytic compartments in neurons. *J Cell Biol* 217, 3127-3139

Chi H, Chang HY, Sang TK (2018): Neuronal Cell Death Mechanisms in Major Neurodegenerative Diseases. *Int J Mol Sci* 19, 3082

Chow HM, Herrup K (2015): Genomic integrity and the ageing brain. *Nat Rev Neurosci* 16, 672-684

Ciechanover A, Kwon YT (2015): Degradation of misfolded proteins in neurodegenerative diseases: therapeutic targets and strategies. *Exp Mol Med* 47, e147

Coleman M (2005): Axon degeneration mechanisms: commonality amid diversity. *Nat Rev Neurosci* 6, 889-898

- Coleman MP, Höke A (2020): Programmed axon degeneration: from mouse to mechanism to medicine. *Nat Rev Neurosci* 21, 183-196
- Conforti L, Gilley J, Coleman MP (2014): Wallerian degeneration: an emerging axon death pathway linking injury and disease. *Nat Rev Neurosci* 15, 394-409
- Conforti L, Tarlton A, Mack TG, Mi W, Buckmaster EA, Wagner D, Perry VH, Coleman MP (2000): A Ufd2/D4Cole1e chimeric protein and overexpression of Rbp7 in the slow Wallerian degeneration (WldS) mouse. *Proc Natl Acad Sci U S A* 97, 11377-11382
- Crish SD, Sappington RM, Inman DM, Horner PJ, Calkins DJ (2010): Distal axonopathy with structural persistence in glaucomatous neurodegeneration. *Proc Natl Acad Sci U S A* 107, 5196-5201
- Czogalla A, Sikorski AF (2005): Spectrin and calpain: a 'target' and a 'sniper' in the pathology of neuronal cells. *Cell Mol Life Sci* 62, 1913-1924
- Davis BM, Crawley L, Pahlitzsch M, Javaid F, Cordeiro MF (2016): Glaucoma: the retina and beyond. *Acta Neuropathol* 132, 807-826
- Dias MS, Luo X, Ribas VT, Peters SH, Koch JC (2022): The Role of Axonal Transport in Glaucoma. *Int J Mol Sci* 23, 3935
- Fang C, Bourdette D, Banker G (2012): Oxidative stress inhibits axonal transport: implications for neurodegenerative diseases. *Mol Neurodegener* 7, 29
- Ferguson SM (2018): Axonal transport and maturation of lysosomes. *Curr Opin Neurobiol* 51, 45-51
- Fischer LR, Culver DG, Tennant P, Davis AA, Wang M, Castellano-Sanchez A, Khan J, Polak MA, Glass JD (2004): Amyotrophic lateral sclerosis is a distal axonopathy: evidence in mice and man. *Exp Neurol* 185, 232-240
- Fu MM, Holzbaur ELF (2014): MAPK8IP1/JIP1 regulates the trafficking of autophagosomes in neurons. *Autophagy* 10, 2079-2081
- Fujiwara T, Morimoto K, Kakita A, Takahashi H (2012): Dynein and dynactin components modulate neurodegeneration induced by excitotoxicity. *J Neurochem* 122, 162-174
- Gerdt J, Brace EJ, Sasaki Y, DiAntonio A, Milbrandt J (2015): SARM1 activation triggers axon degeneration locally via NAD<sup>+</sup> destruction. *Science* 348, 453-457
- Gilley J, Coleman MP (2010): Endogenous Nmnat2 is an essential survival factor for maintenance of healthy axons. *PLoS Biol* 8, e1000300
- Glatigny M, Moriceau S, Rivagorda M, Ramos-Brossier M, Nascimbeni AC, Lante F, Shanley MR, Boudarene N, Rousseaud A, Friedman AK, et al. (2019): Autophagy Is Required for Memory Formation and Reverses Age-Related Memory Decline. *Curr Biol* 29, 435-448
- Grasso D, Renna FJ, Vaccaro MI (2018): Initial Steps in Mammalian Autophagosome Biogenesis. *Front Cell Dev Biol* 6, 146
- Guo F, Liu X, Cai H, Le W (2018): Autophagy in neurodegenerative diseases:

pathogenesis and therapy. *Brain Pathol* 28, 3-13

Gupta N, Yücel YH (2007): Glaucoma as a neurodegenerative disease. *Curr Opin Ophthalmol* 18, 110-114

Hill CS, Coleman MP, Menon DK (2016): Traumatic Axonal Injury: Mechanisms and Translational Opportunities. *Trends Neurosci* 39, 311-324

Horton AC, Ehlers MD (2003): Neuronal polarity and trafficking. *Neuron* 40, 277-295

Hou Y, Dan X, Babbar M, Wei Y, Hasselbalch SG, Croteau DL, Bohr VA (2019): Ageing as a risk factor for neurodegenerative disease. *Nat Rev Neurol* 15, 565-581

Ikenaka K, Kawai K, Katsuno M, Huang Z, Jiang Y-M, Iguchi Y, Kobayashi K, Kimata T, Waza M, Tanaka F, et al. (2013): dnc-1/dynactin 1 knockdown disrupts transport of autophagosomes and induces motor neuron degeneration. *PLoS One* 8, e54511

Jaeger PA, Wyss CT (2009): All-you-can-eat: autophagy in neurodegeneration and neuroprotection. *Mol Neurodegener* 4, 16

Jahreiss L, Menzies FM, Rubinsztein DC (2008): The itinerary of autophagosomes: from peripheral formation to kiss-and-run fusion with lysosomes. *Traffic* 9, 574-587

Kang JM, Tanna AP (2021): Glaucoma. *Med Clin North Am* 105, 493-510

Katsuno M, Adachi H, Minamiyama M, Waza M, Tokui K, Banno H, Suzuki K, Onoda Y, Tanaka F, Doyu M, et al. (2006): Reversible disruption of dynactin 1-mediated retrograde axonal transport in polyglutamine-induced motor neuron degeneration. *J Neurosci* 26, 12106-12117

Kaushik S, Cuervo AM (2018): The coming of age of chaperone-mediated autophagy. *Nat Rev Mol Cell Biol* 19, 365-381

Kerschensteiner M, Schwab ME, Lichtman JW, Misgeld T (2005): In vivo imaging of axonal degeneration and regeneration in the injured spinal cord. *Nat Med* 11, 572-577

King JS, Veltman DM, Insall RH (2011): The induction of autophagy by mechanical stress. *Autophagy* 7, 1490-1499

Klionsky DJ, Abeliovich H, Agostinis P, Agrawal DK, Aliev G, Askew DS, Baba M, Baehrecke EH, Bahr BA, Ballabio A, et al. (2008): Guidelines for the use and interpretation of assays for monitoring autophagy in higher eukaryotes. *Autophagy* 4, 151-175

Knöferle J, Koch JC, Ostendorf T, Michel U, Planchamp V, Vutova P, Tönges L, Stadelmann C, Brück W, Bähr M, et al. (2010): Mechanisms of acute axonal degeneration in the optic nerve in vivo. *Proc Natl Acad Sci U S A* 107, 6064-6069

Kobayashi T, Shiroguchi K, Edamatsu M, Toyoshima YY (2006): Microtubule-binding properties of dynactin p150 expedient for dynein motility. *Biochem Biophys Res Commun* 340, 23-28

Koch JC, Knöferle J, Tönges L, Ostendorf T, Bähr M, Lingor P (2010): Acute axonal degeneration in vivo is attenuated by inhibition of autophagy in a calcium-dependent manner. *Autophagy* 6, 658-659

Koch JC, Knöferle J, Tönges L, Michel U, Bähr M, Lingor P (2011): Imaging of rat optic nerve axons in vivo. *Nat Protoc* 6, 1887-1896

Lai C, Lin X, Chandran J, Shim H, Yang WJ, Cai H (2007): The G59S mutation in p150(glued) causes dysfunction of dynactin in mice. *J Neurosci* 27, 13982-13990

Lane JD, Vergnolle MA, Woodman PG, Allan VJ (2001): Apoptotic cleavage of cytoplasmic dynein intermediate chain and p150(Glued) stops dynein-dependent membrane motility. *J Cell Biol* 153, 1415-1426

Lani R, Dias MS, Abreu CA, Araújo VG, Gonçalo T, Nascimento-Dos-Santos G, Dantas AM, Allodi S, Fiorani M, Petrs-Silva H, et al. (2019): A subacute model of glaucoma based on limbal plexus cautery in pigmented rats. *Sci Rep* 9, 16286

Lee JA (2009): Autophagy in neurodegeneration: two sides of the same coin. *BMB Rep* 42, 324-330

Lee S, Sato Y, Nixon RA (2011): Lysosomal proteolysis inhibition selectively disrupts axonal transport of degradative organelles and causes an Alzheimer's-like axonal dystrophy. *J Neurosci* 31, 7817-7830

Lingor P, Koch JC, Tönges L, Bähr M (2012): Axonal degeneration as a therapeutic target in the CNS. *Cell Tissue Res* 349, 289-311

Lipinski MM, Wu J, Faden AI, Sarkar C (2015): Function and Mechanisms of Autophagy in Brain and Spinal Cord Trauma. *Antioxid Redox Signal* 23, 565-577

Liu WJ, Ye L, Huang WF, Guo LJ, Xu ZG, Wu HL, Yang C, Liu HF (2016): p62 links the autophagy pathway and the ubiquitin-proteasome system upon ubiquitinated protein degradation. *Cell Mol Biol Lett* 21, 29

López OC, Blasco MA, Partridge L, Serrano M, Kroemer G (2013): The hallmarks of aging. *Cell* 153, 1194-1217

Lopez A, Fleming A, Rubinsztein DC (2018): Seeing is believing: methods to monitor vertebrate autophagy. *Open Biol* 8, 180106

Ma M (2013): Role of calpains in the injury-induced dysfunction and degeneration of the mammalian axon. *Neurobiol Dis* 60, 61-79

Maday S (2016): Mechanisms of neuronal homeostasis: Autophagy in the axon. *Brain Res* 1649, 143-150

Maday S, Holzbaur ELF (2014): Autophagosome biogenesis in primary neurons follows an ordered and spatially regulated pathway. *Dev Cell* 30, 71-85

Maday S, Wallace KE, Holzbaur ELF (2012): Autophagosomes initiate distally and mature during transport toward the cell soma in primary neurons. *J Cell Biol* 196, 407-417

Maday S, Twelvetrees AE, Moughamian AJ, Holzbaur ELF (2014): Axonal transport: cargo-specific mechanisms of motility and regulation. *Neuron* 84, 292-309

Maddineni P, Kasetti RB, Patel PD, Millar JC, Kiehlbauch C, Clark AF, Zode GS (2020): CNS axonal degeneration and transport deficits at the optic nerve head precede structural and functional loss of retinal ganglion cells in a mouse model of glaucoma. *Mol*

Neurodegener 15, 48

Martinet W, Agostinis P, Vanhoecke B, Dewaele M, De Meyer GRY (2009): Autophagy in disease: a double-edged sword with therapeutic potential. *Clin Sci (Lond)* 116, 697-712

Mattedi F, Vagnoni A (2019): Temporal Control of Axonal Transport: The Extreme Case of Organismal Ageing. *Front Cell Neurosci* 13, 393

Mawrin C, Pap T, Pallas M, Dietzmann K, Behrens-Baumann W, Vorwerk CK (2003): Changes of retinal glutamate transporter GLT-1 mRNA levels following optic nerve damage. *Mol Vis* 9, 10-13

McKenney RJ, Huynh W, Tanenbaum ME, Bhabha G, Vale RD (2014): Activation of cytoplasmic dynein motility by dynactin-cargo adapter complexes. *Science* 345, 337-341

McKinnon SJ, Schlamp CL, Nickells RW (2009): Mouse models of retinal ganglion cell death and glaucoma. *Exp Eye Res* 88, 816-824

McQuarrie IG, Brady ST, Lasek RJ (1989): Retardation in the slow axonal transport of cytoskeletal elements during maturation and aging. *Neurobiol Aging* 10, 359-365

Melia TJ, Lystad AH, Simonsen A (2020): Autophagosome biogenesis: From membrane growth to closure. *J Cell Biol* 219, e202002085

Mellone M, Kestoras D, Andrews MR, Dassie E, Crowther RA, Stokin GB, Tinsley J, Horne G, Goedert M, Tolkovsky AM, et al. (2013): Tau pathology is present in vivo and develops in vitro in sensory neurons from human P301S tau transgenic mice: a system for screening drugs against tauopathies. *J Neurosci* 33, 18175-18189

Menzies FM, Fleming A, Rubinsztein DC (2015): Compromised autophagy and neurodegenerative diseases. *Nat Rev Neurosci* 16, 345-357

Menzies FM, Fleming A, Caricasole A, Bento CF, Andrews SP, Ashkenazi A, Füllgrabe J, Jackson A, Jimenez Sanchez M, Karabiyik C, et al. (2017): Autophagy and Neurodegeneration: Pathogenic Mechanisms and Therapeutic Opportunities. *Neuron* 93, 1015-1034

Metwally E, Zhao G, Zhang YQ (2021): The calcium-dependent protease calpain in neuronal remodeling and neurodegeneration. *Trends Neurosci* 44, 741-752

Mijaljica D, Prescott M, Devenish RJ (2011): Microautophagy in mammalian cells: revisiting a 40-year-old conundrum. *Autophagy* 7, 673-682

Millar JC, Pang I-H (2015): Non-continuous measurement of intraocular pressure in laboratory animals. *Exp Eye Res* 141, 74-90

Millecamps S, Julien JP (2013): Axonal transport deficits and neurodegenerative diseases. *Nat Rev Neurosci* 14, 161-176

Minoshima S, Cross D (2008): In vivo imaging of axonal transport using MRI: aging and Alzheimer's disease. *Eur J Nucl Med Mol Imaging* 35 Suppl 1, S89-S92

Moldovan M, Alvarez S, Krarup C (2009): Motor axon excitability during Wallerian degeneration. *Brain* 132, 511-523

Nakamura S, Yoshimori T (2017): New insights into autophagosome-lysosome fusion. *J Cell Sci* 130, 1209-1216

Neumann S, Chassefeyre R, Campbell GE, Encalada SE (2017): KymoAnalyzer: a software tool for the quantitative analysis of intracellular transport in neurons. *Traffic* 18, 71-88

Nikoletopoulou V, Papandreou ME, Tavernarakis N (2015): Autophagy in the physiology and pathology of the central nervous system. *Cell Death Differ* 22, 398-407

Noda NN, Fujioka Y, Hanada T, Ohsumi Y, Inagaki F (2013): Structure of the Atg12-Atg5 conjugate reveals a platform for stimulating Atg8-PE conjugation. *EMBO Rep* 14, 206-211

Ori A, Toyama BH, Harris MS, Bock T, Iskar M, Bork P, Ingolia NT, Hetzer MW, Beck M (2015): Integrated Transcriptome and Proteome Analyses Reveal Organ-Specific Proteome Deterioration in Old Rats. *Cell Syst* 1, 224-237

Osterloh JM, Yang J, Rooney TM, Fox AN, Adalbert R, Powell EH, Sheehan AE, Avery MA, Hackett R, Logan MA, et al. (2012): dSarm/Sarm1 is required for activation of an injury-induced axon death pathway. *Science* 337, 481-484

Pang IH, Clark AF (2020): Inducible rodent models of glaucoma. *Prog Retin Eye Res* 75, 100799

Park H, Kang JH, Lee S (2020): Autophagy in Neurodegenerative Diseases: A Hunter for Aggregates. *Int J Mol Sci* 21

Park JW, Vahidi B, Taylor AM, Rhee SW, Jeon NL (2006): Microfluidic culture platform for neuroscience research. *Nat Protoc* 1, 2128-2136

Parzych KR, Klionsky DJ (2014): An overview of autophagy: morphology, mechanism, and regulation. *Antioxid Redox Signal* 20, 460-473

Qu J, Wang D, Grosskreutz CL (2010): Mechanisms of retinal ganglion cell injury and defense in glaucoma. *Exp Eye Res* 91, 48-53

Ray SK (2020): Modulation of autophagy for neuroprotection and functional recovery in traumatic spinal cord injury. *Neural Regen Res* 15, 1601-1612

Ribas VT, Koch JC, Michel U, Bähr M, Lingor P (2017): Attenuation of Axonal Degeneration by Calcium Channel Inhibitors Improves Retinal Ganglion Cell Survival and Regeneration After Optic Nerve Crush. *Mol Neurobiol* 54, 72-86

Robichaud S, Rasheed A, Pietrangelo A, Doyoung Kim A, Boucher DM, Emerton C, Vijithakumar V, Gharibeh L, Fairman G, Mak E, et al. (2022): Autophagy Is Differentially Regulated in Leukocyte and Nonleukocyte Foam Cells During Atherosclerosis. *Circ Res* 130, 831-847

Rodríguez RS, Fernández-Morera JL, Menéndez-Torre E, Calvanese V, Fernández AF, Fraga MF (2011): Aging genetics and aging. *Aging Dis* 2, 186-195

Rose MR (2009): Adaptation, aging, and genomic information. *Aging (Albany NY)* 1, 444-450

Russell RC, Tian Y, Yuan H, Park HW, Chang Y-Y, Kim J, Kim H, Neufeld TP, Dillin

- A, Guan KL (2013): ULK1 induces autophagy by phosphorylating Beclin-1 and activating VPS34 lipid kinase. *Nat Cell Biol* 15, 741-750
- Salvadores N, Sanhueza M, Manque P, Court FA (2017): Axonal Degeneration during Aging and Its Functional Role in Neurodegenerative Disorders. *Front Neurosci* 11, 451
- Sarkar C, Zhao Z, Aungst S, Sabirzhanov B, Faden AI, Lipinski MM (2014): Impaired autophagy flux is associated with neuronal cell death after traumatic brain injury. *Autophagy* 10, 2208-2222
- Schmitt U, Sabel BA (1996): MK-801 reduces retinal ganglion cell survival but improves visual performance after controlled optic nerve crush. *J Neurotrauma* 13, 791-800
- Schuster AK, Erb C, Hoffmann EM, Dietlein T, Pfeiffer N (2020): The Diagnosis and Treatment of Glaucoma. *Dtsch Arztebl Int* 117, 225-234
- Sheng ZH (2017): The Interplay of Axonal Energy Homeostasis and Mitochondrial Trafficking and Anchoring. *Trends Cell Biol* 27, 403-416
- Sleigh J, Schiavo G (2016): Older but not slower: aging does not alter axonal transport dynamics of signalling endosomes in vivo. *Matters* 2016, 1-6
- Song Q, Meng B, Xu H, Mao Z (2020): The emerging roles of vacuolar-type ATPase-dependent Lysosomal acidification in neurodegenerative diseases. *Transl Neurodegener* 9, 17
- Stavoe AK, Gopal PP, Gubas A, Tooze SA, Holzbaur EL (2019): Expression of WIPI2B counteracts age-related decline in autophagosome biogenesis in neurons. *Elife* 8, e44219
- Stavoe AKH, Holzbaur ELF (2019a): Axonal autophagy: Mini-review for autophagy in the CNS. *Neurosci Lett* 697, 17-23
- Stavoe AKH, Holzbaur ELF (2019b): Autophagy in Neurons. *Annu Rev Cell Dev Biol* 35, 477-500
- Stjepanovic G, Baskaran S, Lin MG, Hurley JH (2017): Unveiling the role of VPS34 kinase domain dynamics in regulation of the autophagic PI3K complex. *Mol Cell Oncol* 4, e1367873
- Takahara Y, Inatani M, Eto K, Inoue T, Kreymerman A, Miyake S, Ueno S, Nagaya M, Nakanishi A, Iwao K, et al. (2015): In vivo imaging of axonal transport of mitochondria in the diseased and aged mammalian CNS. *Proc Natl Acad Sci U S A* 112, 10515-10520
- Tham YC, Li X, Wong TY, Quigley HA, Aung T, Cheng C-Y (2014): Global prevalence of glaucoma and projections of glaucoma burden through 2040: a systematic review and meta-analysis. *Ophthalmology* 121, 2081-2090
- Tian W, Alsaadi R, Guo Z, Kalinina A, Carrier M, Tremblay M-E, Lacoste B, Lagace D, Russell RC (2020): An antibody for analysis of autophagy induction. *Nat Methods* 17, 232-239
- Vahsen BF, Ribas VT, Sundermeyer J, Boecker A, Dambeck V, Lenz C, Shomroni O, Caldi Gomes L, Tatenhorst L, Barski E, et al. (2020): Inhibition of the autophagic protein ULK1 attenuates axonal degeneration in vitro and in vivo, enhances translation, and modulates splicing. *Cell Death Differ* 27, 2810-2827

Vidal SM, Salinas NM, Nadal NFM, Alarcón ML, Valiente SFJ, de Imperial JM, Avilés TM, Agudo BM, Villegas PMP (2012): Understanding glaucomatous damage: anatomical and functional data from ocular hypertensive rodent retinas. *Prog Retin Eye Res* 31, 1-27

Vidoni C, Follo C, Savino M, Melone MAB, Isidoro C (2016): The Role of Cathepsin D in the Pathogenesis of Human Neurodegenerative Disorders. *Med Res Rev* 36, 845-870

Vorwerk CK, Zurakowski D, McDermott LM, Mawrin C, Dreyer EB (2004): Effects of axonal injury on ganglion cell survival and glutamate homeostasis. *Brain Res Bull* 62, 485-490

Vorwerk CK, Naskar R, Schuettauf F, Zurakowski D, McDermott LM, Quinto KM, Dreyer EB (2001): Excitotoxicity can be mediated through an interaction within the optic nerve; activation of cell body NMDA receptors is not required. *Vet Ophthalmol* 4, 201-204

Waller A (1851): Experiments on the Section of the Glosso-Pharyngeal and Hypoglossal Nerves of the Frog, and Observations of the Alterations Produced Thereby in the Structure of Their Primitive Fibres. *Edinb Med Surg J* 76, 369-376

Wang J, Struebing FL, Geisert EE (2021): Commonalities of optic nerve injury and glaucoma-induced neurodegeneration: Insights from transcriptome-wide studies. *Exp Eye Res* 207, 108571

Wang JT, Medress ZA, Barres BA (2012): Axon degeneration: molecular mechanisms of a self-destruction pathway. *J Cell Biol* 196, 7-18

Wang Y, Song M, Song F (2018): Neuronal autophagy and axon degeneration. *Cell Mol Life Sci* 75, 2389-2406

Wirth M, Joachim J, Tooze SA (2013): Autophagosome formation--the role of ULK1 and Beclin1-PI3KC3 complexes in setting the stage. *Semin Cancer Biol* 23, 301-309

Wu J, Lipinski MM (2019): Autophagy in Neurotrauma: Good, Bad, or Dysregulated. *Cells* 8, 693

Wyss CT (2016): Ageing, neurodegeneration and brain rejuvenation. *Nature* 539, 180-186

Xie Z, Klionsky DJ (2007): Autophagosome formation: core machinery and adaptations. *Nat Cell Biol* 9, 1102-1109

Xu H, Zhu Y, Chen X, Yang T, Wang X, Song X, Xie X, Hu M, Jiang L, Cheng J, et al. (2021): Mystery of methamphetamine-induced autophagosome accumulation in hippocampal neurons: loss of syntaxin 17 in defects of dynein-dynactin driving and autophagosome-late endosome/lysosome fusion. *Arch Toxicol* 95, 3263-3284

Yang KC, Sathiyaseelan P, Ho C, Gorski SM (2018): Evolution of tools and methods for monitoring autophagic flux in mammalian cells. *Biochem Soc Trans* 46, 97-110

Yang Y, Coleman M, Zhang L, Zheng X, Yue Z (2013): Autophagy in axonal and dendritic degeneration. *Trends Neurosci* 36, 418-428

Yang Z, Klionsky DJ (2010): Mammalian autophagy: core molecular machinery and signaling regulation. *Curr Opin Cell Biol* 22, 124-131



Zhang JN, Koch JC (2017): Collapsin response mediator protein-2 plays a major protective role in acute axonal degeneration. *Neural Regen Res* 12, 692-695

Zhang JN, Michel U, Lenz C, Friedel CC, Köster S, d'Hedouville Z, Tönges L, Urlaub H, Bähr M, Lingor P, et al. (2016): Calpain-mediated cleavage of collapsin response mediator protein-2 drives acute axonal degeneration. *Sci Rep* 6, 37050

Zhang K, Jiang M, Fang Y (2021): The Drama of Wallerian Degeneration: The Cast, Crew, and Script. *Annu Rev Genet* 55, 93-113

Zhao YG, Zhang H (2019): Autophagosome maturation: An epic journey from the ER to lysosomes. *J Cell Biol* 218, 757-770

Zhao YG, Codogno P, Zhang H (2021): Machinery, regulation and pathophysiological implications of autophagosome maturation. *Nat Rev Mol Cell Biol* 22, 733-750

## 7 Acknowledgements

First of all, my sincere gratitude goes out to PD Dr. med. Jan Christoph Koch for providing me the opportunity to conduct research in his laboratory. I am also deeply grateful for his support and guidance over the whole process of my doctoral thesis. Especially, I really appreciate the freedom he gave me during this period, inspiring me to think independently about scientific issues. I believe this was a valuable experience in my career.

Besides, I thank Prof. Dr. Mathias Bähr for the chance that he gave me to work in his department.

I also want to thank Dr. Alexander Böcker for his practical and constructive suggestions and helpful assistance on my experimental project.

Furthermore, I express special thanks to my second supervisor, PD Dr. med. Christian van Oterendorp, who always provided insightful comments that improved my experiments.

I also thank Ms. Elisabeth Barski for her great technical support and excellent advice at the lab. Her patience and willingness to assist are always admirable. Her passion for her work also motivates me.

In addition, I would like to thank Dr. Jiong Zhang for kind help during the initial stages of my experiments, which allowed me to quickly adapt to lab work. I also appreciated his patience and expertise in answering my questions and guiding me through the surgical procedure.

Many thanks also go to my wonderful colleagues for countless good communication, friendly cooperation, and positive encouragement in difficult situations. Thanks for the great time spent with them.

Last but not least, I am also grateful to the China Scholarship Council for supporting me in completing my study in Germany.

## **8 Curriculum vitae**

My name is Xiaoyue Luo, a female born on January 18th, 1995, in Shaoyang, Hunan Province, China. From September 2011 to June 2016, I finished studying at Hunan Normal University and got a bachelor's degree in clinical medicine. After that, I was recruited to Sichuan University to continue my postgraduate study. During this period (from September 2016 to June 2019), I obtained a master's degree in neurology and completed resident training as a neurologist. Subsequently, in January 2020, with financial support from China, I started a medical doctoral project in the neurology department at the University of Göttingen under the supervision of PD Dr. med. Jan Christoph Koch.